

Impact of IL4-R signaling on microglia/MDM during breast carcinoma CNS colonization



Dissertation
for the attainment of the doctoral degree
in Biomedical Science
(Dr. rer. physiol.)

of the
Faculty of Medicine
of the University of Regensburg

submitted by
Laura Trigueros López

from
Málaga

In the year
2022

Impact of IL4-R signaling on microglia/MDM during breast carcinoma CNS colonization



Dissertation
for the attainment of the doctoral degree
in Biomedical Science
(Dr. rer. physiol.)

of the
Faculty of Medicine
of the University of Regensburg

submitted by
Laura Trigueros López

from
Málaga

In the year
2022

Dean: Prof. Dr. Dirk Hellwig

Supervisor: Prof. Dr. med. Tobias Pukrop

Day of the oral examination: 19.09.2022

Table of contents

Table of contents	3
Zusammenfassung	7
1. Introduction	8
1.1. Brain metastasis: relevance and limitations.....	8
1.2. Metastatic brain colonization.....	9
1.2.1. Growth patterns of brain metastasis.....	11
1.2.2. Immune infiltration at the MMPI of brain metastasis.....	13
1.2.2.1. Microglia/BMDM within the brain-MME.....	14
1.3. Metabolic reprogramming of cancer cells: ROS fitness.....	16
1.3.1. Ferroptosis: a novel therapy for BM.....	17
1.4. Metastasis-promoting role of microglia/BMDM in the brain-MME.....	18
1.4.1. IL4 as an immune activator of the brain-MME.....	19
1.5. Aim of the study.....	22
2. Materials and Methods	24
2.1. Materials.....	24
2.1.1. Biological materials.....	24
2.1.1.1. Cell lines.....	24
2.1.1.2. Primary cells.....	24
2.1.1.3. Mouse strains.....	24
2.1.1.3.1. Genetically modified mice.....	24
2.1.2. Cell culture media and additives.....	26
2.1.3. Chemicals, enzymes and ready-to-use reagents.....	26
2.1.4. Buffers and solutions.....	27
2.1.5. Antibodies and fluorescence dyes.....	29
2.1.6. Oligonucleotides.....	30
2.1.7. Commercial kits.....	31
2.1.8. Consumables.....	31
2.1.9. Equipment.....	33
2.1.10. Software products and databases.....	34
2.2. Methods.....	36
2.2.1. Cell culture methods.....	36
2.2.1.1. Maintenance of tumor cells.....	36

2.2.1.1.1. Assessment of proliferation.....	36
2.2.1.2. Primary cell isolation and culture.....	36
2.2.1.2.1. Primary cultures of microglia.....	36
2.2.1.2.2. Primary cultures of monocytes-derived macrophages (MDM).....	38
2.2.2. Functional in vitro assays.....	39
2.2.2.1. Hanging Drop assay.....	39
2.2.2.2. Chemotaxis assay.....	40
2.2.3. <i>In vivo</i> experiments.....	41
2.2.3.1. Stereotactical intracortical injection.....	41
2.2.3.2. Immune checkpoint inhibitor therapy.....	42
2.2.3.3. Animal maintenance and monitoring.....	42
2.2.3.4. Perfusion and organ isolation.....	43
2.2.4. Protein biochemistry.....	44
2.2.4.1. Protein isolation.....	44
2.2.4.2. Protein quantification by Lowry assay.....	44
2.2.5. Western Blot.....	44
2.2.5.1. SDS-PAGE.....	44
2.2.5.2. Western Blot development.....	45
2.2.6. Gene expression analysis.....	46
2.2.6.1. RNA methods.....	46
2.2.6.1.1. Isolation of total RNA from murine tissue samples.....	46
2.2.6.1.2. Isolation of mRNA from eukaryotic cells.....	47
2.2.6.1.3. Reverse transcription.....	47
2.2.6.1.4. Quantitative real-time PCR (qRT-PCR).....	48
2.2.6.1.4.1. Establishment of primers for qRT-PCR reactions.....	49
2.2.6.2. DNA methods.....	49
2.2.6.2.1. Isolation of total DNA from eucaryotic cells.....	49
2.2.6.2.2. Isolation of total DNA from tissue samples.....	50
2.2.6.2.3. Conventional PCR.....	51
2.2.6.2.3.1. Establishment of primers for conventional PCR.....	52
2.2.7. Staining.....	52
2.2.7.1. Immunofluorescence staining.....	52
2.2.7.1.1. Staining of MG/ MDM.....	53
2.2.7.1.2. Staining of tumor cells.....	53
2.2.7.1.3. Staining of tumor cell spheroids.....	54

2.2.7.2. Staining of brain tissues	54
2.2.7.2.1. Hematoxylin and eosin staining.....	55
2.2.7.2.2. Immunohistochemical stainings	56
2.2.8. Microscopy.....	57
2.2.8.1. Bright field microscopy.....	57
2.2.8.2. Confocal microscopy	57
2.2.9. Statistical analysis.....	57
3. Results.....	59
3.1. Murine breast cancer cell lines.....	59
3.1.1. Characterization of murine breast cancer cell lines	59
3.2. Brain metastasis mouse models	62
3.2.1. TUBO breast cancer brain metastasis mouse model.....	62
3.2.2. Comparison of breast cancer brain metastasis mouse models.....	64
3.2.2.1. Overall survival and colonization index.....	64
3.2.2.2. Tumor load analyses by qRT-PCR	65
3.2.2.3. Macro-metastasis / organ-parenchyma interface (MMPI).....	66
3.2.2.4. The immune microenvironment in BM.....	68
3.2.2.4.1. Characterization of MG/MDM in the metastatic brain.....	68
3.2.2.4.2. Characterization of astrocytes in the metastatic brain	70
3.2.2.4.3. Characterization of T cells in the metastatic brain	71
3.2.2.5. Cytokine expression profile.....	73
3.2.3. Macrophage migration: “cold” versus “hot” tumor models.....	75
3.3. IL4/IL4R signaling.....	77
3.3.1. Characterization of IL4 signaling on murine BM model cell lines.....	77
3.3.2. Characterization of IL4 signaling on MDM/MG.....	80
3.3.3. IL4 signaling knockout in BM mouse models	85
3.3.3.1. Effects of IL4-signaling knockout in overall survival, CI tumor load and MMPI.....	85
3.3.3.2. The microenvironment in BM of IL4R knockout mice	90
3.3.3.2.1. Characterization of MG/MDM in the metastatic brain of IL4R knockout mice.....	90
3.3.3.2.2. Characterization of astrocytes in the metastatic brain of IL4R KO mice	93
3.3.3.2.3. Characterization of T cells in the metastatic brain of IL4R KO mice	95
3.3.3.3. Therapeutic approach to IL4R- signaling.....	97
3.3.3.4. MDM conditional IL4R KO mouse model.....	100
3.4. Explanation for IL4 signaling modulation sensitivity of 410.4 model	101
3.4.1. ROS sensitivity in BCBM models	105

4. Discussion.....	108
4.1. Comparison of MMPI colonization models in the CNS	108
4.1.1. Impact of E/M status of metastatic tumor cells in MMPI patterns	108
4.1.1.1. E/M cellular status impacts immunotherapy.....	110
4.2. Impact of the MMPI pattern on immune infiltration	111
4.3. IL4 as an immune activator in brain metastasis	112
4.3.1. Immunotherapy in IL4R α -KO models	114
4.4. ROS fitness as a driver for IL4 sensitivity	115
4.5. IL4 effect in microglia/MDM	118
4.6. Future research perspectives.....	119
5. Summary and Conclusions.....	120
6. Appendix.....	123
6.1. List of Tables	123
6.2. List of Figures.....	124
6.3. Abbreviations.....	126
7. Bibliography	129
8. Acknowledgements.....	137
9. Curriculum Vitae	¡Error! Marcador no definido.

Zusammenfassung

Hirnmetastasen sind mit einer sehr schlechten Prognose verbunden und treten häufig bei Brustkrebs auf. Trotz bedeutender wissenschaftlicher und klinischer Fortschritte nimmt die Häufigkeit von Hirnmetastasen weiter zu. Die metastatische Besiedlung des Gehirns gilt als der entscheidende Schritt in der Metastasierungskaskade, da sie das Fortschreiten der gestreuten Krebszellen zur Bildung klinisch nachweisbarer Makrometastasen ermöglicht. In jüngster Zeit wurden infiltrative Kolonisationswachstumsmuster an der Schnittstelle zwischen Makro-metastasen und Organ-parenchym (MMPI) mit ungünstigen Patientenergebnissen in Verbindung gebracht und gelten aufgrund ihrer prognostischen Auswirkungen als klinisch relevant.

In dieser Studie stellten wir die Hypothese auf, dass der IL4R-Signalweg in aus dem Knochenmark stammenden Makrophagen (BMM)/Mikroglia entscheidend für den metastasenfördernden Makrophagen-Phänotyp während der Besiedlung des Gehirns durch Brustkrebszellen ist. Um die Auswirkungen der IL4R-Signalisierung in MDM/Mikroglia während der Besiedlung des Gehirns zu bestimmen, wurden drei Brustkrebs-Hirnmetastasen-Mausmodelle mit unterschiedlichen MMPI-Mustern verwendet. Die *In-vitro*-Charakterisierung der IL4-Signalaktivierung in MDM/Mikroglia und den Hirnmetastasen-Mausmodellen deutete darauf hin, dass die pro-metastatischen Effekte der IL4/IL4-R-Signalaktivierung weitgehend von der Makrophagenkomponente und nicht von den Tumorentitäten selbst abhängig sind.

Eine umfassende Charakterisierung der metastatischen Mikroumgebung *in vivo* ergab einen klaren Zusammenhang zwischen den MMPI-Mustern und der Immuninfiltration. Darüber hinaus wurden bei der Unterbrechung der IL4/IL4R-Signalübertragung keine Veränderungen im MMPI der Hirnmetastasenmodelle beobachtet. Die Hemmung von IL4-R führte jedoch zu einer drastischen Verlängerung der Gesamtüberlebenszeit, einer signifikanten Verringerung des Kolonisierungspotenzials sowie einer abrupten Veränderung der Verteilung der Immunpopulation in einem Hirnmetastasenmodell mit infiltrativem MMPI-Muster. Die Suszeptibilität für eine Unterbrechung der IL4-Signalübertragung *in vivo* geht mit einer erhöhten Anfälligkeit für eine Glutathionhemmung einher, was auf einen Zusammenhang zwischen dem Erwerb einer infiltrativen MMPI, der Empfindlichkeit für die IL4-Signalübertragung und einer eingeschränkten metabolischen Flexibilität während der BCBM hinweist.

Zusammenfassend belegen diese Daten die entscheidende Rolle der IL4-R-Signalübertragung in MDM/Mikroglia während der metastatischen Besiedlung des Gehirns. Diese ist vor allem für die potenzielle therapeutische Rolle der MMPI-Muster für zukünftige Untersuchungen der grundlegenden biologischen Mechanismen der metastatischen Besiedlung von Relevanz.

1. Introduction

1.1. Brain metastasis: relevance and limitations

Brain metastases (BM) are the most common intracranial tumors in adults, with a frequency varying from 20 to 40% if clinical diagnosis or postmortem studies are considered, respectively (Tabouret et al., 2012; Achrol et al., 2019). BM confer a very poor prognosis, with an estimated overall survival (OS) of 6 months to 2 years in treated patients, and have devastating impact on patient's quality of life (QoL) even before any treatment. Any type of primary tumor can potentially metastasize to the brain, with lung cancer (20-56%), breast cancer (5-20%), and melanoma (7-16%) accounting as the three most common primary tumors associated with BM (Berghoff et al., 2016; Valiente et al., 2018; Achrol.,2019). The incidence of BM is on the rise in cancer patients irrespective of the origin of the primary tumor, possibly boosted by the improvement of imaging techniques uncovering primary disease and the delayed mortality of patients associated with early diagnosis (Tabouret et al., 2012; Moravan et al., 2020). The incidence of BM is strongly influenced by different key factors ranging from clinical to non-clinical aspects. Non-clinical aspects account for the biological sex, ethnicity, age or geographical location of the patient, whereas clinical aspects include the type of primary tumor from which BM arises, the number of developed metastasis, or the stage of the extracranial disease. Among these, the molecular subtype of the primary tumor is known to tremendously impact the occurrence, survival, and treatment of BM (Nguyen et al., 2009; Tabouret et al., 2012; Berghoff et al., 2016; Achrol et al., 2019). Brain metastases derived from breast cancer are a good example of this. Patients characterized with the human epidermal growth factor receptor 2-positive (also known as HER2+) or the triple-negative hormone receptor (TN; estrogen receptor-negative, progesterone receptor-negative, and normal HER2 levels) molecular subtypes account for the most aggressive forms of breast cancer and experience higher risk of developing metastasis in the brain than patients with other molecular subtypes (Martin A. et al., 2017; Rostami et al., 2016).

Despite the plethora of systemic treatment strategies designed in the last decades to palliate the lethal status of BM (Hendricks et al., 2019; Long et al., 2018), the efficacy of targeted- and immune- therapies are still very limited in patients (Valiente et al., 2018). In this regard, the brain comprises unique anatomical features that significantly contribute to therapy resistance. The blood-brain barrier (BBB) or the blood-brain metastasis barriers (BBM) decrease the concentration of drug therapies in the brain compared to other organ metastases, which explains the short survival of treated patients (Arvanitis et al., 2019). Another singular feature of the brain involves its highly immunosuppressive nature, resulting in significantly lower infiltration of T-cells compared to other organs and a consequently decreased response to immune checkpoint (ICP) therapies. Precisely, the acquisition of a unique cellular architecture responsible for the

immune-suppressive environment of the brain and the difficulties for cells and drugs to cross the BBB prevents extrapolation of findings from other cancers to the brain (Quail and Joyce, 2017). Particularly, novel therapeutic interventions against the most aggressive ways of breast cancer brain metastasis (BCBM), which include stereotactic radiosurgery and treatment with trastuzumab, pertuzumab, bevacizumab, lapatinib, or capecitabine agents (Rostami et al., 2016), continue showing a partial response, advocating for new approaches to the disease.

1.2. Metastatic brain colonization

Metastasis is a branched and highly complex phenomenon in which tumor cells disseminate to a distant secondary organ. In general, disseminated metastatic tumor cells can arise from the spread of tumor cells from a primary tumor site through the blood to the brain microvasculature (linear progression model), or from the early dissemination of tumor cells in parallel and independently of the development of the primary tumor (parallel progression model) (Hosseini et al., 2016). Regardless of their origin, the formation of metastasis at a secondary organ constitutes the final stage of a long, multi-phase process in which survival of metastatic tumor cells is highly rare and inefficient in biological terms (Vanharanta and Massague, 2013). At each step of the metastatic cascade, tumor cells can die, spread by migratory mechanism, or remain dormant for periods (weeks, months, or even years) by mechanisms yet incompletely understood (Nguyen et al., 2009). Seeding of the metastatic tumor cells implies its intravasation into circulation, either directly or via the lymphatic system. Likewise, survival, adhesion, and circulatory arrest within the vasculature are required to extravasate into the parenchyma of the brain. Unlike metastatic development in other secondary organs, the first barrier to the spread of tumors in the brain is the BBB, which must be overcome by metastasizing cancer cells prior to the formation of micrometastases ($<2\text{mm}$) (Blazquez et al., 2020B). In event of success, the extravasated tumor cells need to survive in the singular brain microenvironments, which harbor tissue-resident cell types including neurons, astrocytes, and microglia. Thus, metastatic tumor cells fall into a very particular metastatic niche in which they must restart their proliferative programs as a prerequisite to the generation of macroscopic and clinically detectable neoplastic growths (Achrol et al., 2019).

Millions of cancer cells manage to intravasate the vasculature from the primary tumor, although only 0.01% of the disseminated metastatic cancer cells manage to successfully colonize the distant organ and create clinically detectable macro-metastasis ($\geq 2\text{ mm}$). Besides, all previous steps before colonization, including the formation of micrometastases, are most likely completed at the time of the cancer diagnosis (Vanharanta and Massague, 2013), which makes the metastatic colonization the rate-limiting step of the metastatic

cascade from a biological and clinical point of view (Fidler, 1970) (Figure 1). Importantly, micrometastases are usually unclearly delimited from the surrounding tissue during the early phases of tumor cell dissemination (stages I-III). Only when they develop into macro-metastases are they recognizable by their growth pattern.

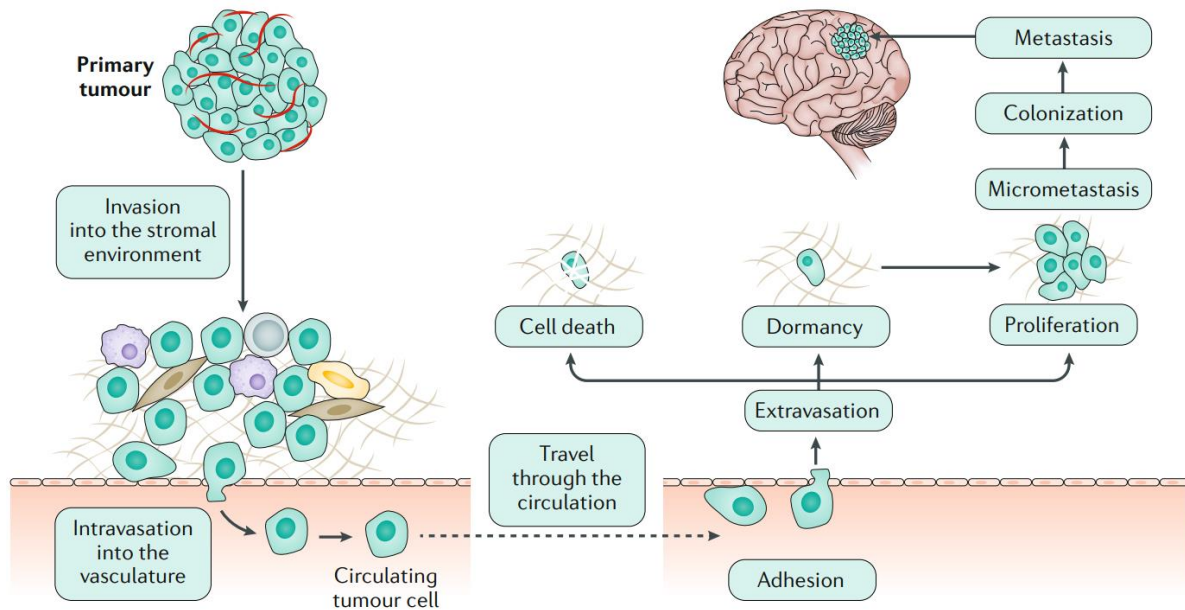


Figure 1. Metastatic brain colonization. Dissemination of metastatic cells to the brain implies multiple steps including invasion of the stromal environment from the primary tumor, intravasation into the vasculature, adhesion, and circulatory arrest within the vasculature. By extravasation into the parenchyma of the brain, cells need to survive in the singular brain microenvironments. A restart of their proliferative programs leads to colonization of the metastatic site, forming first a micro-metastasis which eventually develops into a macro-metastasis. Seeding of disseminated cancer cells into organ targets can occur before primary tumor diagnosis in most of BM-patients. Adapted from (Achrol et al., 2019).

Over the last few decades, research has emphasized the existence of multiple phenotypes within a single tumor (Venkatesan et al., 2022), postulating that the intratumor heterogeneity of cancer is closely related to genomic instability in the tumor cells. Genomic instability is understood as a spectrum of different genetic aberrations acquired early in tumorigenesis that provides properties with survival advantages to certain tumor cells (Heppner, 1984), leading to the creation of resistant tumor subclones able to adapt to new environments (Negrini et al., 2010). Importantly, genome instability favoring the tumor's fitness correlates negatively with patient survival and poor clinical outcome in different types of cancer

(Venkatesan et al., 2022). In this context, the emergence of new technologies such as next-generation sequencing has redefined the notion of cancer evolution and identified different modes of cancer development. Historically, it was believed that cancer followed a multi-step process of oncogene activation leading to the selection of a single, fittest tumor cell clone as the trigger for tumor progression (big-bang theory) (Nowell, 1976). According to recent research, cancer could have a clonal origin characterized by the occurrence of branched events, in which the introduction of genome modifications evolve during cancer progression into a subset of the progeny. Thus, recent reports on different cancer types, including breast cancer (Yates et al., 2015), suggest that branched evolution is common in cancer, as subclonal/branched driver events are usually present within distinct subclones of a tumor (Venkatesan et al., 2022). Since intratumor heterogeneity and cancer evolution contribute to resistance to therapy, there is a high demand for research on the tolerance and propagation of genome instability in cancer subclones as a strategy against cancer progression and metastasis.

1.2.1. Growth patterns of brain metastasis

Our understanding of how disseminated tumor cells become activated and enter in exponential growth phase, overcoming all-natural barriers preventing colonization, is very limited. Furthermore, not all patients undergo an identical colonization course, manifesting important biological differences that impact the clinical detection of the macro-metastasis. Importantly, there are several prognostic factors that allow for improving diagnosis and eventual treatment of patients. One important prognosis factor for BM patients is the presence of infiltrative metastatic growth at the so-called macro-metastasis organ parenchyma/ interface (MMPI) (Siam et al., 2015). The MMPI is defined as the area where cells of the macro-metastasis (≥ 2 mm) and its metastatic microenvironment are in direct contact with the (healthy) adjacent organ parenchyma (Blazquez et al., 2020B). In the past, metastatic growth was understood as an event of stable growth devoid of infiltration, overlooking the clinical relevance of the infiltrative MMPI and its association with unfavorable patient outcomes. Recently, MMPI patterns have been shown to correlate with the overall survival of patients in several types of metastases, including BM (Siam et al., 2015). The MMPI develops over time and evolves in the transition from micro- to macro-metastasis (Siam et al., 2015). Remarkably, the major prognostic feature of the MMPI patterns refers to the grade of infiltration of the metastasis, according to which three main categories have been described: displacing (non-infiltrative), epithelial infiltrative, and diffuse infiltrative MMPIs (Blazquez et al., 2020B) (Figure 2). Remarkably, the existence of different patterns of colonization at the MMPI has been related to the existence of different pathomechanisms driving metastatic progression, leading to speculation about the existence of different potential therapeutic targets.

Displacing MMPIs present a non-infiltrative growth pattern, in which tumor cells comprising the macro-metastasis expand by pushing into the adjacent parenchyma. This type of metastasis shows sharply defined margins and, eventually, a reactive pseudo-capsule demarcating healthy tissue from the tumor core. A reactive pseudo-capsule mostly consisting of glial cells has been observed in the majority of brain metastasis, with collagen aggregates in rare cases that result in a multilayer pseudo-capsule (Siam et al., 2015; Berghoff et al., 2013). Strikingly, displacing MMPIs have been observed in 40% of BM patients and are associated with a good prognosis and lower recurrence (Blazquez et al., 2020B).

On the contrary, infiltrative MMPIs are characterized by containing tumor cells that overcome the physical barrier of the surrounding tissue and/or the pseudo-capsule. Infiltrative metastatic cells reach distant areas outside the metastatic core and are accompanied by severe tissue damage. Remarkably, infiltrative metastatic growth at the MMPI has been reported in approximately 60% of all brain metastasis to date and is associated with a worse prognosis and unfavorable patient outcome (Siam et al., 2015; Blazquez et al., 2020B). Notably, the infiltrative MMPIs can be subdivided as epithelial or diffuse depending on the epithelial/mesenchymal (E/M) features of the infiltrating tumor cells, respectively. Epithelial infiltration occurs in epithelial tumor cells that require cell-cell adhesion to infiltrate the adjacent parenchyma. They infiltrate collectively as a group (strand, cluster, glandular or angiotropic infiltration) and commonly show a short infiltration depth (<1mm). This type of epithelial infiltrative MMPI is often found in BCBM (Siam et al., 2015). A diffuse infiltrative MMPI pattern, however, refers to tumor cells with mesenchymal characteristics, including the acquisition of mesenchymal-like morphology, which deeply infiltrates the adjacent tissue (>2mm) with no need for cell-cell adhesion (Siam et al., 2015; Blazquez et al., 2020B). Due to its deep infiltrative capacity, this MMPI pattern can define metastasis with or without a visible metastatic core, finding the diffuse infiltrative MMPI without visible macroscopic metastasis the worst-case scenario. Remarkably, diffuse infiltration of mesenchymal cancer cells has been associated with resistance to therapy in different types of cancer and related to dependency on molecules with potent anti-oxidant capacity (Viswanathan et al., 2017).

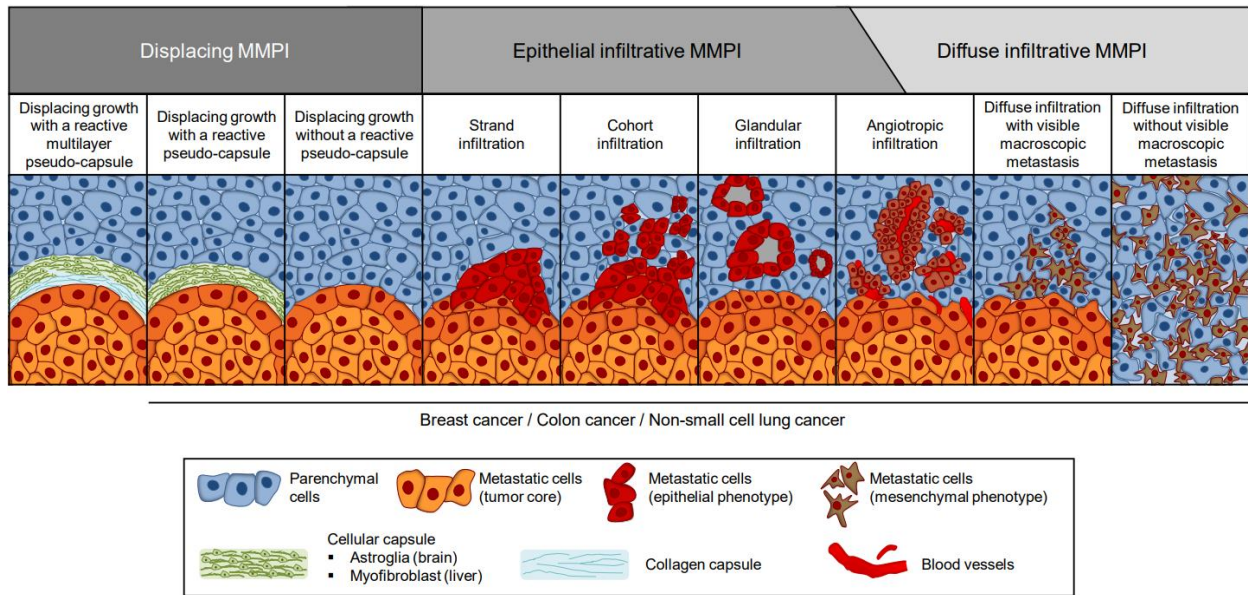


Figure 2. Macro-metastasis/organ parenchyma interface (MMPI) patterns. MMPI patterns are classified into three main categories according to the grade of infiltration of the metastasis: displacing (non-infiltrative), epithelial infiltrative, and diffuse infiltrative MMPIs. These MMPIs have been described for breast, colon, and non-small cell lung cancer. Adapted from (Blazquez et al., 2020B).

1.2.2. Immune infiltration at the MMPI of brain metastasis

The metastatic microenvironment (MME) is widely accepted as a prominent regulator of tumor progression and metastasis. Beyond disseminated tumor cells, the brain-MME is comprised of surrounding non-neoplastic cells, including tissue-resident and recruited immune entities, and structural components of the extracellular matrix (ECM) of the host tissue (Friedl and Alexander., 2011; Neta and Coussens., 2011). Recent studies have demonstrated the role of the immune compartment as a sculptor of the immunosuppressive niche of the brain-MME, identifying tissue-resident microglia, infiltrating bone marrow-derived macrophages (BMDMs), and T-cells among the major immune cell determinants in the metastatic landscape (Klemm et al., 2020). Importantly, accumulation of active microglia and recruited macrophages with amoebic morphology have been reported at the tumor-brain interface of central nervous system (CNS) metastases in several cancer types, including breast cancer, in mice models (HP et al., 2006; Berghoff et al., 2013) and human brain metastases (Amit et al., 2013). In this regard, the MMPI has been suggested to influence the immune infiltration landscape of the brain-MME (Blazquez et al., 2020B; Sparrer et al., unpublished). Nevertheless, the capacity of the MMPI in determining the infiltration of immune cells requires further investigation.

1.2.2.1. Microglia/BMDM within the brain-MME

Microglia and BMDMs are two ontogenetically different populations within the brain-MME (Bowman et al., 2016) that, together, account for up to 30% of the tumor mass (Klemm et al., 2019). Brain microglia, derived from embryonic yolk sac progenitor cells, are the resident macrophages of the CNS and are considered part of the first line of defense of the CNS. Microglia self-maintain their population through adulthood by local proliferation and prolonged cellular longevity, independently of peripheral mononuclear hematopoiesis (Perdiguerro et al., 2015). Unlike microglia, BMDMs derive from circulating monocytes and are recruited to the brain parenchyma only under pathological conditions, where the integrity of the BBB can be compromised (Shi and Pamer, 2011) (Figure 3).

Strikingly, the main target organs of metastasis have been found to harbour tissue-specific macrophage populations (Pukrop et al., 2010, Cotechini et al., 2021). Under physiological conditions, microglia are involved in immune surveillance, maintenance of the CNS homeostasis and prevention of peripheral immune cell recruitment, usually associated with inflammation and tissue damage. However, pathological events such as sensing of pathogen-associated molecular patterns (PAMPs), damage-associated molecular patterns (DAMPs), or metastatic progression results in chronic microglial activation and acute tissue damage responses including neuroinflammation, increased permeability of the BBB, and recruitment of peripheral immune cells (Doron et al., 2019; Fitzgerald., 2008). Similarly, monocyte-related macrophages have been largely related to metastatic progression and therapy resistance (Cotechini et al., 2021) and previously implicated in immune suppression and tumor-promoting wound healing processes within the brain-MME (Bowman et al., 2016).

The key feature enabling the broad functional profile of the macrophage population within the brain-MME resides in their high plasticity. Microglia and BMDMs can integrate environmental stimuli, such as cytokines and chemokines secreted into their immediate milieu (Bowman et al., 2016), undergoing a multifaceted response that incorporates canonical M1 and alternative M2 polarization (Klemm et al., 2020). Interestingly, this spectrum of M1-M2 phenotypes reflects a continuum of macrophage functional diversity, in which simultaneous pro- and anti-inflammatory states can be found in a context-dependent manner, rather than a black and white condition (Klemm et al., 2020). The M1-like macrophage phenotype mediates resistance to pathogens by inducing inflammation (pro-inflammatory function), while the M2-like macrophages are involved in tissue remodeling, immune regulation, and tumor progression (anti-inflammatory function). The progressive polarization of macrophages into pro-metastatic, immunosuppressive phenotypes (M2-like) occurs in the presence of an oncogenic event, where inflammation upgrades from acute to chronic (Doron et al., 2019). M2-like macrophages can be further divided into subsets based on their distinct gene expression profiles. All subsets of M2-like tissue-resident

microglia and recruited BMDMs comprise the tumor-associated macrophage (TAM) population within the BM landscape (Nielsen and Schmid., 2017), which profoundly determine immunosuppressive effects on T cell functioning, immune checkpoint blockade (ICB) therapy resistance (Ruffell et al., 2015) and neutrophil recruitment in BM (Klemm et al., 2020).

Interestingly, M2-polarized macrophages mostly accumulate at the MMPI of the macro-metastasis, creating contact with the carcinoma cells directly after successful extravasation, leading to marked increased invasion capacity of the cancer cells (Blazquez et al., 2018). It is therefore reasonable to speculate that the MMPI plays a role in the immunosuppression effect exerted by TAMs during the metastatic colonization of the brain.

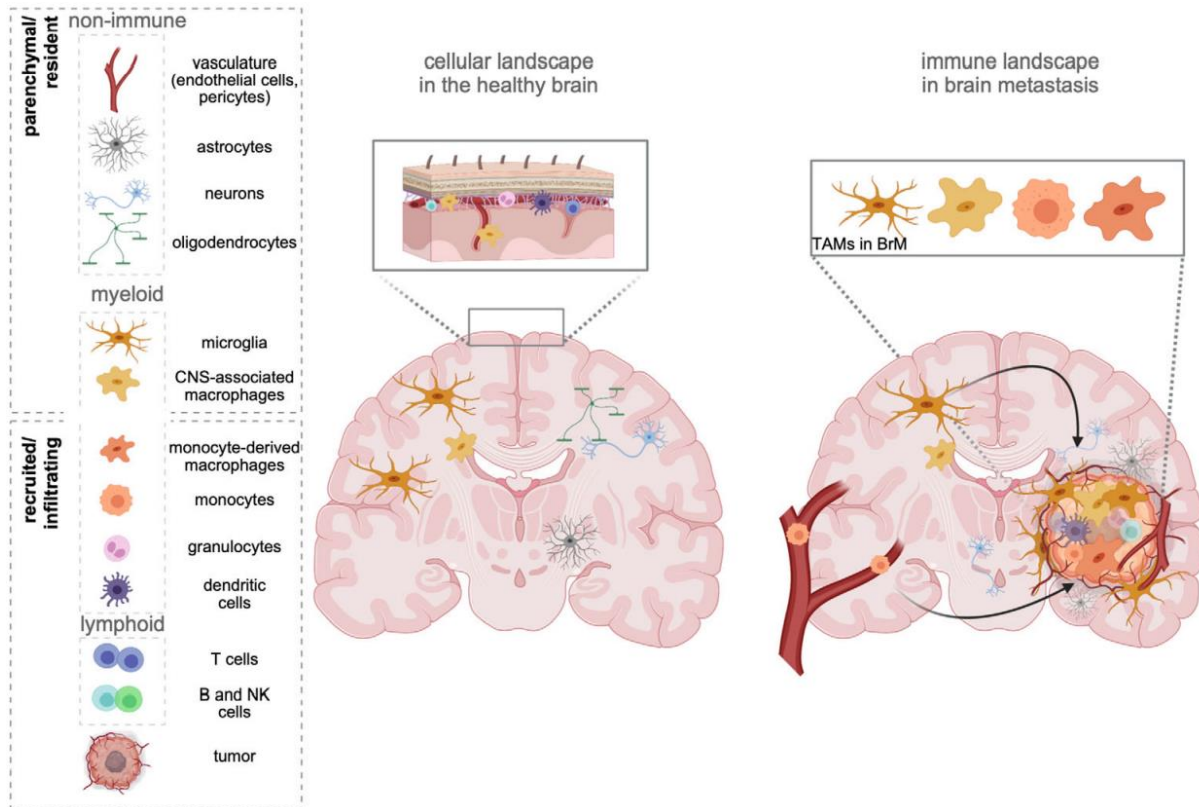


Figure 3. The cellular environment in the healthy brain and BM. The cellular landscape in the healthy brain (left) is comprised of different resident cell types. Among them, microglia represent the only immune cell, while the rest of the immune system, including CNS-associated macrophages, remains at the border regions of the brain (e.g., meninges, ventricles, perivascular areas). On the contrary, the immune landscape in brain metastasis (right) consists of myeloid and lymphoid immune cells recruited/infiltrating from the periphery. Tumor-associated macrophages (TAMs) population comprises both tissue-resident microglia and recruited BMDMs. Adapted from (Schulz and Sevenich., 2021).

1.3. Metabolic reprogramming of cancer cells: ROS fitness

Reprogramming of cancer cell metabolism is caused by oncogenic mutations that induce aberrant activation of signaling pathways (Hanahan et al., 2011). Alteration of cancer cell metabolism is a common albeit largely unknown event with a great impact on BM development. It occurs throughout the metastatic cascade and is widely accepted as a hallmark of BCBM (Liu and Zhang, 2022). One example resides in the high intrinsic and extrinsic ROS levels that cancer cells metastasizing to the brain have to deal with in order to survive the hostile MME (Zille et al., 2019; Zhang et al., 2021). Intrinsic oxidative stress derives from cancer cell proliferation itself and reported re-activation of oxidative phosphorylation (Fischer et al., 2019), while extrinsic oxidative stress involves the immune response of resident brain parenchyma immune cells including astrocytes and microglia. In this context, the metabolic signature dictating detoxification mechanisms during brain colonization determines the survival of the tumor cells, which have been reported to differ greatly among breast cancer molecular subtypes (Blazquez et al., 2020). The TN and HER2+ breast cancer molecular subtypes exhibit greater reliance on glutathione (GSH) biosynthesis than other molecular subtypes of breast cancer to prevent ROS-mediated death in the metastatic niche. Strikingly, the relationship between ROS fitness and GSH metabolism varies not only among molecular subtypes but also across tumor entities of the same molecular subgroup (Blazquez et al., 2020). Boosting the levels of GSH in breast cancer cells has been related to detoxifying related genes and maintenance of intracellular ROS levels in certain TN breast cancer cell lines, while others have been shown to entail reduced GSH level, decreased antioxidant capacity and increased sensitivity to ROS-mediated death (Blazquez et al., 2020).

In addition to the metabolic modifications associated with ROS fitness, lipid metabolic adjustment has been reported to be crucial for metastatic growth in the brain, especially for HER2-enriched BCBM (Cordero et al., 2019; Brown et al., 2020; Liu and Zhang 2022). Likewise, metastatic tumor cells have been shown to exhibit higher metabolic iron demands during the late stages of the metastatic cascade, given the strict requirements necessary for the rapid division of tumor cells associated with the tumorigenic niche. Besides, and unlike other organs, the brain possesses the unique ability to use alternative fuels including acetate, glutamine, and branched-chain aminoacids when blood glucose levels are low. This brain-specific metabolic flexibility to exploit energy sources other than glucose is enhanced by BBB-mediated limited access to nutrients and hijacked by metastatic cells within the brain-MME (Schild et al., 2018). Thus, metastatic cancer cells can rely on the oxidation of glutamine and fatty acids as well as gluconeogenesis to satisfy their energetic requirements and prevent cell death (Chen et al., 2015).

1.3.1. Ferroptosis: a novel therapy for BM

A terminal consequence of oxidative stress in metastatic tumor cells is ferroptosis (Dixon et al., 2012; Wu et al., 2019), a recently described type of cell death that occurs with iron dependence (Li et al., 2020). Reported in different types of cancer (Sun et al., 2020), ferroptosis is characterized by the accumulation of lipid reactive oxygen species (lipid-ROS) and is functionally and morphologically different from apoptosis or other types of previously described mode of cell death (Dixon et al., 2012). Biochemically, ferroptotic cells experience a depletion of intracellular GSH and an acute decrease of the enzyme glutathione peroxidase 4 (GPX4), the key regulator of ferroptosis. Activation of GPX4 inhibits the formation of cytotoxic lipid peroxides (L-OOH) by converting GSH into oxidized glutathione (GSSG), forming the corresponding toxicity-free alcohols (L-OH), harmless to the cell (Li et al., 2020). Inhibition of GPX4, however, leads to the increase of lipid peroxides susceptible to be oxidized by Fe²⁺ in a Fenton-like manner, which results in the generation of a large amount of intracellular ROS, lipid peroxidation and promotion of ferroptosis. Alterations in iron, lipid and ROS metabolism that allow tumor cells to satisfy metabolic demands and enable growth during metastatic colonization have been described as modulators of ferroptosis, making them vulnerable to ferroptosis-mediated cell death (Hassannia et al., 2019).

The plasticity of the cell state concerning the E/M status of the tumor cells has been closely associated with cellular lipid metabolism and cancer therapy resistance (Byers et al., 2013; Bu et al., 2016; Vriens et al., 2019; Germain et al., 2020). The acquisition of mesenchymal properties of epithelial cancer cells has been related to high susceptibility to lipid peroxidation and reliance on pathways involving GPX4 activity to prevent the iron-mediated reaction of toxic lipid peroxides (Hangauer et al., 2017; Viswanathan et al., 2017). In this regard, mesenchymal-like cancer cells are characterized by high enzymatic activity promoting the synthesis of polyunsaturated lipids, which are the substrate for lipid peroxidation (lipid-ROS). Thus, cell lines in a mesenchymal state depend of GPX4 activity to survive. On the other hand, epithelial-like cancer cells show a decreased GPX4 activity (Viswanathan et al., 2017), suggesting a reduced dependence on the GPX4 enzyme and decreased vulnerability to ferroptotic cell death, which negatively correlates with expression of the epithelial marker E-cadherin (Trigueros et al., 2020, submitted). In these terms, ferroptosis emerges as a potential metabolic target for mesenchymal-like tumor cells. Several FDA-approved drugs have been identified as ferroptosis inducers, which makes ferroptosis a new promising strategy against therapy resistance in cancer and metastasis development (Hassannia et al., 2019).

1.4. Metastasis-promoting role of microglia/BMDM in the brain-MME

A growing body of evidence supporting the pro-tumoral role of MG and BMDM during brain metastasis has increased over the last few years given their prominent status as players in metastatic colonization. In this regard, the recent emergence of novel identification models capable of accurately distinguishing between microglia and recruited BMDMs has uncovered the distinct contributions of both TAM populations to BM-MME (Quail and Joyce, 2017; You et al., 2019; Klemm et al., 2020). Notably, microglia have been shown to foster the infiltration of metastatic cells into the brain parenchyma in several ways. Microglia serve as cellular guiding structures to the carcinoma cells (Chuang et al., 2018; Rietkötter et al., 2013) and increase metastatic cell proliferation (Fitzgerald et al., 2008). Shifting microglia from anti-inflammatory (M2) into inflammatory phenotype (M1) has been further related to reduced cancer cell invasion *in vitro* (Pukrop et al., 2010). In this context, induction of M2 polarization and concomitant attenuation of M1 response of MG/BMDM is widely accepted to profoundly impact tumor growth and invasion in brain metastasis (Wu and Watabe, 2017; Andreou et al. 2017). Furthermore, TAMs interaction with inflammatory MME milieu not only affects tumor cells or immune compartment signaling pathways activation but also shapes the ECM itself in a disease-specific manner (Schild et al., 2018; Klemm et al., 2020), as is the case of ECM shaping by macrophages at the primary sites.

However, the signaling pathways involved in the polarization of TAMs into a metastatic-assisting phenotype remain poorly understood. The few studies on the subject point to the contribution of the Wnt-signaling pathway, which is related to both BMDM-induced invasiveness of carcinoma cells (Pukrop et al., 2006) and microglial assisted-invasion of metastatic cells *in vitro* in an EMT-independent manner (Pukrop et al., 2010). In BCBM, however, the phosphoinositide 3-kinase (PI3K) signaling pathway was found to be activated in brain metastasis-promoting microglia/BMDM as well as in the majority of BCBM tissues, leading to significantly reduced pro-metastatic activity of microglia/BMDM when inhibited. (Blazquez et al., 2018). PI3K is a well-known downstream effector of the colony-stimulating factor 1 receptor (CSF1R) signaling pathway, a classic driver for metastasis-associated microglia/BMDM immune suppression phenotype (Condeelis and Pollard., 2006; De et al., 2014; Erblich et al., 2011; Lin et al., 2001). But most importantly, PI3K γ controls the TAM switch between immune suppression (M2-like phenotype) and immune stimulation (M1-like phenotype) in breast cancer metastasis (Kaneda et al., 2016). Strongly associated with PI3K signaling, the interleukin 4 (IL4) has been described as one of the major downstream effectors of the immune suppression (Kaneda et al., 2016), showing high impact over the TAM population during tumor progression and metastasis (Blazquez et al., 2018).

1.4.1. IL4 as an immune activator of the brain-MME

The IL4 is a pleiotropic Th2-like cytokine produced by hematopoietic cells, including Th2-polarized T cells, granulocytes, and monocytes (Howard et al., 1982; Nelms et al., 1999; Sachin P. et al., 2012), and epithelial cancer cells (Surana R., 2014; Todaro et al., 2008; Venmar and Fingleton, 2014). IL4 covers a wide range of functions from immune regulation (Nelms et al., 1999; McCormick and Heller., 2015) to pathology development in allergy, atopic diseases, or asthma (Mueller et al., 2002). Yet, it should not be confused with a mere anti-inflammatory cytokine. IL4 has been shown to trigger potent type 2 inflammatory processes related to tumor progression and metastasis and is largely identified as a major activator of the alternative M2-metastatic macrophage phenotype in microglia and BMDMs during chronic inflammation (Gordon and Martinez., 2010; Orihuela et al., 2016). Besides targeting immune response, IL4 is known to induce pro-invasive phenotypes in epithelial cancer cells (Hallet et al., 2012; Li et al: 2008; Venmar et al., 2014), which makes it an interesting therapeutic target in terms of re-education of the immunosuppressive MME (Ngiow and Young, 2020).

IL4 signals through a heterodimeric complex, the IL4 receptor (IL4R), in combination with a multitude of cell signaling mediators, transcription factors, and regulatory elements. Physiological signaling of IL4 depends on high-affinity binding ($K_D = 20\text{-}300$ pM) to the IL4R α subunit, which causes a conformational change followed by the association of a secondary low-affinity chain, either the common gamma (γ C) or the IL13-R α 1 chain. The different association of the subunits with the IL4-R α chain results in two different types of receptors: type I IL4R (with the γ C chain), primarily expressed on lymphocytes and myeloid cells, and type II IL4R (with the IL13-R α 1 chain), widely expressed in myeloid cells and most non-hematopoietic cells, including cancer cells (Venmar et al., 2014-; Leland et al., 2000; Todaro et al., 2008) (Figure 4). Recognition of the IL4/IL4R α complex by the γ C chain (type I receptor) induces its heterodimerization and follows auto- and cross-phosphorylation by Jak kinases (Jak1 and Jak3). This results in phosphorylation of the cellular tyrosine (Y) residues within the IL-4R α cytoplasmic domain, which serve as docking sites for the Jak/signal transducer and activator of transcription factor 6 (Stat6) or/and the insulin receptor substrate protein (IRS) (Nelms et al., 1999; McCormick and Heller., 2015). The activation of these intracellular signaling molecules results in the triggering of two main downstream pathways: the IRS-2/PI3K/Akt pathway and the Stat6 pathway, which further promotes phospho-Stat6 homodimerization, nuclear translocation, and gene transcription (Nelms et al., 1999; Venmar et al., 2014; McCormick and Heller., 2015). Similarly, activation of the type II IL4R leads to Stat6 and the tyrosine phosphorylation of IRS, which has been associated with further activation of mTOR, AKT, and MAPK/ERK signaling pathways in different cancer cell types (McCormick and Heller, 2015).

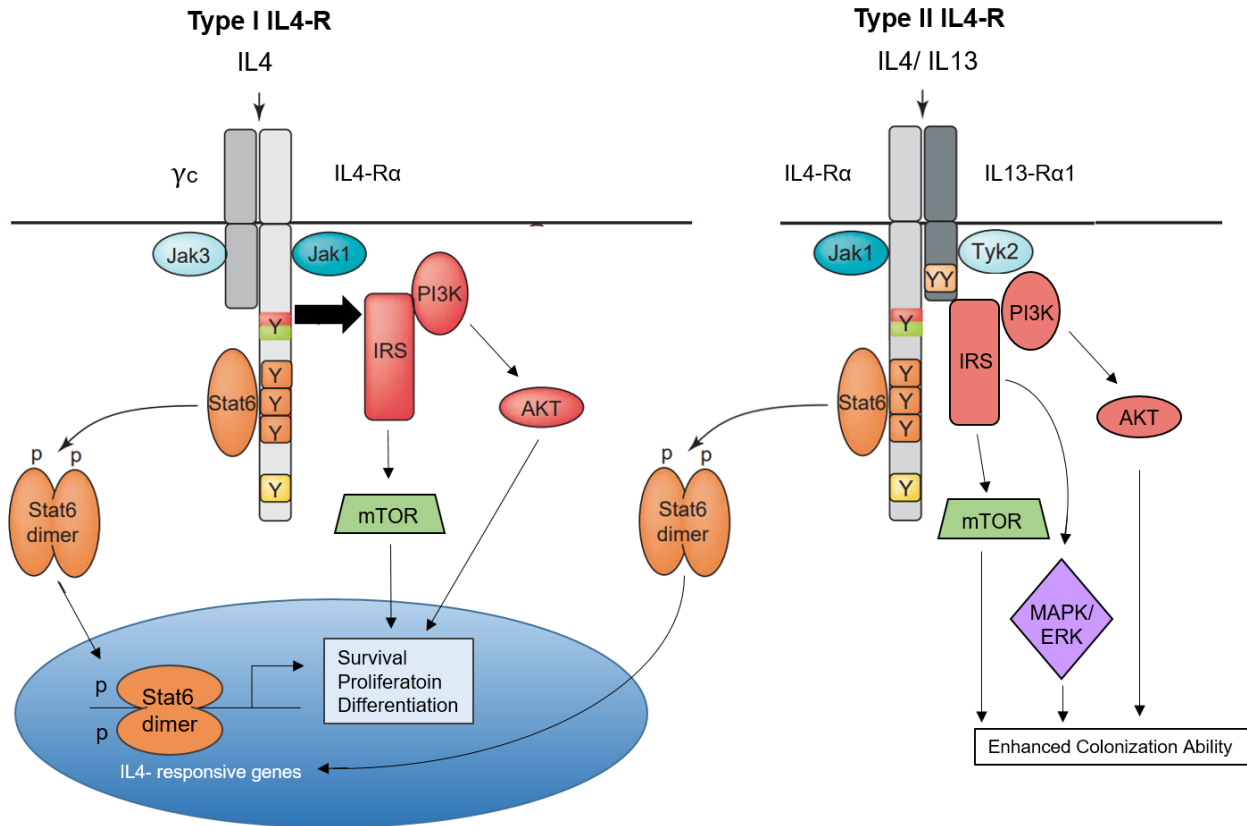


Figure 4. Signaling pathways activated via interleukin 4-receptors (IL4R). Binding of IL4 to the type I IL4R results in activation of the IRS/PI3K/AKT, the IRS/mTOR, and the JAK/STAT6 pathways in hematopoietic cells, which leads to transcription of IL4 responsive genes and the promotion of pro-growth phenotypes. In turn, IL4 promotes pro-metastatic phenotypes in non-hematopoietic cells including epithelial cancer cells upon binding to the type II IL4R. The enhanced colonization ability of the cancer cells is mediated by several signaling pathways including the IRS/PI3K/AKT, IRS/MAPK/ERK, IRS/mTOR, and JAK/STAT6. Adapted from (Chatila., 2004).

Importantly, activation of the type II IL4R has been shown to enhance the colonization ability of breast cancer cells *in vitro*. Attenuating IL4R α expression in metastatic breast cancer cells reduced tumor survival and metastatic potential *in vivo* (Venmar et al., 2014). Consistently, recent studies have shown that depletion of anti-inflammatory M2-like polarized microglia/BMDM population in a murine IL4-induced neuroinflammatory model significantly reduces breast cancer brain metastatic tumor burden *in vivo* (Andreou et al., 2017). The published evidence suggest that IL4 signaling influence cytotoxicity of tumor-infiltrating CD8 T cells, prevent CD4 effector T cell's immune function, and strongly induce the immunosuppressive activity of TAMs (Ito et al., 2017; Villacres et al., 1999; DeNardo et al., 2009).

Although the pro-tumor role of IL4 signaling in tumor progression is understood, its role during metastatic colonization remains largely unknown. IL4 signaling activation in the immunosuppressive TAM population within the brain-MME may lead to sustained breast cancer metastatic outgrowth during late colonization of the brain. Yet, whether IL4R-signaling is involved in the infiltration of the carcinoma cells in the brain parenchyma or if it is part of the intercellular communication between microglia/BMDM and the carcinoma cells at the metastatic site are still open questions. Importantly, combined scientific effort has resulted in several FDA-approved therapies focused on the disruption of IL4, IL4R, and the IL4/IL4R signaling axis (Chiricozzi et al., 2020; Bankaitis and Fligeton, 2015). For that reason, the inhibition of the IL4/IL4R signaling axis constitutes an attractive therapeutic target to reverse the immunosuppressive state of the MME and reactivate anti-tumor immunity, thus enhancing the efficacy of cancer therapy.

1.5. Aim of the study

The prognostic impact of tumor infiltration patterns in BM has highlighted the clinical need to delve deeper into the biological mechanisms underlying the determination of MMPI patterns pathophysiology. A recently published study provides a detailed description of the different MMPI patterns and their association with survival rates in human brain metastasis, which provides a reliable baseline for further studies (Blazquez et al., 2020). So far, these studies focused on the infiltrative grade of the metastasis, which correlates with worse clinical outcomes, while related non-infiltrative categories to favourable prognosis.

In this doctoral dissertation, we hypothesize that IL4R-signaling in MDM/microglia is crucial for the acquisition of a metastasis-promoting macrophage phenotype. Also, we believe that the colonization patterns displayed in the MMPIs have a relevant impact on the configuration of the brain metastatic microenvironment. Thus, different breast cancer brain metastasis models displaying divergent MMPI patterns have been used in order to determine the impact of IL4R-signaling in MDM/microglia during breast cancer colonization of the CNS.

In this context, the first aim of this thesis is the establishment of a brain metastasis mouse model representing a non-infiltrative MMPI pattern. Initially, a comprehensive analysis of this with infiltrative models of brain metastasis previously established in this group will be conducted, emphasizing the effect of the different MMPI patterns on survival, colonization capacity, and immune infiltration levels.

Next, we attempt to investigate the role of IL4 as a major trigger of the pro-metastatic immunosuppressive-TAM population within the brain-MME niche. Thus, the second aim of this thesis is to determine the functional impact of IL4/IL4R signaling blockade on the brain-TAM population *in vitro* and *in vivo*, with a special focus on the characterization of the metastatic microenvironment *in vivo* and the evaluation of its therapeutic effects in combination with immune-checkpoint blockade therapy.

Collectively, this study arises in the attempt to contribute to the understanding of the pro-metastatic role of IL4R-signaling in MDM/microglia during breast cancer colonization of the brain taking into account the clinical relevance of the MMPI.

Precisely, the following aims are pursued in this study:

- 1) Establishment and characterization of a new syngeneic mouse model of brain metastasis with a displacing MMPI pattern (TUBO) *in vitro* and *in vivo*.
- 2) Characterization of the immune response within the brain metastatic microenvironment in the different MMPI models *in vivo*.
- 3) Determination of the impact of IL4/IL4R-signaling blockade in immune response activation during breast cancer colonization of the CNS *in vitro* and *in vivo*, with an emphasis on the TAM population of the brain-MME niche.
- 4) Identification of potential immune resistance mechanisms among the selected breast cancer brain metastasis model cell lines *in vitro*.

2. Materials and Methods

2.1. Materials

2.1.1. Biological materials

2.1.1.1. Cell lines

The cell lines used in this study are listed in Table 1.

Table 1: Cell lines

Name	Cell type/species	Background	Origin/source	Reference
AG TUBO	Murine breast cancer (HER2-driven)	BALB/NeuT	Prof. Christoph Klein (Germany)	(Rovero S. et al., 2000)
410.4	Murine breast cancer (TN)	BALB/c	Prof. F. Balkwill (London, UK)	(Miller et al., 1983)
4T1	Murine breast cancer (TN)	BALB/c	Prof. F. Balkwill (London, UK)	(Aslakson & Miller, 1992)

2.1.1.2. Primary cells

Bone marrow-derived macrophages (BMDM) were isolated from the bone marrow of adult mice (10-12 weeks old). Microglia and astrocytes were isolated from primary glial cell cultures of newborn mice (0-1 day old). Throughout this study BMDM will also be referred to as MDM (monocyte-derived macrophages).

2.1.1.3. Mouse strains

Adult mice (BALB/c) were purchased from Charles River (Hannover, Germany). All animals were fed a soy-free diet and kept in the animal facility for approximately 15 weeks under standard conditions. Newborn mice were bred and obtained from the animal facility of the University Hospital Regensburg and the University Medicine of Gottingen (Germany).

2.1.1.3.1. Genetically modified mice

In this project, general IL4 receptor alpha functional knock-out (IL4R α ^{-/-}) mice (MGI:2657172; Mohrs et al., 1999) were used to determine the role of IL4R-signaling in the communication between mammary

carcinoma cells and MDM/microglia. Genetically modified strains were generated using the Cre/Lox system, a powerful mammalian gene editing technique that utilizes the Cre recombinase enzyme to catalyze site specific recombination. Briefly, the Cre recombinase enzyme recognizes and excises two directly repeated loxP sites, resulting in deletion, inversion or translocation of the LoxP flanked- DNA sequence (floxed) depending on the orientation and location of loxP sites (Hyeonhui Kim et al., 2018). The murine IL4R locus is located in the distal region of chromosome 7 (the human homolog is in chromosome 16). There are two different types of IL4 receptors, however, both heterodimeric complexes contain the IL4R α subunit (see Introduction 1.4.1.). In line with this, IL4R α - deficient mice used in this project were generated by replacing exons 7 through 9 with a single loxP site following Cre-mediated excision and homologous recombination. The resulting IL4R α ^(-/-) mutant mouse lacks the transmembrane, soluble and extracellular regions of the proximal membrane of the IL-4R α , constituting a functional knockout that still retains its protein expression. Wild-type IL4R α mice (IL4R α ^(+/+)) were generated by repeatedly breeding and crossing IL4R α ^(-/-) with IL4R α ^(+/+) BALB/c mice in collaboration with Prof. C. Klein (University Hospital Regensburg, Germany) and used as control groups for further *in vivo* experiments.

To further explore the function of IL4 in macrophages *in vivo*, the Cre/loxP recombination system was applied to conditional gene targeting in BMDM. In this case, Cre would be specifically expressed under the control of the murine M lysozyme gene in monocytes/macrophages (LysM-Cre mice). Thus, BMDM-specific KO mice (IL4R α ^{/flox} LysM^{cre}) were used to investigate the role of IL4 in BMDM during the type-2 immune response. Control mice were heterozygous for IL4R α gene, with LoxP sites flanking the receptor-coding allele and no Cre recombinase (IL4R α ^{/flox} LyM^{+/-} Cre^{-/-}). In turn, the Cre/lox cell-specific knockouts were heterozygous for both the IL4R α gene, with a loxP-flanked allele, and for the Cre transgene (IL4R α ^{/flox} LyM^{+/-} Cre^{+/-}). Because the controls did not have Cre recombinase, phenotypic differences between them and the conditional-KO mice should be due to deletion of the left IL4R α allele in the Cre/lox mice. These mice were provided by Prof. C. Klein (University Hospital Regensburg, Germany).

Table 2: Overview of genetically modified mice strains

Genetically Modified Mouse	CTRL	KO
General IL4R α KO	IL4R α ^{+/+} LyM ^{+/+}	IL4R α ^{-/-} LyM ^{+/+}
Conditional IL4R α KO	IL4R α ^{/flox} LyM ^{+/-} Cre ^{-/-}	IL4R α ^{/flox} LyM ^{+/-} Cre ^{+/-}

2.1.2. Cell culture media and additives

All media and additives used for the culture of the cell lines and primary cells are listed in Table 2.

Table 2: Cell culture and additives.

Product	Company
Accutase solution	Sigma-Aldrich (Steinheim)
DMEM medium (1g/l glucose)	Merck Milipore (Berlin)
Dulbecco's Phosphate Buffered Saline (PBS) without Ca ²⁺ , Mg ²⁺	Sigma-Aldrich (Steinheim)
Fetal calf serum (FCS)	PAN Biotech (Aidenbach)
Glucose 40%	B. Braun (Melsungen)
Hank's balanced salt solution (HBSS)	Gibco/ThermoFisher (Darmstadt)
L-Glutamine-Penicillin-Streptomycin Solution	Sigma-Aldrich (Steinheim)
Normal goat serum (NGS)	Sigma-Aldrich (Steinheim)
Normal horse serum (NHS)	Gibco/ThermoFisher (Darmstadt)
Penicillin/ Streptomycin (P/S)	Merck Milipore (Berlin)
RPMI-1640 medium	Gibco/ThermoFisher (Darmstadt)
Sodium Pyruvate	Sigma-Aldrich (Steinheim)
Trypsin (1:250), 2,5% in PBS, without Ca ²⁺ , Mg ²⁺	Merck Milipore (Berlin)
Trypsin-EDTA (10X)	Sigma-Aldrich (Steinheim)
DMEM (1x)+ GlutaMAX-I	Gibco/ThermoFisher (Darmstadt)
Recombinant murine IL4	Peptotech (Germany)
LPS from <i>E.coli</i>	Enzo-Life-Science (Germany)
BSO	Sigma-Aldrich

2.1.3. Chemicals, enzymes and ready-to-use reagents.

All used chemicals, enzymes as well as other reagents are listed in Table 3.

Table 3. Chemicals, enzymes and other reagents.

Product	Company
2-Mercaptoethanol	Sigma-Aldrich (Steinheim)
Acetic Acid	Merck Milipore (Berlin)
Agarose HEEO Ultra	Carl Roth (Karlsruhe)
Albumin Fraction V (BSA)	Carl Roth (Karlsruhe)
Ammonium Persulfate (APS)	VWR (Ismaning)
Antibody Diluent	Dako (Jena)
Blotting-Grade Blocker (nonfat dry milk)	Bio-Rad (Munich)
Bovine Serum ALbumin (BSA) Standard Ampules	Gibco/ ThermoFisher (Darmstadt)
Chloroform	Carl Roth (Germany)
Deoxyribonuclease I (DNA I)	Worthington/ CellSystems (Troisdorf)
DEPC water	Carl Roth (Germany)
Diethyl Eter	Merck Milipore (Berlin)
Dimethyl Sulfoxide (DMSO)	Sigma-Aldrich (Steinheim)

DNase I (10u/μl)	Roche (Mannheim)
DNase I Incubation Buffer (10X)	Roche (Mannheim)
Ethanol	Merck Milipore (Berlin)
Ethylenediaminetetraacetiv acid (EDTA)	Merck Milipore (Berlin)
Extracellular Matrix (ECM)	R&D Systems (Wiesbaden)
ExtrAvidin-Peroxidase	Sigma-Aldrich (Steinheim)
Fluorescent mounting médium	Dako (Jena)
Glycine	Carl Roth (Karlsruhe)
Isopropanol	Merck Milipore (Berlin)
iTap Universal SYBR Green Supermix	Bio-Rad (Munich)
Laemmli loading buffer Roti-Load 1 (reducing, 4x)	Carl Roth (Karlsruhe)
Methanol	Merck Milipore (Berlin)
Na-Acetate 4.8pH	Carl Roth (Germany)
NaCl 0,9%	B. Braun (Melsungen)
Paraformaldehyde (PFA)	Merck Milipore (Berlin)
Phenol/Chloroform/Isoamyl alcohol	Carl Roth (Germany)
Phosphatase inhibitor PhosSTOP (10x)	Roche (Mannheim)
Poly-L-lysine	Sigma-Aldrich (Steinheim)
Ponceau S Solution (0,1% (w/v) in 5% acetic acid)	Sigma-Aldrich (Steinheim)
Precision Plus Protein Dual Xtra	Bio-Rad (Munich)
Rnase-free water	Invitrogen/ ThermoFisher (Karlsruhe)
RNase OUT (40 u/μl)	Invitrogen/ ThermoFisher (Karlsruhe)
Tetramethylethylendiamin (TEMED)	Sigma-Aldrich (Steinheim)
Tris-Wash Buffer (pH6)	Merck Milipore (Berlin)
Triton X-100	Sigma-Aldrich (Steinheim)
TRIzol Reagent	Invitrogen/ ThermoFisher (Karlsruhe)
Tween 20	Sigma-Aldrich (Steinheim)
UltraPUre DNase/RNase-Free Distilled Water	Invitrogen/ ThermoFisher (Karlsruhe)

2.1.4. Buffers and solutions

The antibodies and fluorescence dyes used in this study are listed in Table 4.

Table 4: Buffers and solutions.

Description	Concentration	Composition
6x DNA loading dye blue	10 mM 0.03%	Tris-Base/Tris-HCl bromophenol blue
Blotting buffer	25 mM 192 mM 20% ad 1 l	Tris-Base/Tris-HCl glycine (v/v) methanol H2O
BSA 5%	5%	(w/v) BSA in TBST
Citrate buffer	2.1 g 29,41g	Solution A: tri-sodium citrate dehydrate in 100 ml H2O Solution B: hydroxytricarballic acid in 1l H2O

	2 ml 98 ml ad 1 L	solution A solution B H ₂ O pH 6.0
Electrophoresis buffer	25 mM 192 mM 0.1% ad 1 L	Tris-Base/Tris-HCl glycine (w/v) SDS H ₂ O
HCl alcohol 0.22%	1 L 6 ml	isopropanol hydrochloric acid 37%
Kanamycin	500 mg 10 ml	kanamycin H ₂ O
Laemmli buffer (4x)	2g 5ml ⁻¹ 10 mg 40% 20% 20%	SDS in H ₂ O bromophenol blue (v/v) glycerol (v/v) stacking gel buffer v/v) 2-mercaptoethanol
MMP 5%	5%	(w/v) MMP in TBST
Peroxidase solution 3%	10% 90%	hydrogen peroxide 30% PBS
PFA solution 4%	24 g 540 ml 6–9 drops 60 ml	PFA distilled water (dH ₂ O) solve at 60 °C NaOH 10x PBS pH 7.3
Resolving gel buffer	1.5 M 2%	Tris-Base/Tris-HCl (w/v) SDS pH 8.8
RIPA lysis buffer	50 mM 150 mM 0.1% 0.5% 1% 10x 100x	Tris-Base/Tris-HCl (pH 7.2) NaCl (w/v) SDS (w/v) Na-deoxycholate Triton X-100 added fresh: phosphatase inhibitor protease inhibitor
Stacking gel buffer	0.5 M 2%	Tris-Base/Tris-HCl (w/v) SDS pH 6.8
Tris-acetate-EDTA (TAE) buffer	40 mM 1 mM 0.1% ad	Tris-Acetate EDTA glacial acetic acid H ₂ O
Tris-buffered saline with Tween20 (TBST)	20 mM 150 mM ad 1 L 0.1%	Tris-Base/Tris-HCl NaCl pH 7.6 (v/v) Tween20

Tris-EDTA (TE) buffer	5 ml 1 ml 494 ml	Tris-Base/Tris-HCl EDTA H ₂ O pH 8.0
Triton X	0.5%	0.5% (v/v) Triton X-100 in PBS

2.1.5. Antibodies and fluorescence dyes

The antibodies and fluorescence dyes used in this study are listed in Table 5.

Table 5: Antibodies and fluorescence dyes.

Name	Source	Label	Application/ Dilution	Company/ Cat. Nr.
E-Cadherin	Rabbit	-	IF (1:100)	Cell Signaling (#3195S)
Vimentin	Rabbit	-	IF (1:100)	Cell Signaling (#5741)
Phalloidin	Amanita phalloides	TRITC	IF (1:600)	Sigma-Aldrich (#P1951)
Rabbit IgG, F(ab') ₂ -TRITC	Goat	TRITC	IF (1:300)	ThermoFischer(#A16101)
Rabbit IgG, F(ab') ₂ -FITC	Goat	FITC	IF (1:300)	ThermoFischer (#31635)
DAPI	Rabbit	-	IF (1:2.000)	Sigma-Aldrich (#D8417)
Stat 6	Rabbit	-	WB (1:500)	Santa Cruz (#sc-1689)
Phospho-Stat 6	Rabbit	-	WB (1:500)	Invitrogen (#700247)
E-Cadherin	Rabbit	-	WB (1:1.000)	Cell Signaling (#3195S)
β-Cat	Mouse	-	WB (1:1.000)	Santa Cruz (E-5#sc-7963)
B-Actin (AS-15)	Mouse	-	WB (1:10.000)	Sigma-Aldrich (#A5441)
Isotype Rat IgG2b, k	Rabbit	-	FACS	BioLegend
CD11b PE conjugated	Rabbit	-	FACS	BioLegend
CD45 PE conjugated	Rabbit	-	FACS	BioLegend
CD45 AF488	Rabbit	-	FACS	BioLegend
Ck8	Rabbit	-	IHC (1:100)	Abcam (#ab59434)
Cd3	Rabbit	-	IHC (1:150)	DCS (#CI597R06)
Iba1	Rabbit	-	IHC (1:1000)	Wako (#019-19741)
Gfap	Rabbit	-	IHC (1:200)	Dake (#ZO334)
Anti Rabbit IgG, biotin (H+L) Biotin	Goat	-	IHC (1:250)	Dianova (#111-065-144)
Streptavidin HRP	-	-	IHC (1:1000)	Zytomed (#ZUC-012008)
DAB-kit	-	-	IHC (1:50)	Dako (#K3468)

2.1.6. Oligonucleotides

Table 6 reunites all oligonucleotides used for this study.

Table 6: Oligonucleotides

Name	Description	Direction	Sequence (5'-3')
mmGadph	Glycerinaldehyd-3-phosphat-Dehydrogenase	Forward	CATCTTGGGCTACACTGAG
		Reverse	CTGTAGCCGTATTCAATTGTC
mmPgk1	Phosphoglycerate Kinase 1	Forward	TGTCCAAACTAGGAGATGTC
		Reverse	CCTTGGCAAAGTAGTTCAG
mmCk8	Keratin 8	Forward	ATGAACAAGGTGGAAGTAGAG
		Reverse	ATCTCCTCTTCATGGATCTG
mmCk19	Keratin 19	Forward	CACTACTTTAAGACCATCGAG
		Reverse	ATCTGTAGGACAATCTTGGAG
mmEcad	Cadherin 1	Forward	GGATATTAATGACAACGCTCC
		Reverse	GCATTGACCTCATTCTCAG
mmVim	Vimentin	Forward	CGGCTGCGAGAGAAATTGC
		Reverse	CCACTTTCGGTTCAAGGTCAAG
mmIba1	Ionized Calcium-Binding Adapter Molecule 1	Forward	TTCAGCTACTCTGACTTTCTC
		Reverse	GAATCATCTCAAGATGGCAG
mmGfap	Glial Fibrillary Acidic Protein	Forward	AACCTGGCTGCGTATAGAC
		Reverse	CCAGCGATTCAACCTTTCTC
mmCd3	T-Cell Surface Glycoprotein CD3 Zeta Chain	Forward	GCTACTACGCTCTGCTACAC
		Reverse	TGATGATTATGGCTACTGCT
mmArg1	Arginin 1	Forward	CAAAGACATCGGTACATTGG
		Reverse	TTGTCTACTTCAGTCATGGA
mmTnf α	Tumor Necrosis Factor alfa	Forward	TCCCCAAAGGGATGAGAAGT
mmiNos	Inducible Nitric Oxide synthase	Forward	GTCTTGCAAGCTGATGGTCA
		Reverse	ACCACTCGTACTTGGGATGC
mmIl1 β	Interleukin 1 beta	Forward	GTAATGAAAGACGGCACACC
		Reverse	ACTCTGCAGACTCAAACCTCC
mmIl6	Interleukin 6	Forward	GATGGATGCTACCAAACCTG
		Reverse	CCAGGTAGCTATGGTACTC
mmIl4	Interleukin 4	Forward	TCTAGTGTTCTCATGGAGCTG
		Reverse	TTTCAGTGATGTGGACTTGG
mmIl10	Interleukin 10	Forward	GAAGACAATAACTGCACCCA
		Reverse	CATTAAGGAGTCGGTTAGCAG
mmMmp12	Matrix Metallopeptidase 12	Forward	CTTCATAAAGATGAGGCTGAC
		Reverse	TGTGCATCTCCTTGAATACC
mmCc117	C-C Motif Chemokine Ligand17	Forward	TTGGTGAGCTGGTATAAGAC
		Reverse	GACAGTCAGAAACACGATGG
mmCxCl13	C-X-C Motif Chemokine Ligand 13	Forward	GAGCTAAAGGTTGAACTCCA
		Reverse	GTTGAAATCACTCCAGAACAC
mmTgm2	Transglutaminase 2	Forward	GAATATGTCCTTACGCAACAG
		Reverse	GTTCATATCCAAGAGCATCAG
mmFn1	Fibronectin 1	Forward	TCAGATAAATCAGCAGTGGG
		Reverse	GTGTTCCAGTGTATTTGTC
mmCd11b	Integrin Subunit Alpha M	Forward	CCCATCTTTCCTGCTAATTCTG
		Reverse	AGGTTGTTGAACTGGTACTG
mmIL4R (WT)	Interleukin-4 wild type	Forward	GTACAGCGCACATTGTTTTT
		Reverse	CTCGCGCACTGACCCATCT
	Interleukin-4 knockout	Forward	CCCTTCTGGCCCTGAATTT

mmIl4R (KO)		Reverse	ACCTGTGCATCCTGAATGAT
mmIL4R LysM	Lysozyme M, myeloid specific promoter	Forward	CTTGGGCTGCCAGAATTTCTC
		Reverse	TTACAGTCGGCCAGGCTGAC
mmLysM-Cre8	Lysozyme M, Cre recombinase conjugated	Forward	CTTGGGCTGCCAGAATTTCTC
		Reverse	CCCAGAAATGCCAGATTACG
mm4select	Target gene	Forward	CCCTCAAACCTTGTCAGGGGAGGGC
		Reverse	CCCAGAAGACTCCCGCCCATCTTC
mmIl33	Interleukin 33	Forward	GAATTCTGCCATGTCTACTG
		Reverse	AAGTTCTCTTCATGCTTGGT
mmAlox5	Arachidonate 5-lipoxygenase	Forward	ATT GCC ATC CAG CTC AAC CA
		Reverse	ACT GGA ACG CAC CCA GAT TT
mmAlox15	Arachidonate 15-lipoxygenase	Forward	CTC TCA AGG CCT GTT CAG GA
		Reverse	GTC CAT TGT CCC CAG AAC CT
mmPeg2	Prostaglandin E Receptor 2	Forward	TTCTCCTGGCCATTATGACC
		Reverse	TGTAGGCAAAGATTGTGAAAGG
mmGpx4	Glutathione Peroxidase 4	Forward	GTCTGCCTGGATAAGTACAG
		Reverse	CTAGCTGAGTGTAGTTTACGT
mmHo1	Heme Oxygenase 1	Forward	AAGAGGCTAAGACCGCCTTC
		Reverse	GTCGTGGTCAGTCAACATGG
mmNqo1	NAD(P)H Quinone Dehydrogenase 1	Forward	TCTCTAGCATATAAGGAAGGAC
		Reverse	CTTATTCTGGAAAGGACCGT
mmBlvrb	Biliverdin reductase B	Forward	TAAGATTCTGCAAGAGTCAGG
		Reverse	CCAGTTAGTGGTTGGTCTC
mmFth1	Ferritin Heavy Chain 1	Forward	TACTGGAAGTGCACAAACTG
		Reverse	ATCTTGCCTAAGTTGGTCAC
mmNcoa4	Nuclear Receptor Coactivator 4	Forward	CAGTTTGTGATCTCTTTGCCT
		Reverse	TGCTCGATTCTGGTAGTCTG
mmGpx2	Glutathione Peroxidase 2	Forward	CTCAATGAGCTGCAATGTC
		Reverse	CAGGTCGGACATACTTGAG

2.1.7. Commercial kits

All commercial kits are listed in Table 7.

Table 7: Commercial kits.

Product	Company
Amersham ECL Prime Western Blotting Detection Reagent	GE Healthcare (Freiburg)
Signal Fire ECL Reagent	Cell Signaling Technology
DC (detergent compatible) protein assay	Bio-Rad (munich)
High Pure RNA Isolation Kit	Roche (Mannheim)
iScript cDNA synthesis Kit	Bio-Rad (Munich)

2.1.8. Consumables

All consumables used in this study are listed in Table 8

Table 8: Consumables

Product	Company
10 cm Petri dish (coated)	Nunc (Langensfeld)
10 cm Petri dish (un-coated)	Starstedt (Nümbrecht)
12-well plates	Starstedt (Nümbrecht)
24-well plates	Starstedt (Nümbrecht)
384-well plates	Greiner Bio-one (Frickenhausen)
6-well plates	Nunc (Langensfeld)
96-well plates	Nunc (Langensfeld)
Blades Wilkinson Classic	Wilkinson (Solingen)
Cell culture flasks (25, 75, 175 cm ²)	Starstedt (Nümbrecht)
Cell scrapper 25 cm	Starstedt (Nümbrecht)
Centrifuge tubes (15, 50 ml)	Starstedt (Nümbrecht)
Combitips advanced (0.1 ml)	Eppendorf (Hamburg)
Cover glasses (18x18 mm)	Carl Roth (Karlsruhe)
Dubois decapitation scissors	Hermle (Tuttlingen)
ES-Compresses	Hartmann (Heidenheim)
Glass Pasteur Pipetter (150, 230 mm)	Brand (Wertheim)
Hamilton microliter syringe (10 µl)	Sigma-Aldrich (Steinheim)
Metallic spacer (3.8 mm diameter)	Kig GmbH (Kirkel)
Microscope slides (25 x 75 x 1 mm)	Carl Roth (Karlsruhe)
Millicell cell culture inserts (12 mm, 0.45 µm pore size)	Merck Milipore (Berlin)
Noyes eye scissors	Hermle (Tuttlingen)
Pipette tips (10 / 100 / 1000 µl)	Sarstedt (Nümbrecht)
Polycarbonate membrane insert (6-Well, 0.4µm pore size)	BD Falcon (Heidelberg)
Polystyrene round-bottom FACS tubes (5ml)	Falcon (Amsterdam)
Reaction tubes (0.2, 0.5, 1.5, 2 ml)	Sarstedt (Nümbrecht)
Rotilabo Blotting papers (1.5 mm)	Carl Roth (Karlsruhe)
Sealing-Folie (AMPLisel, transparent)	Greiner Bio-one (Frickenhausen)
Semkin standard forceps	Hermle (Tuttlingen)
Seralon polyamide suture (DR-009, USP 7/0, EP 0.5)	Serag-Wiessner GmbH (Naila)
Serological pipettes (5, 10, 25 ml)	Sarstedt (Nümbrecht)
Sterican needle Gr. 17, 18, 20	B. Braun (Melsungen)
Steritop-Filter (0.22 µm pore size)	Merck Milipore (Darmstadt)
Tissue forceps	Hermle (Tuttlingen)
Wecker spatula	Hermle (Tuttlingen)
Whatman qualitative round filter paper (90 mm diameter)	Sigma-Aldrich (Steinheim)

2.1.9. Equipment

All laboratory equipment used during this thesis is listed in Table 9.

Table 9: Equipment

Product	Label	Company
Analytical balance	R180D	Sartorius
Autoclave	5050 ELV	Tuttnauer
Autoclave	Varioklav 135S	HP Medizintechnik GmbH
Automatic flake ice machine	Scotsman AF100	Scotsman
Block thermostat	HLC BT 130	Ditabis/HLC
Cell counting chamber	Neubauer Improved	LO Laboroptik Marienfeld
Cell culture incubator	CB 160	Binder
Cell culture incubator	Heraeus	Thermo Fisher Scientific
Centrifuge	Biofuge 15	Sepatech
Centrifuge	Biofuge fresco	Thermo Fisher Scientific
Centrifuge	Biofuge pico	Thermo Fisher Scientific
Centrifuge	CT15RE	Himac
Centrifuge	Microstar 12	VWR
Chemical balance	L610D	Sartorius
Chemical balance	SI-2002A	Denver Instrument
Chemiluminescence system	ImageQuant LAS-4000	Fujifilm
CO2 incubator	BB 6220	Heraeus Instruments
Cooling plate	CP 60	Microm
Drying cabinet	UT6200	Heraeus Instruments
Drying chamber	UT 6120	Thermo Fisher Scientific
Ductless recirculating fume hood	CaptairBio I-130	Erlab
Electric pipetting aid	Accu-jet pro	Brand
Electric pipetting aid	Pipetboy	Integra
ELISA reader	TECAN Sunrise Infinite F50	Tecan Group
Confocal laser scanning microscope	<i>FV3000</i>	Olympus
Floor centrifuge	Varifuge 3.0 RS	Heraeus Instruments
Gel imaging system	Gel Doc XR+	Bio-Rad
Heating and drying table	MEDAX	Medax
Heating/shaking block	Thermomixer 5436	Eppendorf
Heating/shaking block	Thermomixer R	Eppendorf
Incubator shaker	Unitron	Infors HT
Laminar air flow bench	LaminAir HB2472	Heraeus Instruments
Laminar flow hood	Herasafe HS18	Heraeus Instruments
LightCycler	QuantStudio 5, 384-well	Thermo Fisher Scientific
Light/fluorescence microscope	EVOS FL	Thermo Fisher Scientific
Magnetic stirring bar retriever	MR3001	Heidolph Instruments
Magnetic stirrer and heating plate	IKA RCT	Ikamag
Microliter pipette, automatical	Multipette plus	Eppendorf

Microliter pipettes	100–1000µl, 20–200µl, 2–20µl, 0.2–2µl	Gilson/Eppendorf
Microwave	8018 E	Privileg
Microwave	KOR 6D07SL	Daewoo
Mini centrifuge	ProFuge 10K	Stratagene
Mini shaker	IKA MS2	IKA Lab equipment
Mini shaker	Sunflower 3D	BioSan
pH meter	538 MultiCal	WTW
pH meter	CG842	Schott
Platform shaker	Duomex 1030	Heidolph Instruments
Power supply	Standard Power Pack P25	Biometra
Roller shaker	RS-TR05	Phoenix Intrument
Single-lens reflex camera	Canon EOS 600D	Canon
Slides scanner system	Pannoramic 250	Sysmex
Sliding microtome	HM 400 R	Microm
Spectrophotometer	NanoDrop 1000	Thermo Fisher Scientific
Spectrophotometer	NanoDrop 2000	Thermo Fisher Scientific
Stereotaxic drill	Jacobs Chuck (18,000 rpm)	Kopf Instruments
Surface shaker	Reax 3	Heidolph Instruments
Table centrifuge	5810R	Eppendorf
Table centrifuge	Allegra X-15R	Beckman Coulter
Table centrifuge	Megafuge 1.0 Sepatech	Kendro Laboratory Products
Table centrifuge	Megafuge 3.0R	Heraeus Instruments
Table centrifuge	Multifuge 3	Heraeus Instruments
Thermal cycler	PTC-200	MJ Research
Tissue float bath	GFL 1052	GFL
Transilluminator	Ultraviolet (UV) slider	Intas
Ultra-precise small animal stereotaxic instrument	Model 963	Kopf Instruments
Vortex shaker	REAX 2000	Heidolph Instruments
Vortex shaker	Vortex Genie 2	Intas
Water bath	SW-20C	Julabo GmbH
Water purification system	MilliQ	Millipore
Western blot transfer system	Trans-Blot SD Semi-Dry	Bio-Rad
Western blot transfer system	Trans-Blot Turbo	Bio-Rad

2.1.10. Software products and databases

All software products and databases used during the thesis are listed in Table 10.

Table 10: Software products and databases

Product	Purpose	Company
BioGPS (database)	Database for gene and protein function	BioGPS

CaseViewer (version 2.3)	Imaging editor for slide images	3DHISTECH Ltd.
EndNote (version X8.2)	Citation program	Clarivate Analytics
<i>FV31S-SW software.</i>	<i>Imaging processing editor for confocal images</i>	Olympus
Gen Card (versión 5.3)	Database for gene and protein function	Life Map Sciences
GraphPad Prism (version 7)	Graphs and statistics	GraphPad Software
Heatmapper (online tool)	Creating heatmaps	omicX
Image Lab (on device)	Image analysis of agarose gels	Bio-Rad
ImageJ (win64) (version 1.51s)	Analyzing data, editing pictures	Wayne Rasband
ImageQuant LAS 4000 (on device)	Chemiluminescence imaging	Fujifilm
Microsoft Office 2013	Managing data, writing text, editing pictures	Microsoft
NanoDrop (on device)	DNA/RNA measurement	Thermo Fisher Scientific
NCBI (database)	Database for genomic information, BLAST tool	NCBI
PerlPrimer (version 1.1.21)	Designing primers	(Marshall, 2004)

2.2. Methods

2.2.1. Cell culture methods

2.2.1.1. Maintenance of tumor cells

Breast cancer cell lines were grown at 37°C and 5% CO₂ in a humidified incubator. In order to passage the cells, they were washed once with PBS (Sigma-Aldrich), detached by incubation with 1mL Trypsin-EDTA (1x) (Sigma-Aldrich) for up to 10 min and Split in a ratio 1:5-1:10. For TUBO and 410.4 tumor cell lines, incubation could be as long as 15 mins, shaking the container by hand to assist in detachment. To maintain cells over a longer period, they were frozen in DMSO (Sigma-Aldrich) with 90% FCS (PAN- Biotech) and stored in liquid nitrogen. All cell lines were routinely tested for contamination with mycoplasma.

2.2.1.1.1. Assessment of proliferation

To determine the cell proliferation rates of the breast cancer cells used in this project, 5×10^4 , 1×10^5 , 1.5×10^5 , 2.5×10^5 , 5×10^5 and 1×10^6 cells per well were seeded in triplicates in 24-well plates. After 48h incubation, cells were trypsinized and quantified with a Neubauer chamber, calculating the proliferation rate as the division of the mean of cell number at 48h by the number of seeded cells.

2.2.1.2. Primary cell isolation and culture

2.2.1.2.1. Primary cultures of microglia

This method was performed for the creation of a glial culture composed of microglia and astrocytes in which the latter serve as physical support for the former, placed on the surface. In order to perform primary cultures of microglia, the brains of newborn, postnatal day 0/1 mice (P0 and P1, respectively) were isolated. First, brains were quickly displaced from the rest of the body, and the scalp and skull were removed in order to access the meninges. After placing the naked brains of newborn mice into Petri dishes containing Hanks solutions, the meninges and blood vessels from the whole brain were carefully dissected and removed, dissociating mechanically the resulting hemispheres into 2.5% trypsin (Merck Milipore) at 37°C for 10 mins. DNase I (0.4 mg/mL, Cell System) was added for further 5 min to stop the enzymatic reaction. Next, tissue was centrifuged at 4°C for 10 min, followed by cell resuspension and further cultivation in DMEM medium supplemented with 10% FCS, 100 U/mL penicillin and 100 µg/mL streptomycin (Merck Milipore) in T75 flasks coated with poly-L-lysine (200 µg/mL, Sigma-Aldrich) at 37°C and 5% CO₂ in a humidified atmosphere. The culture medium was changed after 24h, 48h and 96h. In addition to the change

of medium, glial cultures were stimulated with L929- conditioned medium, which contains macrophage colony-stimulating factor (M-CSF), a growth factor for the differentiation of monocytes into macrophages (Stanley, 1985). After 8 to 12 days, microglia were harvested by shaking them off the astrocytic monolayer with an orbital shaker incubator (Grant Bio).

The purity of microglia isolation was assessed using fluorescence-activated cell sorter (FACS) for the α M integrin (Cd11b, Biolegend) and the leucocyte common antigen (Cd45, Biolegend) as follows. Upon microglia isolation, 12×10^4 cells were distributed into a total of six FACS tubes of 5mL (BD Falcon 352052), three for compensation (8×10^4 cells) and three for physical properties analysis (4×10^4 cells). FACS tubes were centrifuged at 13.000rpm for 7min at 4°C, the supernatant discarded and the cell stained as corresponding (see Table 11).

Table 11: Compensation and antibody FACS staining procedure

Tube 1	unstained	2ml PBS 2%FBS / tube
Tube 2	CD45 AF488	0.5 μ l Ab / tube (= 0.25 μ g / tube)
Tube 3	CD45 PE	1.25 μ l Ab / tube (= 0.25 μ g / tube)
Tube 4	Iso AF488	0.5 μ l Ab / tube (= 0.25 μ g / tube) CD45 PE 1.25 μ l Ab / tube (= 0.25 μ g / tube)
Tube 5	CD11b AF488	0.5 μ l Ab / tube (= 0.25 μ g / tube) Iso PE 1.25 μ l Ab / tube (= 0.25 μ g / tube)
Tube 6	CD11b AF488	0.5 μ l Ab / tube (= 0.25 μ g / tube) CD45 PE 1.25 μ l Ab / tube (= 0.25 μ g / tube)

Next, FACS tubes were vortexed and incubated for 30min at 4°C-8°C. To each tube, 2mL of PBS with 2% FBS was added, except for the unstained tube (tube 1). Again, the tubes were centrifuged at 1200rpm for 5min at 4°C and then the supernatant was removed. The pellet was resuspended in 200-400 microlitres of PBS with 2% FBS and briefly stored at 4°C while the measurement took place on the FACSCalibur BD. The final quality of the isolated microglia is calculated as a percentage, using only these cultures with a purity of more than 85%.

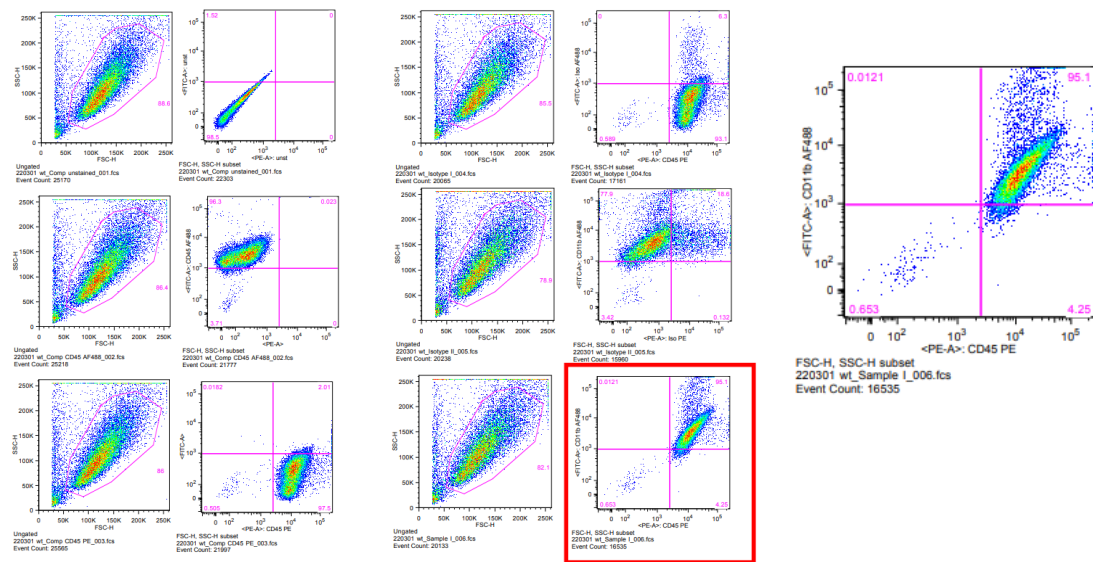


Figure 5. Example of cell count determination using flow cytometer BD FACSCalibur

2.2.1.2.2. Primary cultures of monocytes-derived macrophages (MDM)

This method was performed in 10 to 12 weeks-old BALB/c mice, following the briefly modified protocol established by Reiling et al. (2001). First, mice are sacrificed by CO₂ asphyxiation. The skin is disinfected with 70% ethanol, an incision is made on both hind legs and the skin and muscle attached to the legs are removed using scissors and tweezers (Hermle). The intact femur is obtained by cutting the knee joint distally and carefully pulling the head of the femur from the hip joint. The femur is placed in a petri dish with 70% ethanol and gently cleaned with compresses (Hartmann) to remove the remaining tissue. After cleaning and under sterile conditions, the bone marrow canal is opened by cutting PE near each joint and washed with Pluznik Medium in a coated petri dish (Nunc dish) by inserting a fine needle (Gr. 17, B. Braun) into the femoral bone cavity. The coated Petri dish allows fibroblasts, osteoclasts, and other cells present in the bone marrow to adhere to the bottom of the plate while macrophage progenitors stay as suspension cells. After 24 h incubation at 37°C and 5% CO₂, the supernatant was collected and centrifuged 10 min at 1200 rpm and room temperature (RT). The cell pellet containing MDM was resuspended in 40 ml Pluznik medium (see Table below) and seeded in four un-coated Petri dishes (Sarstedt). Cells were allowed to adhere and differentiate to mature monocyte-derived macrophages during the following six days at 37°C and 5% CO₂. Medium change was performed after 72 h. For further experiments, MDMs were harvested on day seven by the addition of 1 ml Accutase (Sigma-Aldrich) and seeded in MDM-culture medium (see Table below). Both cell culture mediums were supplemented with L929 conditioned medium, which

contains M-CSF, a growth factor that promotes bone marrow progenitors (monocytes) to differentiate into bone marrow-derived macrophages (Stanley, 1985). The CSF1 containing conditioned medium was obtained from the L929 murine fibroblast cell line, as previously described by Pfannes and collaborators in 2001 (Pfannes, Muller, Korner, Bessler, & Hoffmann, 2001). The conditioned medium was then collected from L929 cells (10×10^6), previously seeded in a T175 with 100 ml DMEM and incubated for seven days at 37°C and 5% CO₂. The conditioned medium was then centrifuged at 2000 g, filtered with a Steritop-Filter (0.22 µm pore size, Merck Millipore) and kept at -20°C.

Table 12: Composition of cell culture mediums for MDM isolation

Pluznik Medium	MDM- culture medium
DMEM	DMEM
10% FCS	10% FCS
5% NHS	15% L929 conditioned medium
30% L929 conditioned medium	
0.01mM Na-pyruvat	
0.05mM β-Mercaptoethanol	
100 U/ml penicilin	
100 mg/ml streptomycin	

2.2.2. Functional in vitro assays

2.2.2.1. Hanging Drop assay

Given its greater accuracy in representing the cellular microenvironment *in vivo* in comparison to monolayer cultures, the hanging drop method was used for monitorization of the ability of tumor cells to form a spheroid and their outgrowth over time. Tumor cell spheroids were formed by preparation of single cell suspensions of 250 cells in medium-drops (DMEM+10% FCS) having a final volume of 25µL. The droplets were placed on the inner side of the lid of a 100 mm cell culture Petri dish. The bottom of the plate was filled with 10mL of PBS to prevent dehydration of the droplets, the lid carefully inverted 180° onto it and the drops incubated for 72h at 37°C. The PBS was then removed from the Petri dish and the dish was inverted to check the quality of the spheroids via EVOS FL microscope (0h images). The best-formed spheroids were transferred into a 24MW plate containing 1ml/well buthionine sulfoximine (BSO)-stimulated culture medium (10, 25 or 50µM) and incubated up to 72h at 37°C. Control spheroids were incubated with non-stimulated medium. Photographs were taken 3, 24, 48 and 72 hours after transference and the spheroid outgrowth (mm²) was analyzed by ImageJ software. Graphics representing spheroid size variation were created with the GraphPad Prism 7 program.

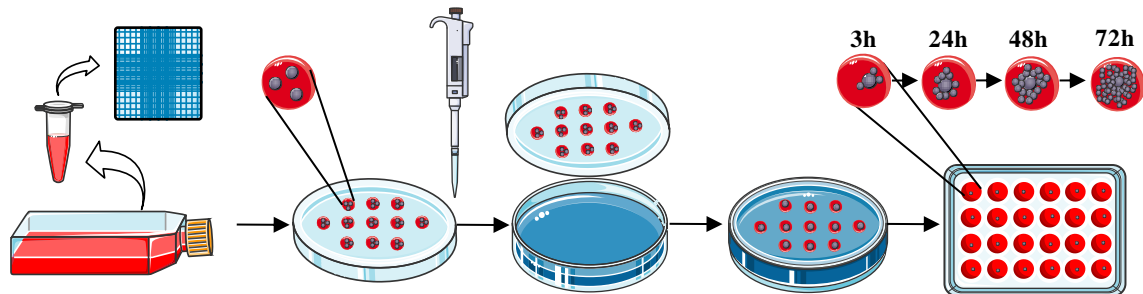


Figure 6. Schematics of Hanging Drop assay.

2.2.2.2. Chemotaxis assay

The chemotaxis assay evaluated the migration capacity of macrophages in response to cytokines/ chemoattractant molecules secreted by breast cancer tumor cells. In more detail, this method was useful to assess the potential for chemoattractant communication between macrophages and breast cancer cell lines.

Prior to the MDM/MG migration (day -2), the different tumor cells were seeded in a 6MW plate ($0,5 \times 10^6$ cells/ well/ 2ml) and incubated for 48h in culture medium (DMEM+10% FCS). The supernatant from each well was then centrifuged for 10 min at 1.300rpm and subsequently filtered with a $0,2 \mu$ micropore filter (ministart#16534-k). From the filtered medium, 500 μ l were added to a 24MW plate and, above each well, transwell permeable inserts of 3μ m polycarbonate membrane (Costar#3415) were incubated for 30min-1h at 37°C to improve permeabilization (day 0). Afterward, macrophages were added above the insert (70.000 cells / 300 μ l) and incubated at 37°C overnight (16-20h) in order to allow the cell migration. The migratory capacity of macrophages in response to supernatants from different tumor cell lines was analyzed by FACS (day 1) as previously explained. Briefly, cell count determination was performed by measurement of physical properties (size vs granularity) using a flow cytometer BD FACS-Calibur (FSC vs. SSC), without an antibody being needed to staining in a procedure similar to the one explained above (see section 2.2.1.2.1).

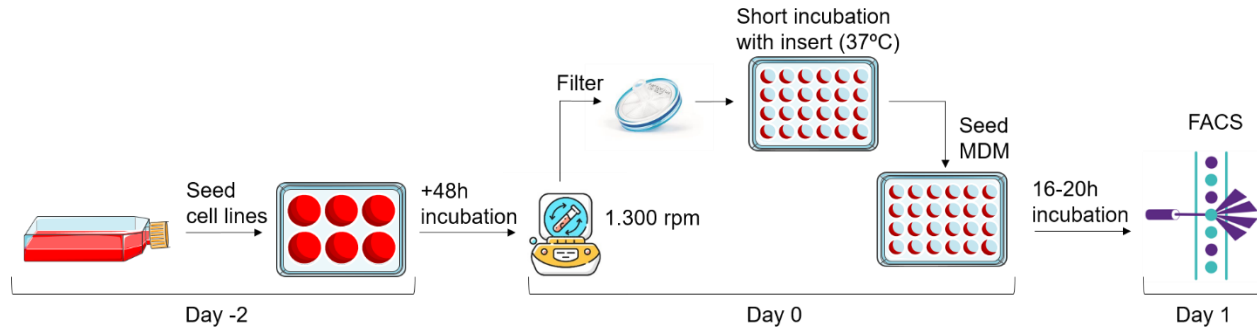


Figure 7. Schematics of Chemotaxis assay

2.2.3. *In vivo* experiments

2.2.3.1. Stereotactical intracortical injection

The brain colonization *in vivo* models were performed in 10-12-weeks-old BALB/c mice. For the establishment of the method, tumor cells were stereotactically injected in the cortical region of syngeneic mice put under anesthetics by intraperitoneal injection of the anesthetic solution (10 μ l/g KW) (see Table 13). First, the cortical area was disinfected with 70% ethanol and opened using a small midline incision with the help of a sterile scalpel. The periosteum of the right skull cup was carefully removed and the mouse was placed into a stereotaxic frame (David Kopf Instruments). The skull was placed horizontally to the surface by fixing it with rigid ear bars. Using a tooth-technical drill (David Kopf Instruments), a drill hole of approx. 1 mm of diameter was stereotactically bored 1 mm rostral and 2 mm lateral of the anatomical point bregma.

Previous to injection, cells were trypsinized and counted in a Neubauer Chamber. The desired number of cells were centrifuged and finally resuspended in 3 μ l gel matrix, consisting of 1 μ l cell culture medium and 2 μ l ECM gel (Sigma). The resulting cell suspension was mixed and drawn up in a 10 μ l Hamilton syringe (Sigma-Aldrich) with a beveled cannula. The syringe was placed in the stereotactic device holder vertically to the hole in the skull and with the open end of the cannula pointing to the left. The cannula was introduced 3.5 mm deep in the brain through the skull hole and pulled back 0.5 mm in order to form a small cavity for the cell content. Cells were injected directly into the cortical region for 1 min, with the needle remaining in the same position for two mins more to assure the establishment of the cells in the brain parenchyma. While removing the needle, the lesion was washed with NaCl and the remaining damaged skin was stitched up

with a polyamide suture (Seralon, Serag-Wiessner GmbH). Finally, painkillers were injected subcutaneously (5 µg/g KW) and mice were laid down on a thermal plate (Medax) until recovery from anesthesia.

Table 13: Composition of anesthetic solution and painkiller for stereotactical intracortical injection of tumor cells

Anesthetic solution	Painkiller
Ketamin 100 mg/Kg	Rimadyl 5mg/kg
Domitor 0,25 mg/kg	
NaCl ad 10ml	

2.2.3.2. Immune checkpoint inhibitor therapy

Mice undergoing immunotherapy were 11-13 weeks old at the time of the intervention. Animals were injected every 2-3 days with a combined cocktail of immune checkpoints inhibitors including anti-CTLA4 (Cytotoxic T-Lymphocyte Antigen 4) (BioXcell 731719A2 #BPO164; CD152, clone 9D9; 8,5mg/ml) and anti-PD1 (Programmed Death-1) (Ceinco 0419L420; CD279; 5,2mg/ml). Injection volumes were calculated individually for each mouse at a dose of 10mg/kg body weight. A total of 9 injections were performed per animal. The antibodies were mixed with PBS to a final volume of 100 µl per mouse. Upon treatment, mice were monitored daily for neuropathological status according to section 2.2.3.3.

2.2.3.3. Animal maintenance and monitoring

Following stereotactical intracortical injection, mice were regularly monitored by attending to changes in their behaviour, physical fitness, weight or motor skills. Animals were weighed at least once a week and submitted to the Hanging Wire test in case of showing neuropathological symptoms and motor deficits. This test allows the evaluation of assessing muscle strength, coordination, and orientation of the animals, usually damaged in event of metastatic outgrowth (Blazquez et al., 2018). According to their health status, each mouse was individually evaluated as follows:

Table 14: Animal scoring after stereotactical intracortical injection

Score	Description of symptoms	Actions
I	No abnormalities: Coat smooth, shiny. Normal behaviour (sleeping, curiosity, social behaviour)	No measures required: further observation and weight control (at least 1-2 times per week)
II	Weight loss <10%: Dull coat, dull eyes. Unusual behaviour (impaired motor function, hyperkinetics)	Close observation: weight check (at least every 2 days)
III	Weight loss <20%: Abnormal posture, high muscle tone. Disturbed behaviour (isolation, expression of pain, apathy). Wound healing disorder	Close observation: weight control (at least 1 x daily). Hanging wire test
IV	Weight loss ≥20%: Convulsions, paralysis. Unacceptably disturbed behaviour (e.g. automutilation)	Immediate termination

2.2.3.4. Perfusion and organ isolation

Symptomatic and surviving animals were perfused with PBS for organ-specific studies. For this purpose, the animals were first anaesthetized with Ketamin (10%) and Domitor. Only when they were deep asleep, an incision was made in the abdomen. The thoracic cage was exposed and the peritoneum was scraped until the heart could be seen. Eventually, the ribs could be fractured to enlarge the field of vision. The heart was immobilized with forceps, a needle was injected into the left main heart chamber and a small opening was made in the right cardiac atrium to allow blood to drain out during PBS infusion. Thus, blood was progressively removed from the circulatory system, washing out also the cerebral vasculature and hardening the brain. Immediately afterward, the animal was decapitated and the brain separated from the skull. The animal's brain was removed from the skull, the olfactory bulbs were removed and the anterior parts were separated as the first samples. These were then subjected to shock freezing with liquid nitrogen and stored at -80°C. These samples were subsequently used for RNA isolation and gene expression analysis by quantitative real-time polymerase chain reactions (qRT-PCR) (see 2.2.6.2.3.). The rest of the brain was fixed in PFA4% for 48h, washed and stored in PBS until embedding in paraffin and further subsequent immunohistochemical (IHC) staining. The liver, lungs, and spleen were also collected and stored under both procedures to support future research beyond the scope of this project.

2.2.4. Protein biochemistry

2.2.4.1. Protein isolation

Lysates from whole cells were generated by seeding 1×10^6 cells per well in 6-well plates. After overnight adherence at 37°C and 5% CO_2 , cells were washed once with PBS and subsequently detached from the well with a cell scraper in 50-100 μl RIPA lysis buffer mixed with protease inhibitors and phosphatase inhibitors (Roche). Lysates were immediately vortexed, placed on ice for at least 30 min and then centrifuged for 10 min at 15,000 rpm and 4°C to pellet cell debris and DNA. Supernatants were collected and finally stored to -20°C .

2.2.4.2. Protein quantification by Lowry assay

The total protein concentration levels of the samples were determined by the DC (detergent compatible) protein colorimetric assay (Bio-Rad). The reaction used in this method is similar to the well-documented Lowry assay (Lowry, Rosebrough, Farr & Randall, 1951) but briefly modified to obtain faster results. The assay is based on the reaction between the protein and copper ions at alkaline pH, which results in the formation of complexes that are subsequently reduced to monovalent cations able to react with a Folin reagent. This reaction of Folin reagent by the copper-treated protein leads to color development, measurable by spectrophotometer (Tecan) at 750nm concerning a BSA standard curve (Gibco) (Peterson, 1979). The total protein concentration is exhibited by a color change of the sample solution in proportion to the protein concentration. In this study, the samples of interest were mixed with ddH₂O in a ratio of 1:5 and the assay was carried out according to the manufacturer's instructions.

2.2.5. Western Blot

2.2.5.1. SDS-PAGE

The Western Blot technique was used to analyze the protein expression in whole-cell lysates. For that purpose, proteins were first separated according to their molecular weight by discontinuous SDS polyacrylamide gel electrophoresis (SDS-PAGE) (Laemmli, 1970), consisting of two separate gels cast at different pH values. First, the separating/resolving gel (10%) is prepared and, after polymerization the second gel, the sharpening/stacking gel (5%) is placed on top of the first. With the help of a comb, columns are generated on the surface of the stacking gel, on which the protein samples (10-20 μg) were previously mixed with 4x Laemmli loading buffer (Carl Roth) and heated for 5 min at 95°C will be deposited. This

loading buffer contains 2-mercaptoethanol which reduces the protein disulfide bonds. Additionally, the buffer also comprises negatively charged SDS, which covers sampled proteins and applies an anionic charge in proportion to the protein mass. Thus, proteins in the separating gel migrate towards a positively charged anode through an acrylamide mesh created by the gel solely influenced by their molecular weight, with smaller proteins migrating faster. The samples loaded onto the gel were focused on the stacking gel for 30 min at 90 V and subsequently, proteins were resolved for around 90 min at 130 V. For determination of the protein size, a protein standard (Bio-Rad) was applied.

Table 15: Composition of stacking and resolving gels

Reagent/ solution	Stacking gel (5%)	Resolving gel (10%)
ddH ₂ O	3450 µl	3950 µl
Acrylamide/Bisacrylamide (30%)	830 µl	3350 µl
Resolving gel-buffer	-	2500 µl
Stacking gel-buffer	630 µl	-
APS (10% w/v)	50 µl	100 µl
TEMED	5 µl	10 µl

2.2.5.2. Western Blot development

After electrophoresis, the resolving gel was introduced into a blotting complex composed of two sheets of Whatman blotting paper (Carl Roth) on each side and a nitrocellulose membrane previously equilibrated in a transfer buffer placed between them. The resolving gel was put on top of the nitrocellulose membrane and the blot sandwich was introduced in a semi-dry transfer system at 15 V for 90 min at RT. After blotting, and to confirm transfer efficiency, the membrane was routinely stained with 0.5% Ponceau S (Sigma-Aldrich) as a loading control. Next, in order to saturate unspecific binding sites, the membrane was blocked for 1h in 5% MMP (Bio-Rad) or 5% BSA (Carl Roth) in TBST at RT and subsequently incubated with specific primary antibodies overnight at 4°C in the corresponding blocking solution (MMP or BSA). Over a period of 30 min, the membrane was washed three times with TBST and then incubated with secondary antibodies conjugated to horseradish peroxidase (HRP) for 1 h at RT in the corresponding blocking solution. The enzyme HRP catalyzes the oxidation of luminol producing a chemoluminescence signal measurable in a biomolecular imager. After final incubation the membrane is rinsed again three times in TBST for 5 min each and prepared for chemoluminescence signal detection using the ECLPrime detection reagent (GE Healthcare) in the LAS-4000 Imager (Fujifilm). Lastly, Protein expression was further quantified by using

ImageJ software. Intensities of bands were numerically calculated, associating the ratio of protein of interest to the corresponding loading controls [β -actin or heat shock protein 90 (HSP90)].

TBST (1x):

- 20 mM Tris 2.4 g
- 137 mM NaCl 8 g
- H₂O bidest. ad 1 l (adjust to pH 7.6)
- 0.1% (v/v) Tween-20 1 ml

Transfer buffer (1x):

- 25 mM Tris 3 g
- 192 mM glycine 14.4 g
- 20% (v/v) methanol 200 ml
- H₂O bidest. ad 1 l (adjust to pH 8.3)

2.2.6. Gene expression analysis

2.2.6.1. RNA methods

2.2.6.1.1. Isolation of total RNA from murine tissue samples

The isolation of total RNA from murine brain metastases samples was carried out with the TRIzol (Invitrogen) reagent. After adding 200 μ l chloroform (Carl Roth) to small tissue samples, mixing and incubating for 5 min at RT, samples were homogenized in 1ml TRIzol and subsequently centrifuged at 20000 g for 15 min at 4°C. Only the upper phase of the three phases resulting from the centrifugation was transferred to a new tube and mixed with 500 μ l of isopropanol. Next, the sample was incubated for 10 min at RT, followed by centrifugation at 13000 g and 4°C for 30 min to allow the precipitation of the RNA. The pellet was washed in 1 ml 70% ethanol at 20000 g and 4°C for 5 min, air dried for 5-10 min and resuspended in 50 μ l DNA digestion mix in order to remove contaminating DNA. After 20 min incubation at 37°C, the remaining RNA was purified by adding 150 μ l nuclease-free water (Invitrogen) and 200 μ l phenol/chloroform/isoamyl alcohol (Carl Roth). The sample was vortexed for 30 sec and subsequently centrifuged for 2 min at 20000 g and 4°C. Again, the upper aqueous phase containing the RNA was transferred to a new tube, adding 20 μ l sodium acetate (3 M, pH 4.8) (Carl Roth) and 200 μ l isopropanol and incubating for 30 min at 4°C. Afterward, and in order to precipitate the RNA, samples were centrifuged for 30 min at 20000 g and 4°C and the resulting pellet was washed twice in 1ml 70% ethanol for 5 min each

at 20000 g and 4°C and then air-dried. The RNA was resuspended in 20 µl nuclease-free water and its purity and concentration were determined at the NanoDrop ND-1000 spectrophotometer (Peqlab).

DNA digestion mix:

- | | |
|--|--------|
| • DNase I (10 U/µl, Roche) | 1 µl |
| • RNase OUT (40 U/µl, Invitrogen) | 0.5 µl |
| • DNase I incubation buffer (10x, Roche) | 5 µl |
| • Nuclease-free water | 43.5µl |

2.2.6.1.2. Isolation of mRNA from eukaryotic cells

To isolate mRNA from culture cells, the spin column-based High Pure RNA isolation kit (Roche) was used according to the manufacturer's instructions. First, 0.5×10^6 cells were seeded in 6-well plates and allowed to adhere overnight at 37°C and 5% CO₂. After washing once with PBS, cells were lysed 400 µl of the lysis/binding buffer supplemented with 200 µl PBS. This buffer, consisting in RNases inactivators, Triton X-100 and guanidine hydrochloride, mediates permeabilization of the cell membrane and induces protein denaturation. After cell lysis, samples were vortexed for 15 sec to help cell lysis, applied onto a spin column consisting of glass fiber fleece and centrifuged at 8000 g for 15 sec. While proteins, salts and cellular debris are eluted during centrifugation, nucleic acids strongly bind to the column, ensuring the capture of DNA and RNA in the spine. The contaminating DNA was digested directly on the column by incubation with DNase I for 15 min at RT and the remaining RNA was washed three times. The isolated RNA was eluted from the column by adding 50 µl nuclease-free water and its purity and concentration were measured with the NanoDrop ND1000 spectrophotometer (Peqlab).

2.2.6.1.3. Reverse transcription

Gene expression changes were analyzed by qRT-PCR. For that purpose, the isolated RNA was transcribed into complementary DNA (cDNA) with the iScript cDNA synthesis kit (Bio-Rad). Briefly, the RNA-dependent DNA polymerase enzyme (reverse transcriptase) binds to the random hexamer oligonucleotides and oligo (dT) primers that are contained in the kit, which are complementary to the poly-A tail of eukaryotic mRNA, allowing the reverse transcription of all mRNA in the sample. For each sample, 1µg of total RNA (template) was mixed with 4µl of 5x iScript reaction mix, 1µl of the iScript reverse transcriptase enzyme and nuclease-free water to a final volume of 20µl. The prepared reaction mix was then incubated in a thermal cycler (DNA Engine, Bio-Rad) for 5 min at 25°C to anneal the primers, followed by 30 min at

42°C to allow cDNA synthesis. Finally, the thermal cycler was raised to 85°C for 5 min, causing the enzymatic reaction to stop by degradation of the reverse transcriptase. Once they cool down, each sample was diluted in a ratio of 1:5 with nuclease-free water and kept at -20°C.

2.2.6.1.4. Quantitative real-time PCR (qRT-PCR)

Quantitative real-time PCR (qRT-PCR) was used to analyze changes in gene expression. This method maintains the same basic principle as conventional PCR but uses SYBR Green as a detection marker, an asymmetric cyanine dye that intercalates the double-stranded DNA sequence and allows quantification of the DNA templates. The DNA-dye complex absorbs blue light (λ_{max} 497nm) and emits green light (λ_{max} 520nm), yielding information on DNA amplification and its relative concentration. First, a hot-start iTaq DNA polymerase was activated (95°C for 12 min), allowing amplification of the gene of interest (GOI) for 40 cycles in a coordinated process of DNA denaturation (95°C for 15 s) followed by annealing of gene-specific primers and product extension (60°C for 1 min). Every cycle increases the copy number of GOI and, proportionally, the fluorescent signal intensity led by SYBR Green dye, allowing the fluorescent signal to be plotted against the number of cycles. The cycle number at which the fluorescence reaches the threshold level is known as the Ct value and was normalized to the expression of two house-keeping genes (HK) (=ΔCt value). A final step in the qRT-PCR program induces a slow increase of temperature that allows the melting curve analysis by constant measurement of the Green fluorescent, informing of the melting point of the amplified DNA.

The primers used in this study were designed as described in 1.2.6.1.4.1 and are listed in Table 6. First, a reaction mix including 5.6 μl iTaq Universal SYBR Green Supermix, 0.6 μl of forward and reverse primer mixture (10 μM) and 1.8 μl nuclease-free water per cDNA-triplicated sample was prepared. For each gene, 8 μl of the prepared reaction mix was pipetted into a 384-well plate (Greiner Bio-One) in triplicates and 2 μl cDNA solution (10 ng) diluted in nuclease-free water in a ratio 1:1 was added to each well. The plate was then sealed and centrifuged at 400 g and 4°C for 5 min. Finally, qRT-PCR was carried out using the QuantStudio 5 Real-Time PCR System according to the following protocol (Table 16) and analyzed with the QuantStudio Design & Analysis software. Housekeeping genes *Gapdh* and *Pgk1* were used as references to calculate the relative gene expression of murine cell line and brain tissue samples. The purity of qRT-PCR products was determined by analysis of the melting curves. Negative controls (non-template control; non-primer control) were included.

Table 16: Protocol of qRT-PCR program

Step	Temperature	Time	Cycles
Activation of Taq DNA polymerase:	95°C	12 min	
Denaturation:	95°C	15 s	40
Annealing and elongation:		1 min	40
Melting curve analysis:	95°C	15 s	
	60-95°C	2°C/min	

2.2.6.1.4.1. Establishment of primers for qRT-PCR reactions

Primer pairs for qRT-PCR analyses were designed with the PerlPrimer software (version 1.1.2.1, SourceGorge.net; Marshall, 2004). Δ Ct-method assumes 100% amplification efficiency, so reliable analysis of relative gene expression requires primers efficiency analysis before PCR. For each GOI, several different primer pairs were designed and tested for efficiency to choose the most suitable ones, assuming 100% primer efficiency for those able to exactly duplicate the PCR product in each PCR cycle. To test primer efficiency, positive controls were chosen from the BioGPS database (C. Wu et al., 2009), which shows cell lines and tissues with high GOI expression. Briefly, this test involves preparing serial dilution series of cDNA of known concentration from the positive controls. Subsequently, qRT-PCR was performed as described in 2.2.6.1.4. and the measured Ct values plotted against the amount of input cDNA. The slope of the resulting graph was calculated by the QuantStudio Design & Analysis software, in which a slope of -3.33 equals a primer efficiency of 100%. Finally, primers with an efficiency of 90-110% were chosen for further analysis. Heatmap graphics were created with GraphPad-Prism technology.

2.2.6.2. DNA methods

2.2.6.2.1. Isolation of total DNA from eucaryotic cells

Purification of total genomic DNA from eukaryotic cells was carried out using a microcentrifuge according to QIAamp DNA Mini Blood Mini Handbook Kit's instructions (QIAGEN). Briefly, cells grown in a monolayer were detached from a 6MW plate using a cell scraper. Appropriate number of cells (5×10^6 cells max.) were transferred to a 1,5ml microcentrifuge tube and centrifuged for 5 min at 300x g. Without disturbing the pellet, the supernatant was completely discarded, and cell pellet was resuspended in PBS to a final volume of 200 μ l. For protease digestion, 20 μ l proteinase K was added to the sample. Afterward,

efficient lysis of the sample was ensured by adding 200µl of AL Buffer, pulse-vortexing for 15s and incubating in a heating block at 56°C for 10min. The microcentrifuge tube was briefly centrifuged, 200µl of 96-100% ethanol was added, shaken for 15 seconds and briefly centrifuged again. The resulting mixture was applied to a spin column (in a 2ml collection tube) and centrifuged a 6000x g for 1min. The spin column was then placed in a clean 2 ml collection tube, carefully opened and 500µl of AW1 buffer was added without wetting the ring. Subsequent centrifugation of the mixture at 6000x g for 1 min with AW1 allowed a stringent wash with low guanidine concentration. Next, as previously, the centrifuge column was placed in a new collection tube and the tube containing the filtrate discarded. The freshly transferred spin column was carefully opened and 500µl of AW2, a Tris-based ethanol solution, was added to remove salts by centrifugation at maximum speed (~20000x g) for 2 min. To reduce the chances of Buffer AW2 carryover, the spin column was placed in a new 2 ml collection tube and subjected to final centrifugation at full speed for 1min. Finally, the spin column was placed in a clean 1.5 ml microcentrifuge tube and 3 elution washes with AE buffer (50µl) were performed independently. In each case, loading with AE buffer was followed by a 5-min incubation at RT (15-25°C) before each centrifugation (6000x g for 1min) to increase DNA yield. DNA concentration and purity were measured with the NanoDrop ND-1000 spectrophotometer (Peqlab) (approximately 150ng/µl were obtained from 10⁶ cells). DNA samples were long-term stored at -30 to -15°C after elution with Buffer AE.

2.2.6.2.2. Isolation of total DNA from tissue samples

The QIAmp DNA Mini Kit (QIAGEN) was used to purify DNA from the murine ear and brain metastases samples. First, the amount of tissue (murine ear) was determined and reduced to a maximum of 25 mg. Pieces of mouse ear were cut into small fragments, placed in a 2ml microcentrifuge tube and digested with 180µl of tissue lysis buffer (ATL buffer). Immediately afterward, and to increase homogenization, the tissue sample was mechanically disrupted with tissue grinding pestles. Then, 20µl of proteinase K was added to the sample to remove endogenous nucleases, vortex mixed and incubated at 56°C for 16-20h (overnight lysis). The 2 ml microcentrifuge tube was centrifuged briefly to remove droplets from inside the lid and 200 mL of lysis buffer with guanidine salts (AL) was added to improve the binding of the column and detergent. The semi-lysed sample was incubated at 70°C for 10min after mixing by pulse vortexing for 15s. Subsequently, the fully lysed sample was washed 1) with ethanol (200µl added, centrifuged at 8,000rpm for 1min) and 2) with concentrated wash buffers AW1 and AW2 (500µl, centrifuged at 8,000rpm for 1 and 3min, respectively) discarding the tube containing the filtrate and maintaining the spin column at each step. The washing phase was completed by placing the spin column in a new 2ml collection tube and centrifuging

at maximum speed for 1min. Finally, 50µl of elution buffer (AE) was added to the spin column and centrifuged at 8,000rpm for 1min. To increase DNA yield, the elution step was tripled and the elution buffer incubated for 5 mins before each centrifugation step.

2.2.6.2.3. Conventional PCR

Validation of mice genetic modification was performed by the Polymerase Chain Reaction (PCR). This biochemical method allows determining the presence or absence of specific genomic DNA sequences using DNA sequence amplification. All procedures were performed on ice. Following DNA isolation, all essential components for the reaction are mixed in the so-called standard master mix (MM) (see table 17). Subsequently, this MM is heated up to 94°C, separating the double helix of DNA into two pieces of single-stranded DNA (initial denaturation). Then, a thermostable DNA polymerase enzyme (PAN-Taq) synthesizes two new copies of the original DNA (duplication) by adding complementary deoxynucleoside triphosphates (dNTPs) to each of the single-stranded DNA (annealing). The use of thermocyclers allows repeating the process in a highly efficient manner, performing 30 to 40 denaturing – synthesizing - elongating cycles (elongation) within approximately 2 hours and leading to more than a billion exact copies of the original DNA sequence (Table 18). Final volume of 20 µl per sample.

Table 17: List of essential components included in the master mix (MM) for the PCR

Reagent	Concentration	Volume [µl] per sample
Buffer-PCR	10x	2
MgCl ₂	25mM	1,6
dNTPs	10mM	0,5
BSA	20mg/ml	0,25
PAN-Taq	5 U/ml	0,1
H ₂ O-PCR	-	9,55
3'Primer (8µM)	8µM	1
5'Primer (8µM)	8µM	1
DNA sample/ template	-	4

Standard MM for each sample was multiplied by the number of primer pairs and the number of samples. Then, the MM was divided into as many centrifuge tubes as there were pairs of primers, adding the corresponding pair of primers to each of the tubes. In this study, 5 different primers were used to analyze

gen expression modifications in BALB/c mice. Depending on the type of primer pair, the thermal cycler modifies the temperature and duration of the different steps in each cycle (Table 18).

Table 18: Protocol of PCR program

Primer	Initial denaturation	Denaturation	Annealing	Elongation	Extended elongation	Cycles
E10 + 16 (KO)	94°C/1min	94°C/30 s	59°C/30 s	72°C/1min	72°C/5min	35
E8 + E8 (WT)	94°C/1min	94°C/30 s	57°C/30 s	72°C/1min	72°C/5min	40
Lys1 + Lys2	94°C/1min	94°C/30 s	58°C/30 s	72°C/50 s	72°C/5min	35
Lys1 + Cre8	94°C/1min	94°C/30 s	58°C/30 s	72°C/50 s	72°C/5min	35
P5 + P6	94°C/1min	94°C/30 s	66°C/30 s	72°C/30 s	72°C/7min	30

2.2.6.2.3.1. Establishment of primers for conventional PCR

Primer pairs for PCR genotyping analysis were ordered from Eurofins Genomics. According to the manufacturer's instructions, the lyophilized primers were rehydrated before use with nuclease-free water to obtain a final concentration of 8µM. After dilution, the primers were stored at -20°C. For genotyping of BALB/c mice, five different primer pairs were used. The length of the amplicon product indicated the presence/absence of the genomic sequence of interest.

2.2.7. Staining

2.2.7.1. Immunofluorescence staining

Cellular localization of E-cadherin (transmembrane cell adhesion protein), Vimentin (intermediate filament of mesenchymal origin) or Phalloidin (phallotoxin that selectively binds to actin filaments) was visualized with immunofluorescence (IF) stainings. The staining procedure started with the washing of the coverslips or slides with PBS and the subsequent cell membrane permeabilization (0.5% Triton X solution). Next, samples were blocked to prevent non-specific background binding of the primary antibody (1% BSA) and cells were then stained with primary antibody against E-cadherin, Vimentin or Phalloidin for 1-2h (see below). In the case of non-conjugated primary antibodies, a secondary FITC-conjugated antibody was added for 1 h to bind to the primary antibody. Lastly, DAPI was used for the visualization of cell nuclei. Negative controls (only secondary antibody) were performed to exclude non-specific binding of a secondary antibody and unspecific staining. All images were taken with an *FV3000 confocal* laser scanning microscope (Olympus).

2.2.7.1.1. Staining of MG/ MDM

Cell morphology studies are often related to the visualization of the cytoskeletal structures of the cell under microscopy. In this context, phalloidin, a phallotoxin derived from the death fungus (*Amanita phalloides*), is a highly selective bicyclic peptide that binds to actin filaments (also known as F-actin) present in most eukaryotic cells. Phalloidin is often conjugated to a fluorescent dye, such as TRITC, allowing cellular structures to be visualized under microscopy.

2×10^5 cells diluted in DMEM medium supplemented with 10% FBS and 15% L929 were seeded on glass coverslips pre-treated with ECM (1:4 with DMEM medium) and incubated overnight at 37 °C in 24-well plates. After fixation with 500 μ l of 4% PFA for 10 min at RT, coverslips were washed three times with 500 μ l PBS for 5 min. Staining protocols were performed as indicated in Table 19. Afterward, the glass coverslips were inverted and placed upside down on slides with DAKO fluorescent mounting medium. They were left to dry at RT for a minimum of 2 hours prior to storage at 4°C.

Table 19: Phalloidin staining protocol

Reagent	Dilution	Volume	Incubation
PBS wash		500 μ l	3 x 5 min
0,5% Triton-X in PBS		500 μ l	10 min
PBS wash		500 μ l	3 x 5 min
1% BSA (blocking buffer)		500 μ l	30 min
PBS wash		500 μ l	3 x 5 min
Phalloidin-TRITC in blocking buffer	1:600	400 μ l	2 h
PBS wash		500 μ l	3 x 5 min
DAPI -staining	1:2000	400 μ l	5 min
PBS wash		500 μ l	3 x 5 min

2.2.7.1.2. Staining of tumor cells

Tumor cells ($\sim 5 \times 10^4$) were seeded on ECM-treated coverslips (ratio 1:4) and incubated for 24h at 37°C in a 24- multiwell plate. Cells were then washed once with 300 μ l PBS, fixated with 300 μ l 4% PFA for 10 min at RT and further washed twice with 500 μ l PBS for 5min. The staining procedure was performed as described in the table above (Table 19). After staining, coverslips were inverted, placed onto slides with fluorescent mounting medium (DAKO) and allowed to solidify in darkness for 12-24 h at 4 °C. Slides were stored at 4°C. Images were obtained from FV3000 confocal microscope (FV31S-SW Olympus).

2.2.7.1.3. Staining of tumor cell spheroids

Spheroids created with 250 tumor cells were visualized using the EVOS FL microscope at 4x and 10x magnification and pre-selected prior to staining. The finest spheroids were transferred to chamber slide systems (ThermoFisher) and incubated in DMEM+ 10% FCS medium for 16h at 37°C to allow adhesion. Subsequently, the medium was very carefully aspirated from the chamber to avoid suction of the spheroid, washed once with 500µl PBS and fixed with 500µl 100% methanol stored at -20°C for 10 mins on ice. Then, the methanol was removed from the well, leaving a remainder of approximately 200µl and allowed to evaporate at RT. When the chamber slide- wells were completely dry, spheroids were washed twice with 500µl PBS and stained with anti-E-Cadherin and anti-Vimentin antibodies as indicated in the table below (Table 20). After staining, the slides were separated from the chamber according to the manufacturer's instructions. The spheroids were coated with coverslips dipped in fluorescent mounting medium (DAKO) and allowed to solidify in darkness for 12-24 h at 4 °C. Slides were stored at 4°C. Images were obtained from FV3000 confocal microscope (FV31S-SW Olympus).

Table 20: Tumor cell spheroids staining protocol

Reagent	Dilution	Volume	Incubation
PBS wash		500µl	3 x 5 min
0,5% Triton-X in PBS		500µl	10 min
PBS wash		500µl	3 x 5 min
1% BSA (blocking buffer)		500µl	30 min
PBS wash		500µl	3 x 5 min
1°Antibody in blocking buffer	1:100	400µl	2 h
PBS wash		500µl	3 x 5 min
2°Antibody in blocking buffer	1:300	400µl	1h
PBS wash		500µl	3 x 5 min
DAPI -staining	1:2000	400µl	5 min
PBS wash		500µl	3 x 5 min

2.2.7.2. Staining of brain tissues

With the collaboration of the Institute of Pathology of the University Hospital Regensburg, collected brain tissues were routinely processed into cassettes, dehydrated and embedded in paraffin. The use of a sliding microtome allowed brain section into slices of 3 µm, which floated on a warm water bath subsequently placed on glass slides by a technical assistant. Slices were allowed to dry overnight at RT and warmed in an oven at 60 °C for 30 min on the next day. Decreasing alcohol concentration series consisting of short

changes of xylol, alcohol and water (see table below) allowed fixation of slices, proceeding to performance of different staining protocols according to the investigated targets. In all cases, samples were afterward subjected to increasing alcohol concentration series consisting of short changes of water, alcohol, and xylol to dehydrate the tissue. Samples were finally sealed with coverslips and scanned at the Institute of Pathology of the University Hospital Regensburg using the Pannoramic 250 slides scanner system. The CaseViewer software was used for the visualization of stained samples.

Table 21: Alcohol concentration series for staining of brain tissue

Decreasing alcohol concentration series		Increasing alcohol concentration series	
Reagent	Incubation	Reagent	Incubation
Xylol	5-10 min	Deionized water	short
Xylol	5-10 min	70% EtOH	3-5 min
100% EtOH	3-5 min	96% EtOH	3-5 min
100% EtOH	3-5 min	96% EtOH	3-5 min
96% EtOH	3-5 min	100% EtOH	3-5 min
96% EtOH	3-5 min	100% EtOH	3-5 min
70% EtOH	3-5 min	Xylol	5-10 min
Deionized water	short	Xylol	5-10 min

2.2.7.2.1. Hematoxylin and eosin staining

After hydrating the tissues, slices were stained with the nuclear dye hematoxylin, washed, and counterstained with eosin. Classically, hematoxylin and eosin (H-E) staining have been used to visualize cell morphology in tissue sections and to distinguish among different tissue types based on its capacity to stain nucleic acids in blue-purple (hematoxylin) and proteins in pink (eosin). Accordingly, H-E was used to differentiate between blue cell nuclei and pink cytoplasm and extracellular matrix in stained tissues (Cardiff et al., 2014) (Table 22).

Table 22: H-E staining protocol

Reagent	Incubation
Hematoxylin	5 min
Water bath (37°C)	5-10 min
72% dH1O/ 28% HCL alcohol 0.22%	Short (10 sec)
Water bath (37°C)	5-10 min
Eosin + 1drop 100% acetic acid	3 min
Water bath (37°C)	3 min

2.2.7.2.2. Immunohistochemical stainings

Morphological features of brain metastases were evaluated performing different immunohistochemical stainings. For visualization of the MMPI patterns, brain slices were stained against the mesenchymal marker vimentin (Vim) and the epithelial marker cytokeratin-8 (Ck8). For evaluation of the MME, brain slices were stained with allograft inflammatory factor 1 (Iba1) to detect microglia/macrophages; astrocytes, with glial fibrillary acidic protein (Gfap); and T cells, with cluster of differentiation 3 (Cd3). The different staining protocols were performed with technical assistance and performed as described in the following tables:

Table 23: IHC staining protocols for Cd3, Ck8 and Iba1

Reagent	Incubation
1x Target Retrieval solution, citrate pH 6.1	30 min 330W, allow cooling
Dionized water	3x, short (10 sec)
Tris wash buffer (pH6)	10 min
100µl 3% peroxidase solution	10 min
Tris wash buffer (pH6)	10 min
100µl antibody diluent	20 min
100µl antibody in antibody diluent	overnight ar RT
Tris wash buffer (pH6)	10 min
100 µl Rabbit IgG (H+L)-Biotin (1:250) in antibody diluent	1h RT
Tris wash buffer (pH6)	10 min
100 µl ExtrAvidin-Peroxidase (1:1000) in antibody diluent	1h RT
Tris wash buffer (pH6)	10 min
100 µl DAB solution (1:50)	10 min RT
Tris wash buffer (pH6)	10 min
Hematoxylin	20 sec
Water bath (37°C)	1 min
Deionized water	Short wash

Table 24: IHC staining protocols for Gfap

Reagent	Incubation
1x Target Retrieval solution, citrate pH 6.1	30 min 330W, allow cooling
Dionized water	3x, incubate overnight at 4°C
Tris wash buffer (pH6)	10 min
100µl 3% peroxidase solution	10 min
Tris wash buffer (pH6)	10 min
100µl antibody diluent	20 min
100µl antibody in antibody diluent	1h RT
Tris wash buffer (pH6)	10 min
100 µl biotinylated secondary antibody (Reagent AB2)	15 min RT

Tris wash buffer (pH6)	10 min
100 µl streptavidin alkaline phosphatase (Reagent AP)	15 min RT
Tris wash buffer (pH6)	10 min
100 µl chromogen solution (Chromogens Red 1+2+3 (1:25) in AP substrate buffer)	1.5 min RT
Tris wash buffer (pH6)	10 min
Hematoxylin	20 sec
Water bath (37°C)	1 min
Deionized water	Short wash

2.2.8. Microscopy

2.2.8.1. Bright field microscopy

Bright-field microscopy enabled cell morphology study of tumor cells and tumor cell spheroids. Visualizations were carried out with a FV3000 confocal laser scanning microscope (Olympus) and analyzed with the FV31S-SW image processing software. 20x (oil-free), 40x and 60x (oil immersion) objectives were used to acquire images. The EVOS FL microscope was also used to monitor spheroid formation or cell confluence levels at 4x and 10x magnification.

2.2.8.2. Confocal microscopy

Immunofluorescence stainings of tumor cells and tumor cell spheroids were visualized with a FV3000 confocal laser scanning microscope (Olympus) and analyzed with the FV31S-SW image processing software. DAPI (405 nm), FITC (488 nm) and TRITC (532 nm) lasers were used to acquire images with a 20x (oil-free), 40x and 60x (oil immersion) objectives, avoiding fluorescence crosstalk between channels by applying sequential acquisition.

2.2.9. Statistical analysis

All experiments were performed at least in biological triplicates unless stated otherwise. Statistical analysis was performed with GraphPad Prism 7 software and data sets were analyzed with unpaired *t*-test (one variable, two groups), one-way analysis of variance (ANOVA) (one variable, three or more groups), or two-way ANOVA with or without repeated measurements (two variables, two or more groups) depending on the experimental design. ANOVAs were followed by appropriate post-hoc tests including Dunnett's

(comparing every mean to a control mean), Tukey's (comparing every mean with every other mean) or Sidak's (comparing selected pairs of means) multiple comparisons. For Kaplan-Meier survival analysis, a log-rank test was performed. For contingency tables, a chi-square test was used. Data are displayed as mean + standard deviation (SD) unless stated otherwise. *P* values less than 0.05 were considered as being statistically significant (**P* < 0.05; ***P* < 0.01; ****P* < 0.001; *****P* < 0.0001). Final graphics were generated with GraphPad Prism 7 software.

3. Results

3.1. Murine breast cancer cell lines

Breast cancer is the second most common primary tumor with a propensity to BM overall and the most prevalent in women worldwide. As previously explained in this thesis, the molecular subtype of breast cancer has a great impact on the incidence, prognosis, and treatment response of breast cancer-derived BM (Kim et al., 2018; Kotecki et al., 2018). Patients characterized with the HER2+ or the TN subtypes account for the most aggressive forms of breast cancer and experience a higher risk of developing BMs (Rostami et al., 2016). Accordingly, the 4T1 and 410.4 murine breast cancer cell lines were used in this work as TN breast cancer models, while the TUBO murine breast cancer cell line was used as HER2+ molecular subtype of breast cancer.

3.1.1. Characterization of murine breast cancer cell lines

First, we looked for differences between the selected breast cancer cell lines *in vitro*. For this, we determined their proliferation rates and investigated their different pathophysiology. The expression of epithelial-like markers, such as E-cadherin (Ecad), cytokeratin 8 (Ck8) and β -catenin (β Cat) and the mesenchymal-like marker vimentin (Vim) were assessed. Next, the cell lines were characterized morphologically by immunofluorescence in 2D and 3D cell culture models.

Cell line-specific differences concerning cell proliferation rate were found, with the TUBO cell line showing the lowest proliferation ratio, the 410.4 cell line performing intermediate proliferation speeds and the 4T1 cell line with the highest proliferation index (Figure 8A). According to protein expression analysis, the TUBO cell line expressed E-cadherin strongly compared to the 410.4 and, to a greater extent, the 4T1 cell line. The same was observed for Ck8 and β Cat epithelial markers, albeit with a less marked gradation between cell lines. Contrary, the 4T1 cell line showed high protein levels of Vim compared to 410.4 and TUBO, in which levels of the mesenchymal marker were undetectable by western blot analysis (Figure 8B).

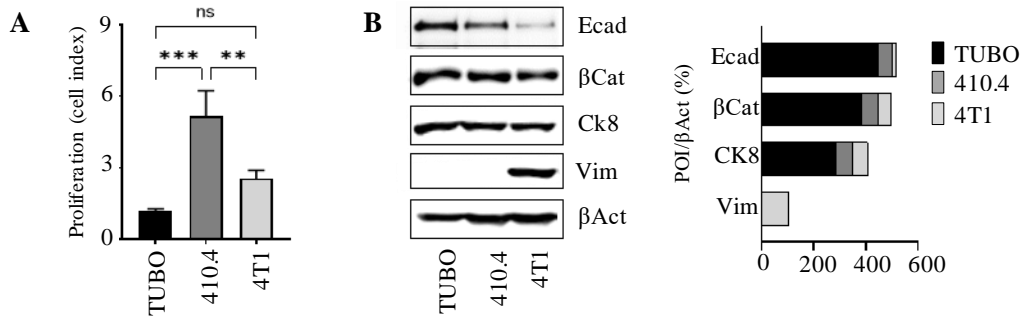


Figure 8. Characterization of murine breast cancer cell lines. A) Cell proliferation rate of TUBO, 410.4 and 4T1 cell lines after 48h. **B)** Western Blot analysis of epithelial (Ecad, β Cat, Ck8) and mesenchymal-like (Vim) markers. Quantification of representative bands for E-cadherin (Ecad), β -Catenin (β Cat), Cytokeratin-8 (Ck8), Vimentin (Vim) and β -Actin (β Act) protein expression is shown. P-value was calculated with one-way ANOVA followed by Tukey's multiple comparisons; ** $P < 0.01$, *** $P < 0.001$.

Morphologically, all three cell lines were adherent and grow with different degrees of tightness. While TUBO cells grew as rather round and tightly packed structures, 410.4 cells grew as wide, tight surfaces and 4T1 cells showed looser structures with fewer attachment points (Figure 9A). Reinforcing protein expression analysis, the three breast cancer cell lines displayed an epithelial phenotype *in vitro*, albeit with a progressive gradation in their E-cadherin expression. According to immunofluorescence staining, TUBO showed a marked epithelial phenotype compared to 410.4 and 4T1, while the expression level of E-cadherin in 4T1 was notably reduced. The decrease of Ecad expression in 4T1 was concomitant with an increase of vimentin expression, pointing to a partially mesenchymal character of the cell line, absent in 410.4 or TUBO (Figure 9B).

Additionally, the formation of spherically symmetric aggregates of cancer cells with no artificial substrate for cell attachment by the hanging drop assay (see Methods 2.2.2.1) allowed us to work with 3D cell culture models. All three epithelial cell lines were able to form spheroids. However, as noted in the 2D models, the resulting tumor spheroids showed quite dissimilar structures with contrasting degrees of compactness. Interestingly, analogous to what happens during metastasis, the cells at the periphery of each spheroid were actively proliferating, while the inner region of the spheroid (spheroid core) remained as a quiescent necrotic zone. Confocal images of E-cadherin staining (green) showed the epithelial marker mainly localized at the periphery of the spheroids, more strongly expressed in TUBO and weaker in 4T1. Likewise, 4T1 showed intense positive staining for vimentin (red), whereas TUBO and 410.4 cells showed very mild and almost absent signs of positive staining (Figure 9C).

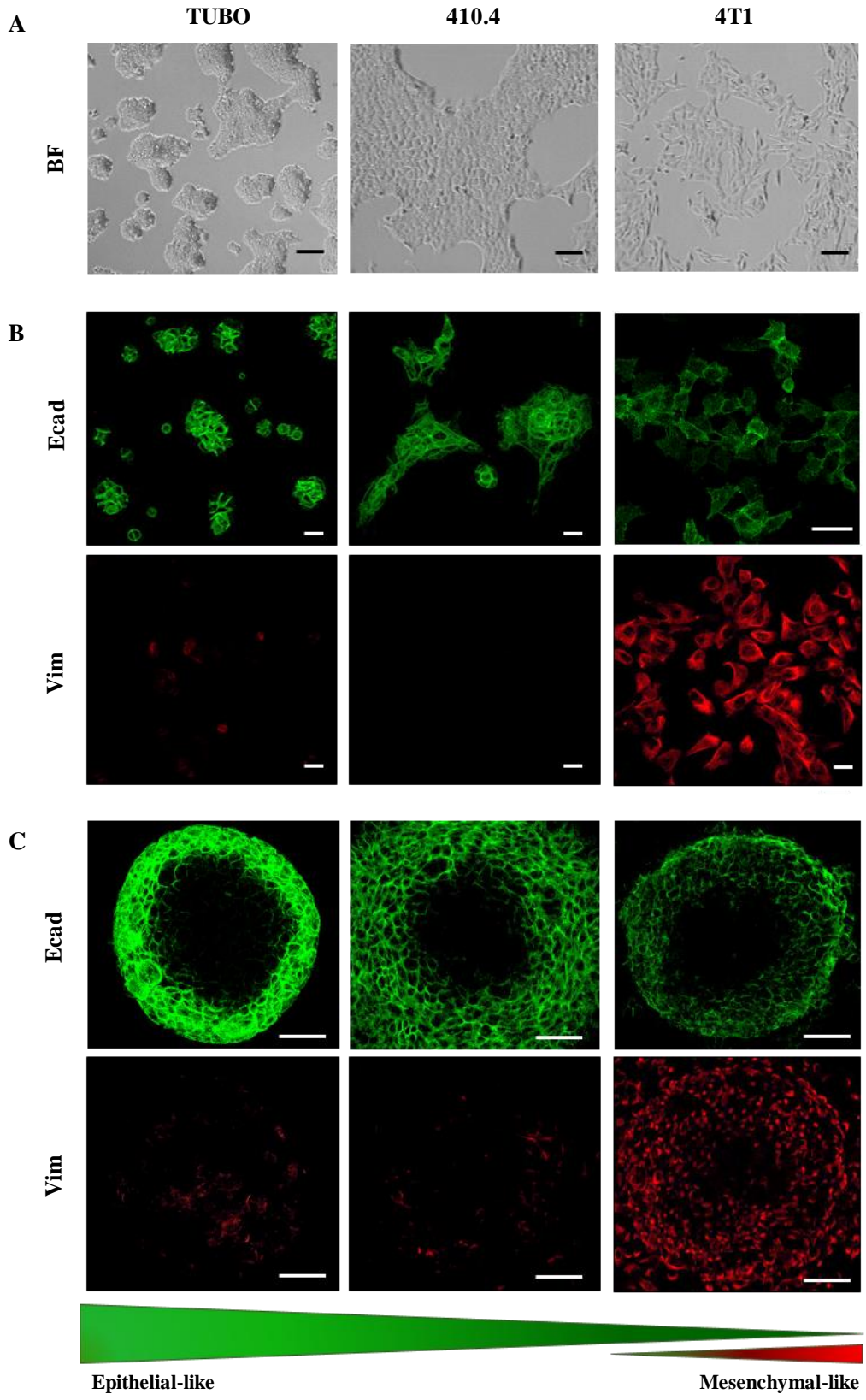


Figure 9. Morphological characterization of murine breast cancer cell lines. **A)** Representative pictures of murine breast cancer cell lines (TUBO, 410.4, 4T1) were taken with a bright field (BF) microscope. Scale bars represent 100 μm (black lines). **B)** Confocal microscopy images after Ecad-conjugated FITC (green) and Vim-conjugated TRITC (red) staining of 2D cell culture models of breast cancer cell lines. Scale bars represent 50 μm (white lines). **C)** Detailed representative images of E-cadherin and Vimentin-stained tumor cell 3D spheroids. Scale bars represent 40 μm . Black areas within the spheroids represent necrotic zones.

Collectively, all three murine breast cancer cell lines were identified as epithelial, although marked differences in their epithelial/mesenchymal-like (E/M) cellular state was observed. While TUBO and 410.4 cell lines showed hardcore Ecad expression, the 4T1 expressed both Ecad and Vimentin, indicating a more mesenchymal-like status of these cell line compared to 410.4 and TUBO.

3.2. Brain metastasis mouse models

A crucial aspect of this work involves investigating the impact of IL4 signaling in BCBM models displaying different MMPI patterns. The 4T1 and its parental 410.4 TN breast cancer cell lines have been successfully established as syngeneic BM models in our group and respectively described as high and moderate colonizers of the CNS (Blazquez et al., 2020A). Both cell lines show infiltrative growth at the MMPI. We hypothesized that infiltrative growth patterns must be associated with an increased immune infiltration compared to displacing growth patterns. To assess this question one very important aim of this thesis was the establishment of a displacing model. For this, we used the TUBO, a HER2-driven cell line (Rovero S. et al., 2000) kindly provided by Prof. C. Klein within the FOR2127 project.

3.2.1. TUBO breast cancer brain metastasis mouse model

The establishment of the TUBO as a mouse model of murine BCBM was initially approached by stereotactically injecting different amounts of cells (10^4 and 10^3) embedded in ECM into the right hemisphere of 10-12 weeks old syngeneic Balb/C mice, as previously described (Blazquez et al., 2020) (Figure 10A). The stereotactic injection of 10^4 cells resulted in median overall survival (OS) of 17 days, while the injection of 10^3 cells led to a median overall survival (OS) of 20 days in all mice (Figure 10B). The presence of macro-metastasis in the injected brains was confirmed by immunohistochemistry (IHC) analysis. The use of epithelial markers such as Ck8, widely used in the pathological diagnosis of adenocarcinoma, revealed the exact location of metastatic brain tissue (Figure 10C). Of interest, since the

injection of both quantities of TUBO cells led to the successful colonization of the brain, I decided to use the lowest amount of tumor cells able to induce metastatic growth in more than 90% of the mice for further analysis.

The metastatic-load marker Ck8 was further assessed in the brain tissue by qRT-PCR analyses. The expression level of *Ck8* was significantly increased in TUBO-injected mice in comparison with control mice, only injected with ECM, robustly confirming the detection of BM (Figure 10D).

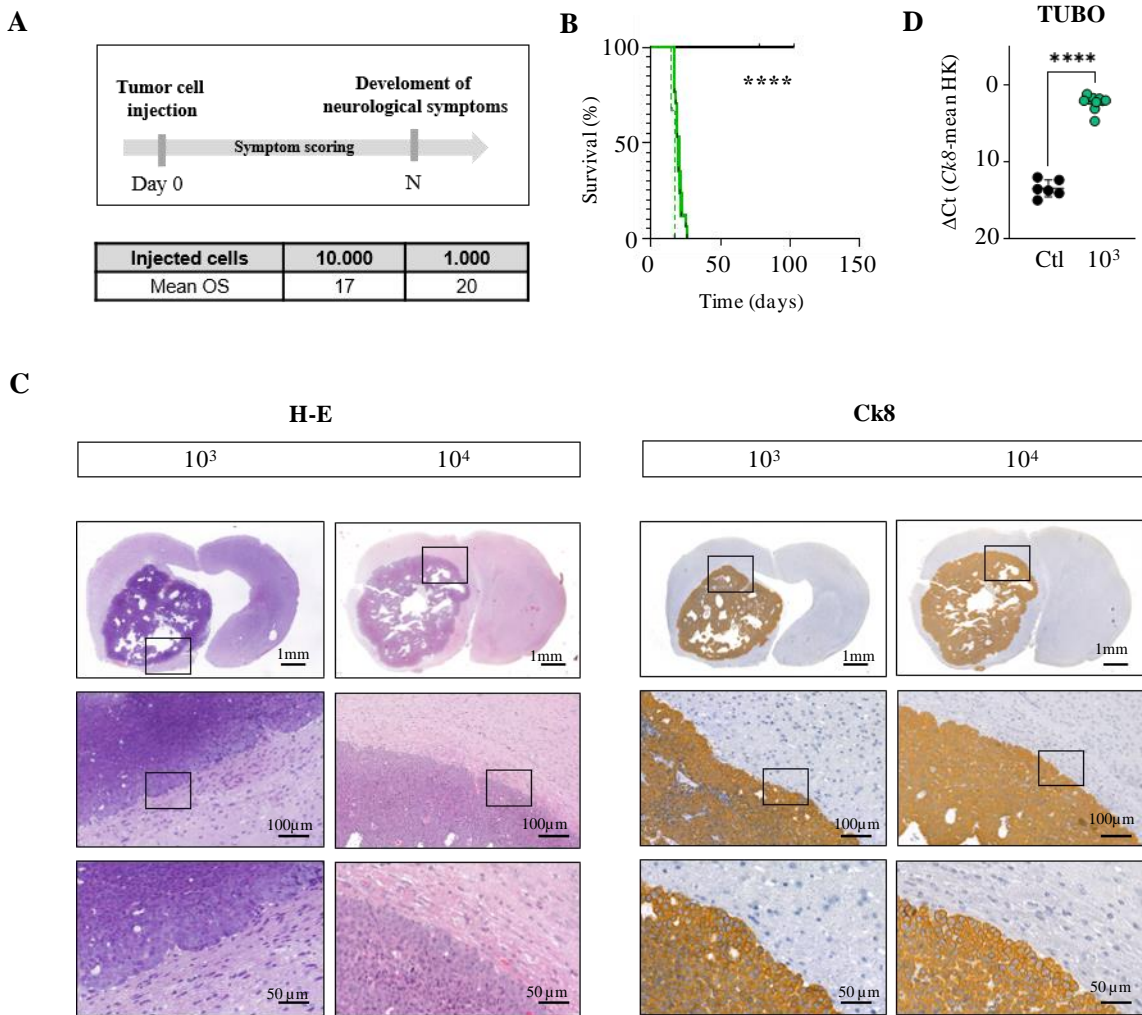


Figure 10. TUBO breast cancer BM mouse model. **A)** Scheme of the *in vivo* experimental setting. **B)** Kaplan-Meier curve reveals overall survival (OS) of syngeneic mice injected with 10³ (solid green) or 10⁴ (dotted green) TUBO cells. P-value was calculated with Log-rank (Mantel-Cox) test (p<0.001). **C)** IHC staining of cytokeratin 8 (Ck8) in tissue sections of TUBO-induced brain metastases after injection of 10³ and 10⁴ cells. Representative images of coronal brain sections and images of the MMPI at higher magnifications are shown. **D)** Real-time PCR analysis of *Ck8* gene expression in ECM-injected controls

(Ctl, black) and TUBO metastatic tissue (green). *Gapdh* and *Pgk1* were used as housekeeping (HK) genes. P-value was calculated with the unpaired t-test (****p <0.001).

Altogether, the TUBO cell line has been established as a mouse model of murine BCBM. This TUBO-mediated colonization model results in lethality within 2-3 weeks after injection *in vivo* and displays a displacing MMPI pattern.

3.2.2. Comparison of breast cancer brain metastasis mouse models

The establishment and characterization of TUBO breast cancer cell line BM mouse model were followed by comparison with the previously described 4T1 and 410.4 models. The three models were analyzed in terms of their overall survival on previous findings (Blazquez et al., 2020A), injection of only 10^3 cells was sufficient to cause the formation of symptomatic metastases in both cases.

3.2.2.1. Overall survival and colonization index

As reported in the previous section, injection of TUBO led to metastatic symptom development and subsequent fatality within 2-3 weeks after injection (median OS = 20 days). In turn, stereotactical injection of the moderate colonizing 410.4 cell line in syngeneic mice caused a delayed death, approximately 7-8 weeks (median OS = 51 days) after injection. Mice injected with the highly aggressive 4T1 developed metastases approximately 3-4 weeks after intracortical injection (median OS = 25 days), with shortened survival rates closely resembling those described for TUBO (Figure 11A).

To accurately compare the colonization capacity of these cell lines, their colonization potential was assessed using a simple and precise quantification tool developed in our group: the colonization index (CI) (Trigueros et al., 2022, submitted). The CI allows to easily determine the aggressiveness of a cancer cell line in means of its colonization capacity by considering three important parameters: the number of carcinoma cells injected, the percentage of animals developing symptomatic brain metastases and the median overall survival of the mice. Thus, the colonization potential of TUBO as BCBM mouse model was assessed by formulation of the CI and compared to 4T1 and 410.4 BM models. Surprisingly, TUBO emerged as a highly colonizing cell line (CI=0.5) (Figure 11B). As expected from previous publications, the 4T1 cell line was found to be a high colonizer (CI=0.4), while the 410.4 cell line showed a moderate colonizing potential (CI=0.196) (Figure 11B).

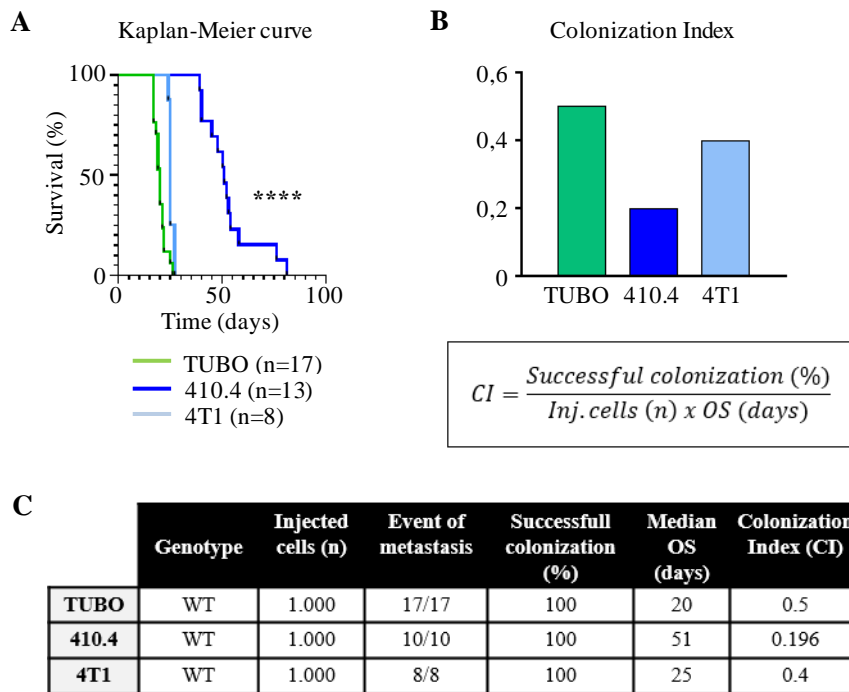


Figure 11. Overall survival and colonization index of BCBM mouse models. **A)** Kaplan-Meier curve shows overall survival of syngeneic mice injected with TUBO, 410.4 or 4T1 breast cancer cell lines. 10^3 cells were injected in all cases. P-value was calculated with Log-rank (Mantel-Cox) test (**** $p < 0.0001$). **B)** Colonization index (CI) comparison among TUBO, 410.4 and 4T1 breast cancer cell lines. The mathematical equation is depicted. **C)** Representation of parameters considered in order to evaluate the CI.

Collectively, the TUBO brain metastasis model resulted in the worst survival rate and the highest CI, closely followed by the 4T1 model in both cases. The 410.4 model had a better prognosis, although equally fatal, and a more moderate CI.

3.2.2.2. Tumor load analyses by qRT-PCR

Brain tissue of the mice stereotactically injected with TUBO, 410.4 and 4T1 did not show any significant differences regarding their tumor load, as could be confirmed using quantitative real-time PCR analyses of the metastatic-load marker Ck8. Additional cytokeratin markers including cytokeratin 19 (Ck19) and the epithelial marker Ecad, both associated with metastatic development, were also analyzed. TUBO-derived metastatic brain tissues revealed significantly increased expression levels of *Ck19* and *Ecad* in comparison

to 410.4 and 4T1-injected brains, pointing to the previous *in vitro* reported grading of epithelial features of the BM model cell lines. Likewise, expression levels of the mesenchymal marker vimentin were significantly increased in 4T1 metastatic brains in comparison to 410.4- and, to a greater extent, to TUBO-metastatic brain tissues, confirming previously reported *in vitro* mesenchymal status of the 4T1 cell line (Figure 12).

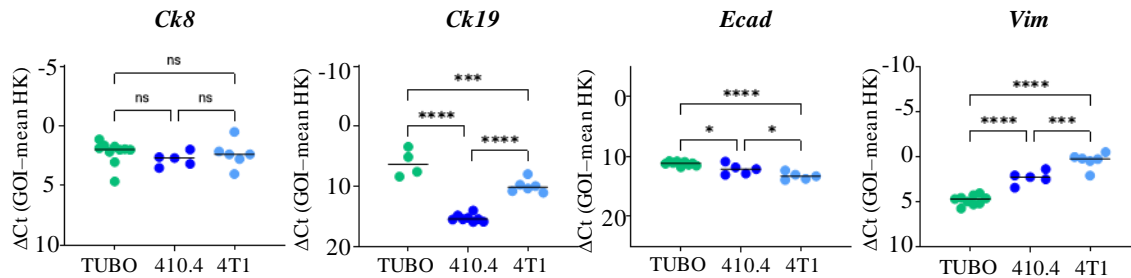


Figure 12. Tumor load comparison between the BCBM mouse models. A) Real-time PCR analysis of the metastatic epithelial markers including cytokeratin 8 (Ck8), cytokeratin 19 (Ck19) and E-cadherin (Ecad), and the mesenchymal marker vimentin (Vim). Expression levels were assessed in BM from TUBO-, 410.4- and 4T1- stereotactically injected mice. *Gapdh* and *Pgk1* were used as housekeeping genes (HK; mean and individual values; $n \geq 4$; one-way ANOVA followed by Tukey's multiple comparisons; * $P < 0.05$, *** $P < 0.001$, **** $P < 0.0001$, ns=not significant).

3.2.2.3. Macro-metastasis / organ-parenchyma interface (MMPI)

As previously explained in this work, recent publications highlight the prognostic impact of the growth pattern of metastases at the MMPI, which correlates with overall survival of patients in BM (Siam et al., 2015). Two types of MMPI can be distinguished: infiltrating and non-infiltrating MMPI, which account for 60 and 40% of BM, respectively (Blazquez et al., 2020B).

Comparative IHC analysis of the metastatic brains obtained from injection with the murine BM model cell lines revealed the existence of major disparities in their MMPIs. General hematoxylin/eosin (H-E) and specific Ck8 staining of the brain metastatic areas revealed wide metastasis with a solid growth pattern in TUBO-injected mice. No signs of infiltration into the adjacent parenchyma at the MMPI could be observed. Instead, defined margins pushing surrounding areas in order to grow by compression of the adjacent tissue were found. This type of metastatic growth pattern has been previously described by our group as a non-infiltrative or displacing MMPI pattern (Blazquez et al., 2020B). However, the brain macro-metastases arising from the TUBO murine breast cancer cell line may represent the first *in vivo* model system to study

the non-infiltrative displacing MMPI pattern, to the best of our knowledge. Mice stereotactically injected with 410.4- and 4T1-cell lines, in turn, displayed an epithelial infiltrative growth pattern at the MMPI (Figure 13).

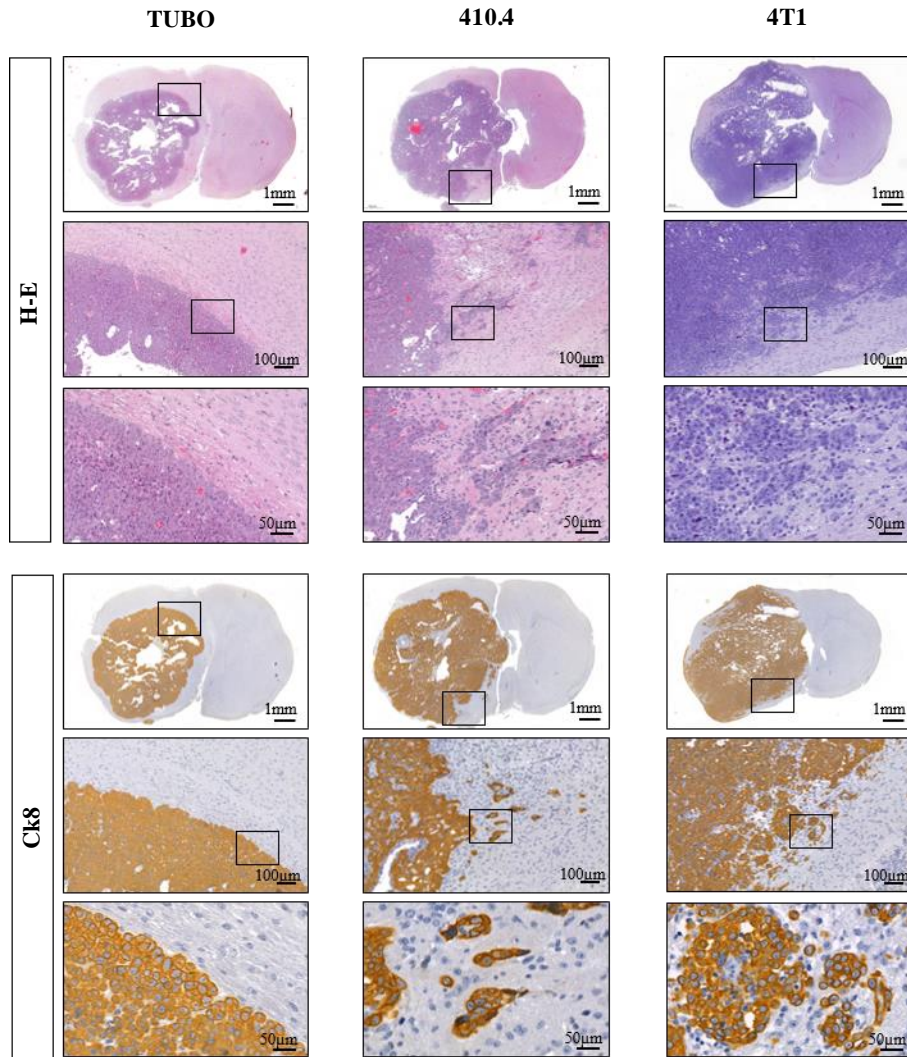


Figure 13. MMPI of BCBM mouse models. Histological staining of hematoxylin/eosin (H-E) and IHC staining of Cytokeratin 8 (Ck8) in tissue sections from brain metastases of Balb/C mice injected with the corresponding cell line. Representative images of coronal brain sections and their MMPI at higher magnifications are shown.

Overall, important morphological differences were found at the MMPI among the three murine BCBM model cell lines included in this study. The TUBO model reflected a characteristic epithelial non-infiltrative growth pattern at the MMPI, albeit with an unexpectedly high CI (median OS=20 days). However, the

moderately colonizing 410.4 (median OS=51 days) and highly colonizing 4T1 (median OS=25 days) models displayed an epithelial infiltrative metastatic growth pattern at the MMPI, as previously described (Blazquez et al., 2020B).

3.2.2.4. The immune microenvironment in BM

The brain-MME comprises a multifaceted immune landscape composed of unique cell types such as astrocytes and microglia that, together with infiltrative peripheral immune cells including infiltrative T cells or MDM, are known to crucially influence metastatic progression in the brain. In turn, MMPIs are considered likely to influence immune infiltration. To investigate how the different epithelial MMPI patterns depicted above are shaping the immune distribution inside (metastatic core), outside (“healthy” tissue) and at the MMPI, I next characterized the presence of activated microglia/macrophages (Iba1+), astrocytic activation (Gfap+) and infiltrative-T cells (Cd3+) in the metastatic brain tissues. Immune markers were analyzed immunohistologically and at RNA level in the metastatic brain tissues.

3.2.2.4.1. Characterization of MG/MDM in the metastatic brain

MG and MDMs are among the major immune cell determinants of the brain-MME landscape (Klemm et al., 2020). While MG are the main resident immune cells in the CNS and the first line of defense in the healthy brain, MDM only crosses the BBB and enters the brain parenchyma after detection of pathogen-derived signals or injury. The dual role of MG/MDMs within the TME is now well known, with complex multifaceted phenotypes that lead to the production of pro- or anti-inflammatory cytokines and other molecules that sculpt the brain-TME. In this context, activated MG/MDM have been associated with neoplastic progression and metastatic spread of tumors, emerging as prominent players in brain cancers and metastasis (Klemm et al., 2020). Since cell type-specific transcriptomic changes have also been reported in MG and MDM comprised in metastatic brain-MME, analysis of the activation states of these two macrophage populations were assessed in all syngeneic BCBM models by using Iba1+.

According to our analysis, activated MG/MDMs were found at the MMPI and core of the metastatic brain in all models. The presence of Iba1-positive cells decreased with increasing distance from the metastatic area and disappeared in the non-injected hemisphere (Figure 14A). Nevertheless, significant differences in MG/MDM frequencies were observed among models. In the case of TUBO-injected brains, no major clusters of activated microglia were observed at the MMPI or metastatic core compared to 410.4 and 4T1-metastatic tissues. The later models, however, showed more Iba1-positive cells, with important MG/MDMs

accumulation at the MMPI, especially for 410.4 and 4T1 (Figure 14A). Analysis of *Iba1* expression by qRT-PCR confirmed macroscopic findings, revealing significant lower levels of *Iba1* in the TUBO model, closely resembling those found in tumor-free ECM-injected mice (control). Tissues injected with 410.4 and 4T1 cells showed a significantly higher macrophage presence, as confirmed by higher *Iba1* expression levels (Figure 14B).

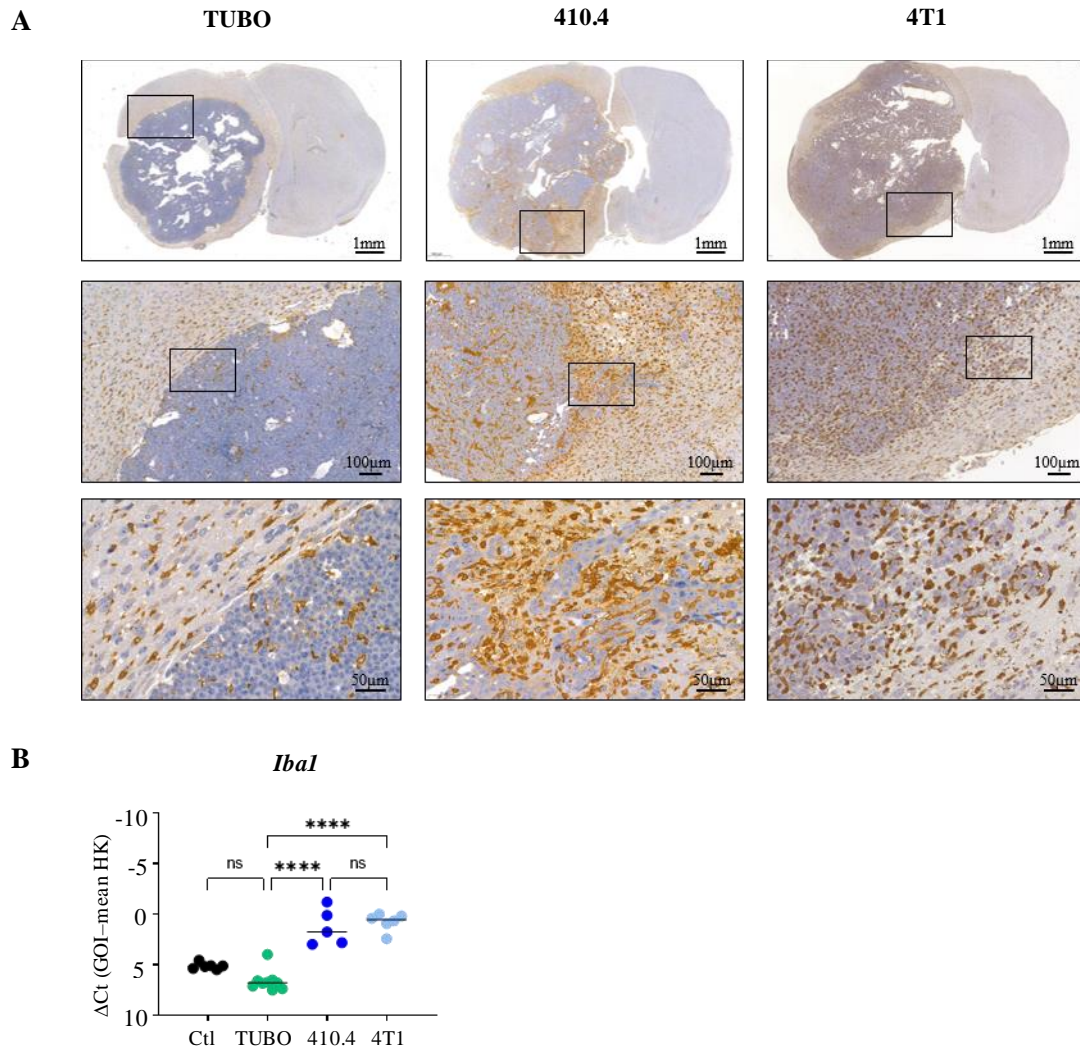


Figure 14. Characterization of MG/MDM populations in the metastatic brain. A) Immunohistochemistry (IHC) images of brain metastatic tissue of mice injected with BCBM models TUBO, 410.4 and 4T1 after staining of MG/MDM populations with *Iba1*. **B)** Real-time PCR analysis of *Iba1* gene expression level in ECM-injected controls (Ctl) and BM from TUBO, 410.4 and 4T1. *Gapdh* and *Pgk1* were used as housekeeping (HK) genes. P-value was calculated with one-way ANOVA followed by Tukey's multiple comparisons tests (**** $p < 0.0001$).

3.2.2.4.2. Characterization of astrocytes in the metastatic brain

Astrocytes, characterized by star-shaped morphology under physiological conditions, are the second glial cell type in the CNS. In response to tumor cells, astrocytes become activated, infiltrating surrounding tissues and capable of triggering metastasis (Xing et al., 2013).

A strong Gfap staining, described as a marker for brain injury (Xing et al., 2013), was observed in all three models. Astrocytes were strongly activated in the brain parenchyma, especially in the hemisphere in which the tumor cells were initially injected. In contrast to microglia, activated astrocytes did not penetrate the metastatic core in any model, but remained in the surroundings. Particularly in TUBO-injected brains, astrocytes seem to arrange themselves at the MMPI to form a sort of glial envelope, surrounding the tumor cells and delimiting the tumor core from the adjacent organ parenchyma (Figure 15A). According to literature (Blazquez et al., 2020B), this reactive glial pseudo-capsule around the metastasis is usually associated with cell lines displaying a non-infiltrative displacing metastatic growth pattern at the MMPI, as in the case of the TUBO model. In turn, in 410.4 and 4T1-injected brains, Gfap-positive cells remained at the periphery of the metastatic core, massively bordering the tumor tissue (Figure 15A).

At the gene expression level, astrocyte numbers were significantly lower in the TUBO model compared to 4T1 and 410.4 metastatic tissues, with *Gfap* expression levels similar to those found in controls. No significant differences in *Gfap* expression levels were found between metastatic brains injected with 410.4 and 4T1 (Figure 15B).

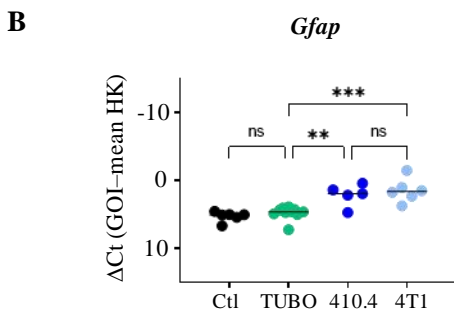
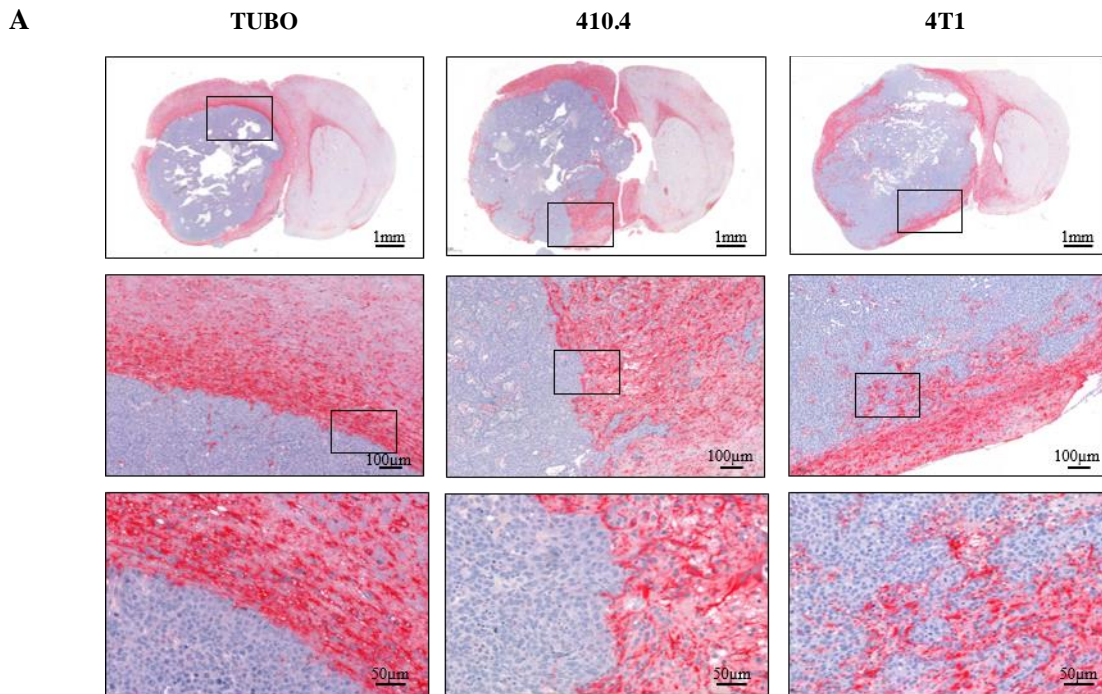


Figure 15. Characterization of astrocyte population in the metastatic brain. **A)** Immunohistochemistry (IHC) images of brain metastatic tissue after staining of astrocyte population with Gfap marker of mice injected with BCBM models TUBO, 4T1 and 410.4. **B)** Real-time PCR analysis of *Gfap* gene expression level in ECM-injected controls (Ctl) and BM from TUBO, 410.4 and 4T1. *Gapdh* and *Pgk1* were used as housekeeping (HK) genes. P-value was calculated with one-way ANOVA followed by Tukey's multiple comparisons tests (** $p < 0.01$, *** $p < 0.001$, ns = not significant).

3.2.2.4.3. Characterization of T cells in the metastatic brain

T cells represent the major immune compartment of BM-MME and correlate positively to brain metastases prognosis. Cytotoxic T cells (CD8+) display a tumor-suppressive function and are associated with

prolonged survival of cancer patients, whereas regulatory T cells (CD4+) also exhibit immunosuppressive properties, related to shortened overall survival rates. Interestingly, T cells infiltrate the CNS only under pathological conditions, so they are mostly absent in healthy brain parenchyma (Berghoff and Preusser, 2015).

Detection of T-cells in the metastatic core, MMPI or organ-parenchyma was assessed by Cd3 marker in the *in vivo* models. Remarkably, TUBO-injected metastatic tissues lacked any trace of T cells immunohistologically. The 410.4 and 4T1-injected brains, in turn, showed positive areas for Cd3 staining both in the metastatic core and at the MMPI, reducing in frequency as the distance from the MMPI increased (Figure 16A). The absence of T cells in the TUBO model was reinforced by qRT-PCR analysis, in which the *Cd3* gene expression was downregulated even compared to tumor-free mice injected with ECM (Ctl). On the other hand, the 410.4 BM model showed a significant increase in T cells compared to 4T1, revealing *Cd3* expression levels considerably higher than those observed in TUBO (Figure 16B).

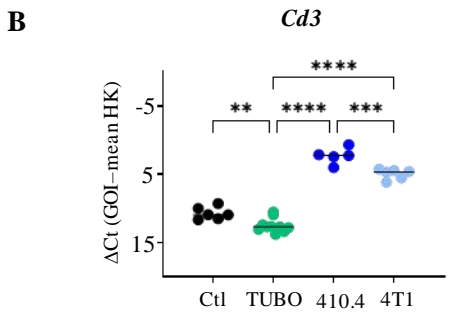
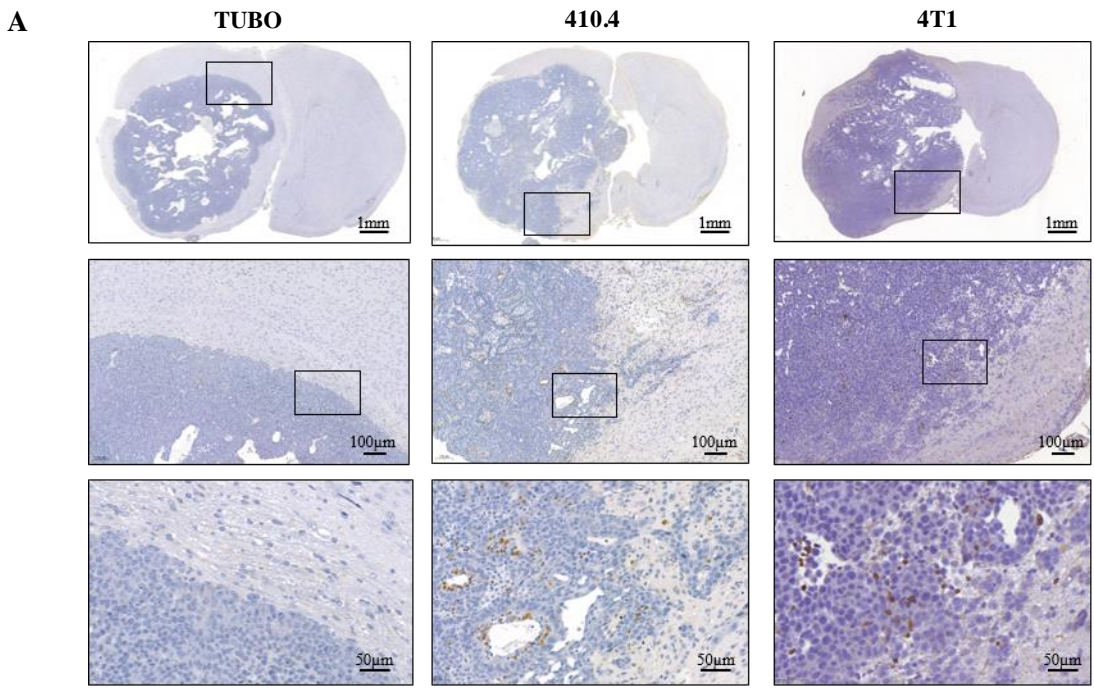


Figure 16. Characterization of T cell population in the metastatic brain. **A)** Immunohistochemistry (IHC) images of brain metastatic tissue after staining of T cell population with Cd3 marker of mice injected with BCBM models TUBO, 410.4 and 4T1. **B)** Real-time PCR analysis of *Cd3* gene expression level in ECM-injected controls (Ctl) and BM from TUBO, 410.4 and 4T1. *Gapdh* and *Pgk1* were used as housekeeping (HK) genes. P-value was calculated with one-way ANOVA followed by Tukey's multiple comparisons tests (**p<0.01, ***p<0.001, ****p<0.0001).

Analysis of the intratumoral immune cell population landscape revealed outstanding differences among BM mouse models. Immune infiltration of all assessed populations was significantly lower in the TUBO model compared to the 4T1 or 410.4 models. Expression levels of *Iba1* and *Gfap* in TUBO metastatic tissues were close to those found in control mice (ECM injected), while no significant differences were observed between 410.4 and 4T1 models. More importantly, *Cd3* expression levels in TUBO metastatic tissues were significantly lower than control levels, suggesting a clear absence of T cells in the metastatic tissue. In contrast, 410.4 metastatic tissues showed higher T-cell infiltration than tissues injected with the 4T1 model, pointing to a potentially decisive differential feature when distinguishing between the two BM models.

Considering the results upon characterization of the immune microenvironment in BM, it could be said that the non-infiltrative TUBO-derived metastasis is immunologically a “cold tumor” model (Liu et al., 2021), with levels of macrophage, astrocyte and mainly T-cell infiltration far below than 410.4 and 4T1 models as well as control-derived tissues. Furthermore, the gene expression profile of TUBO-derived metastatic tissues hardly changes compared to the *in vitro* samples, suggesting a low immune response profile. By contrast, the degree of infiltration of macrophages, astrocytes and T cells in 410.4 and 4T1 is significantly higher than in control tissues both in terms of immune staining and gene expression. Likewise, given the high rate of immune infiltration, T-cell infiltration in particular, the infiltrative 410.4 and 4T1 cell lines are initially considered "hot tumor" models. Brain-MME gene expression shifted significantly in mice injected with these cell lines, suggesting their ability to trigger responses in surrounding cells, including the immune compartment.

3.2.2.5. Cytokine expression profile

For a better understanding of the effects of BCBM mouse models in the *in vivo* brain-MME, the gene expression levels of a panel of different pro- and anti-inflammatory cytokines usually comprised within the MME were measured in metastatic brain tissues (*in vivo*) and compared to the expression levels of the same

genes found in cultured cell lines (*in vitro*) (Figure 17). Except for interleukin-1-beta (*Il1β*), the gene expression pattern of *in vitro* cultured TUBO cell line did not differ significantly from the expression observed in TUBO metastatic brain tissues. Nevertheless, cytokine signaling seemed to be susceptible to modifications in the 4T1 and the 410.4 models. Gene expression levels of arginine-1 (*Arg1*), tumor necrosis factor- alpha (*Tnfα*) or interleukin-4 (*Il4*) were significantly higher in both 4T1- and 410.4-derived metastatic brain tissues compared to the expression levels found in the cultured cell lines. Other markers such as inducible nitric oxide synthase (*iNos*), *Il1β* or interleukin-6 (*Il6*) were regulated only in a single infiltrative model, leaving no explanation to the origin of the shift in the gene expression profile of the immune reactive genes.

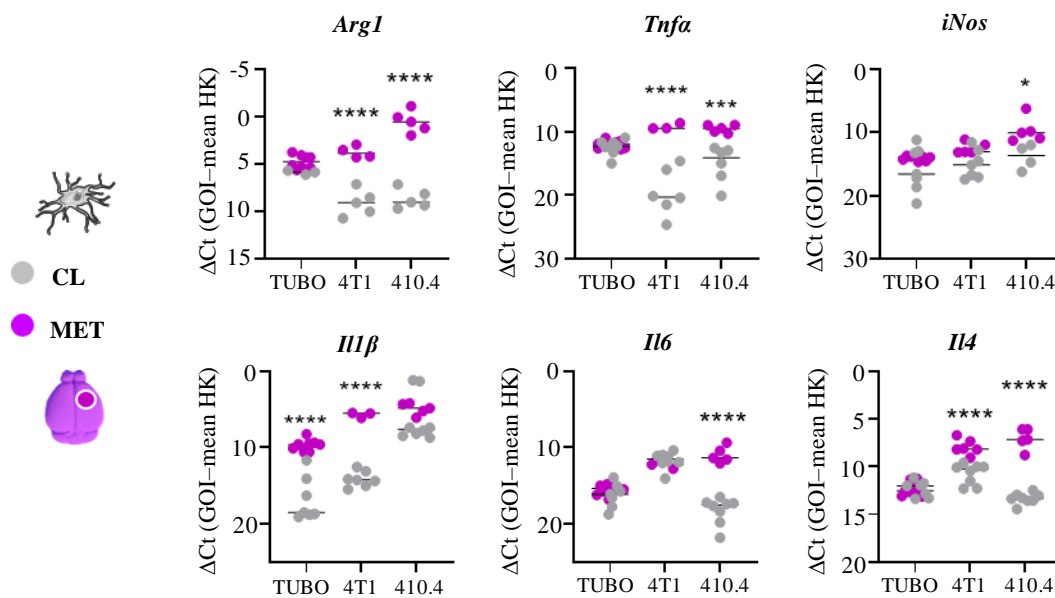


Figure 17. Gene expression signature in the microenvironment of BM: *in vitro* versus *in vivo* expression patterns. A) Real-time PCR analysis of MME-comprised cytokines in metastatic tissue (*in vivo*) compared to gene expression levels in cultured cell lines (*in vitro*). *Gapdh* and *Pgk1* were used as housekeeping (HK) genes. (CL=cell line; MET=metastatic tissue). (Two-way ANOVA; Šídák's multiple comparison test (* $p < 0.05$, *** $p = 0.001$, **** $p < 0.0001$)).

Brain metastatic breast cancer cells are capable to shape the brain-MME to exert tumor-promoting signals that induce pro-tumorigenic processes, although the driving force behind this shift is unclear. Given the limited scope for interaction of the TUBO “immune desert” model with the nearby environment, the drivers of change in the *in vivo* gene expression profile reported in the figure above should rather be reflected in highly interactive tumor models: 410.4 and 4T1. Analyzed genes were higher expressed in the 410.4 – metastatic tissues compared to 4T1 and TUBO models, while TUBO showed the lowest expression rate. Importantly, genes regulated in parallel by both 410.4 and 4T1 models are interrelated: *Arg1* and *Tnfa* are susceptible to regulation upon activation of IL4 signaling. Thus, IL4 emerges as a potential activator of the immune system in the context of brain metastatic environment.

3.2.3. Macrophage migration: “cold” versus “hot” tumor models

As discussed in the introduction, studies of disease-specific enrichment of immune populations point to tissue-resident MG and recruited MDMs have prominent immunosuppressive players in BM (Klemm et al., 2020). However, the complex interplay between metastatic cells and the myeloid compartment is not yet fully understood and therefore requires further research. In our models, the different MMPI patterns (infiltrative vs. displacing) (Figure 14, 15, 16) and the dissimilar cytokine expression profiles (“cold” vs “hot”) (Figure 17), suggest highly divergent degrees of immune infiltration between the three breast cancer models.

In the attempt to shed light on factors governing the macrophage-tumor interactions within the brain-MME in our models, the ability of the murine breast cancer cell lines to induce macrophage migration *in vitro* was assessed by a chemotaxis assay (see Methods 2.2.2.2). In this experiment, monocyte-derived macrophages (MDM) or microglia (MG) migrated through a semi-permeable membrane chemo-attracted by cytokines and chemokines present in the supernatant of the breast cancer tumor cells. Interestingly, widely differing frequencies of macrophage migration were associated with tumor supernatants. Supernatants derived from 410.4 and 4T1 cell lines induced a pronounced MDM migration compared to the control (tumor cytokine-free supernatant), while TUBO-derived supernatant induced a slight but non-significant increase in macrophage migration (Figure 18A). As for MG, 410.4 and 4T1-derived supernatant induced significantly higher migration compared to the control, whereas TUBO-derived supernatant induced no change in migration (Figure 18B).

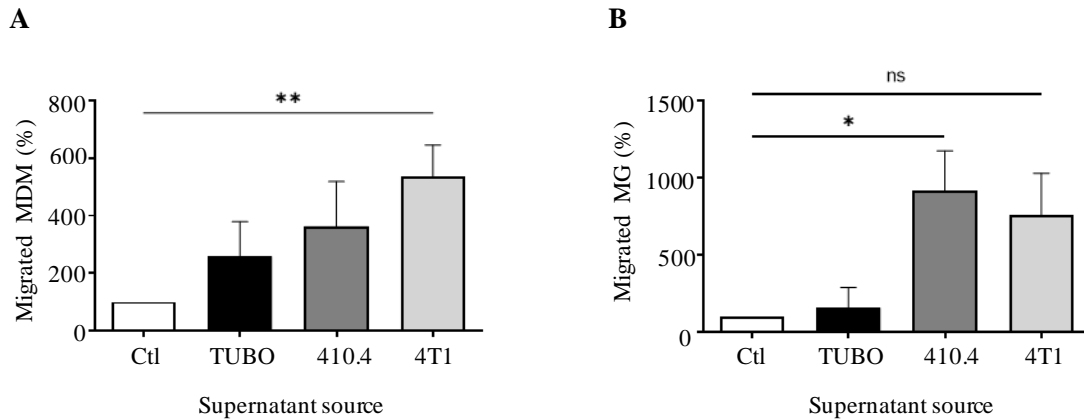


Figure 18. Macrophage migration capacity: “cold” versus “hot” tumor models. **A)** Quantification of MDM migrated cells after co-culture with tumor cytokine supernatant or control supernatant (n=4). **B)** Quantification of MG migrated cells after co-culture with tumor cytokine supernatant or control supernatant (n=2). Control refers to tumor cytokine-free supernatant. The number of migrated cells refers to the cells adhered to the soil of the culture plate after migration. (Ctl, control; P-value was calculated with the unpaired t-test: *p<0.05, **p<0.01, ***p<0.001).

Considering the proposed classification of cancer cell lines as "hot" or "cold" tumors in terms of their degree of immune infiltration *in vivo* (Fig 14, 15, 16), their scope for interaction at gene expression profile level within the brain-MME (Figure 17) and their ability to induce macrophage migration reported above (Figure 18), the TUBO cell line is robustly considered as “cold tumor” model in this thesis, characterized by inducing no or low degree of immune cell infiltration. By contrast, the 410.4 and 4T1 cell lines are taken as "hot tumor" models, triggering a stronger immune response with significant infiltration of immune cells (Liu et al., 2021).

Interestingly, Arg1, iNos, IL6 and IL4 are well established markers for M2-polarized macrophages, while IL1 β and TNF α are well established for M1-polarization. In turn, analysis of the cytokine expression profile in the microenvironment of BM-derived from TUBO, 410.4 or 4T1 suggested IL4, Arg1 and TNF α as essential molecules triggering gene pattern changes of brain-MME *in vivo*. Both Arg1 and TNF α genes, however, are expressed downstream of the activated IL4 signaling pathway. As described in the Introduction of this work (see section 1.4.1), IL4-signaling is among the major downstream effectors of phosphoinositide 3-kinase (PI3K) signaling pathway, a robustly reported driver for metastasis-associated MDM immune-suppressive phenotype (Kaneda et al., 2017). Particularly, IL4 is strongly associated with macrophage-mediated immunosuppression in tumoral and metastatic contexts by regulating its polarization to their anti-inflammatory M2-like phenotype. Yet, the precise involvement of IL4 as an active player in

shaping the brain-MME mediated by breast cancer cells with metastatic capacity is poorly understood. Given the evidence that macrophage polarization to its M2 phenotype is strongly induced by IL4 signaling and its implications for metastatic progression in different organs, we further focus on unraveling the potential role of IL4/IL4R-signaling in the communication between mammary carcinoma cells and the myeloid compartment of BM.

3.3. IL4/IL4R signaling

The hypothesis of this doctoral thesis claims that IL4/IL4R-signaling in microglia/ MDM is crucial for the acquisition of the metastasis-promoting macrophage phenotype during breast cancer colonization of the CNS. To test this hypothesis, IL4 signaling was initially characterized in the different BM mouse model cell lines. Likewise, activation of the IL4 signaling pathway in microglia/MDM was assessed aiming to shed light on IL4-induced metastasis-promoting macrophage phenotype acquisition.

3.3.1. Characterization of IL4 signaling on murine BM model cell lines

Murine BM model cell lines were characterized in terms of protein expression, morphological modifications, and cytokine expression profile upon IL4 signaling activation. First, protein expression of phosphorylated Stat6, a known downstream effector of the IL4/IL4R signaling pathway (Venmar et al., 2014), was assessed upon IL4 treatment. Induction of IL4 signaling cascade activation was confirmed in all three cell lines (Figure 19A). Interestingly, no apparent EMT was observed at the protein level, characterized by a loss of epithelial markers including E-cadherin and β -catenin. These epithelial markers were expressed equally in the control condition (PBS treatment) and after IL4 stimulation of the cell lines (Figure 19B). Morphological characterization featured in detail in confocal images of Phalloidin-conjugated TRITC staining revealed very different patterns of spatial organization, size and degrees of intercellular cohesion among the cells. The absence of IL4-associated EMT induction was further confirmed by morphological analyses, where no evidence of a discernible phenotypic change in the cell body of the tumor cells or signs of EMT induction after IL-4 boosting was observed (Figure 19C).

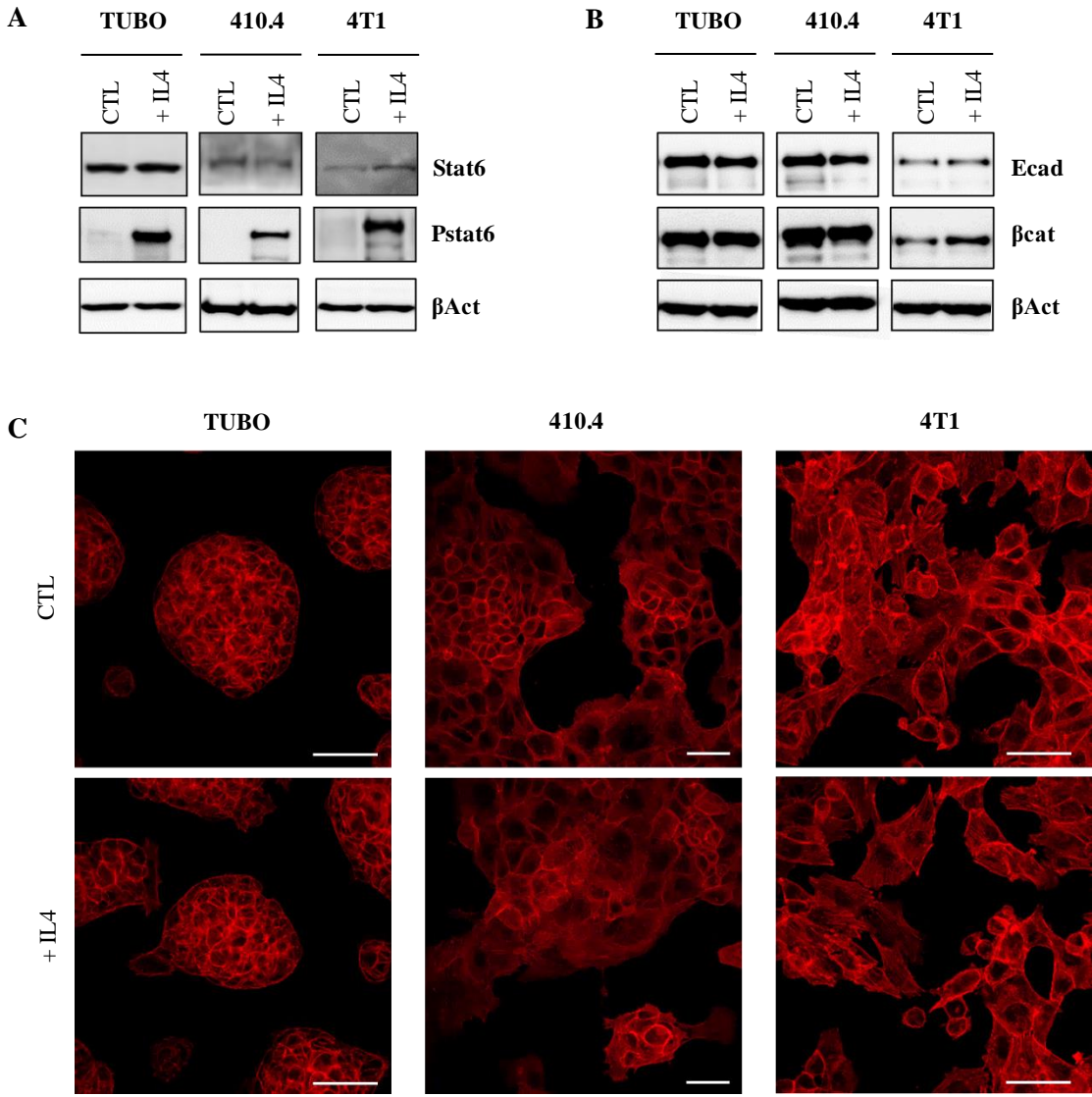


Figure 19. Characterization of IL4 signaling on murine BM model cell lines. **A)** Western blot analysis of IL4 signaling downstream effectors Stat6 and P-Stat6. Representative bands for protein expression are shown upon PBS (control) or IL4 (20ng/ml) treatment. **B)** Western blot analysis of IL4 signaling-downstream effectors Ecad and βcat. Representative bands for protein expression are shown upon PBS (control) or IL4 (20ng/ml) treatment. **C)** Confocal microscopy images after Phalloidin-conjugated TRITC (red) staining. Scale bars represent 40μm.

Next, the gene expression signature of TUBO, 410.4 and 4T1 cell lines upon IL4 stimulation was assessed by quantitative RT-PCR analyses. The classical pro-inflammatory molecule lipopolysaccharide (LPS) was

used as positive control in event of inflammatory response. No changes in the cytokine expression profile were observed upon IL4 or LPS treatment. To consider, all three cell lines showed nearly unchanged expression levels of *Arg1* and *IL4* upon activation of IL4 signaling cascade in comparison to the control group (PBS treated) (Figure 20A).

Furthermore, comparative real-time PCR analysis of inflammatory and anti-inflammatory genes revealed divergent cytokine expression profiles among the cell lines. The highly colonizing TUBO cell line showed a higher expression of the cytokines *Arg1* and *Tnfa* when compared to 4T1, but no significant differences when compared to the moderate colonizing 410.4 cell line. Only expression of *IL1 β* was significantly higher in the 410.4 cell line, with reported lowest expression levels of *Il6*. Lastly, the highly colonizing 4T1 cell line reported significantly higher expression levels of *Il4* and *Il6*, as well as lowest expression levels of *Tnfa*. No significant differences were observed in *iNos* expression among the cell lines (Figure 20B).

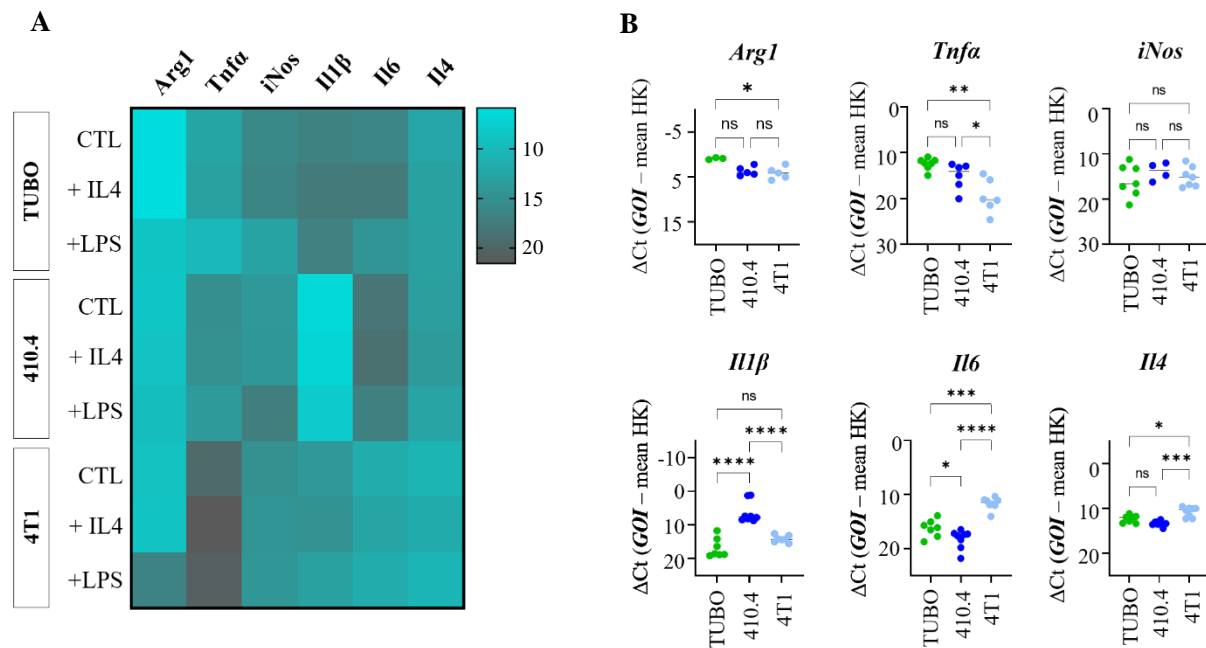


Figure 20. Characterization of IL4 signaling on murine BM model cell lines. **A**) Heatmap representing quantitative RT-PCR analysis of differentially expressed genes (*Il4*, *Tnfa*, *Il1 β* , *Arg1*, *Il6*, *iNos*) in the murine BM cell line model cell lines stimulated with IL4 (20ng/ml) or LPS (10ng/ml) for 24h. **B**) Comparative basal cytokine expression profile among the murine BM model cell lines. *Gapdh* and *Pgk1* were used as house-keeping (HK) genes (n \geq 3; two-way ANOVA; *P < 0.05, **P < 0.01, ***P < 0.001, ****P < 0.0001, n.s. = not significant).

The absence of *in vitro* responsiveness of the murine breast cancer cell lines to IL4 stimulation was confirmed by the absence of IL4-induced EMT, a characteristic feature of the response to the signaling pathway activation according to literature (Cheng et al. 2018). Additionally, bulk gene expression analysis revealed no upregulation of *Arg1* upon IL4 treatment, failing to explain the regulatory changes previously observed in the brain-TME of metastatic tissues (Figure 17). In other words, the breast cancer cell lines themselves are probably not responsible for the gene expression pattern shift observed *in vivo*. It is therefore suggested that the secretion of soluble factors that shape the MME does not necessarily depend on the tumor cell subtype that colonizes it, but rather on alternative cell types, including non-neoplastic cells within it.

3.3.2. Characterization of IL4 signaling on MDM/MG

The study of the disease-specific enrichment of immune populations by Klemm et al. suggests that tissue-resident MG and recruited MDMs are prominent immunosuppressive players in BM (Klemm et al., 2020). Aiming to shed light on the role and underlying mechanism of IL4 in MDM/MG during BM, both myeloid populations were characterized in the presence of IL4, LPS or PBS (control) for 24h concerning basic features such as morphology, protein and gene expression, as in the case of the tumor cells.

Genetically modified mice were used throughout this project to obtain a comprehensive insight into the functioning of IL4. As previously described in this thesis (see Material 2.1.1.3.1), the Cre-lox system technology was used to create a functional homozygous IL4R α -knockout after interbreeding of heterozygous mice (IL4R α ^(+/-)) (Figure 21A). The resulting IL4R α ^(-/-) mice (KO) lack overt phenotypic abnormalities and present normal B and T cell population distribution in lymphatic organs, according to literature (Mohrs et al, 1999; MGI: 2657172). Successful homozygous disruption of the IL4R α gene (IL4R α ^(-/-)) was identified by conventional PCR of biopsies derived from the homozygous intercross offspring (ear punch and freshly isolated MDM) (Figure 21B). The resulting IL4R α -KO BALB/c mice have a pure Balb/C background with a fully competent murine immunity, making this model useful for immunotherapy assessment.

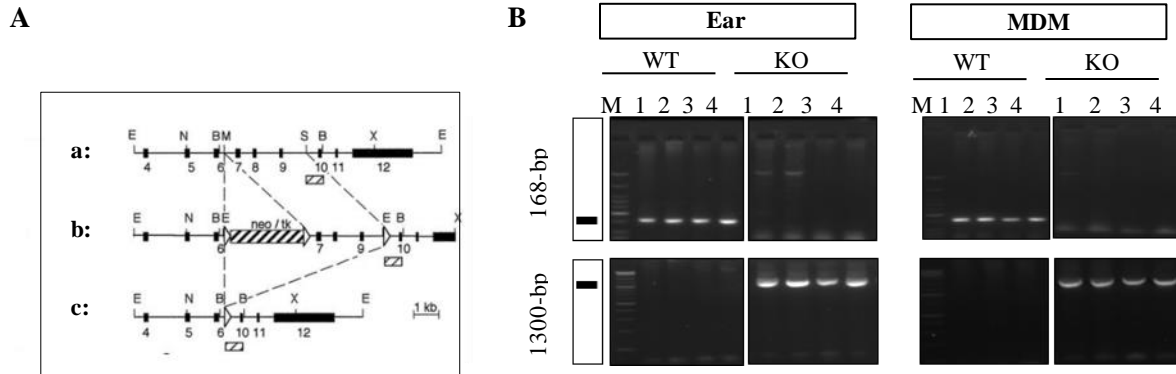


Figure 21. IL4R α -knockout murine model. **A)** Scheme of wild-type IL4R α gene locus (a), the targeting construct (b) and the mutated locus (c). Exons 7 to 9 were deleted by Cre-mediated recombination as described in Mohrs et al.1999. **B)** Conventional PCR analysis of ear biopsies or MDM. The 168-bp bands reveal the wild-type allele (+), and the 1300-bp bands reveal the allele with deleted exons (-) of the knockout mice.

In terms of protein expression analysis, activation of the IL4/IL4R signaling pathway was confirmed in MDM^{WT} and MG^{WT} upon IL-4 stimulation using canonical phosphorylation of Stat6. As expected, no expression of phosphorylated Stat6 was observed in KO macrophages upon IL4 treatment (Figure 22A), suggesting a loss of IL4/IL4R signaling activation that corroborates successful homozygous disruption of the IL4-R α receptor subunit gene. Additionally, IL4 signaling-associated EMT induction of MG/MDM was monitored at protein level by expression of the epithelial markers Ecad and β cat. IL4-dependent expression of Ecad and β cat was observed exclusively in WT cells and absent in the KO cells. No significant increase in the protein expression levels of P-Stat6, E-cadherin or β -catenin was observed in MG/MDM^{WT} or MG/MDM^{KO} after treatment with PBS or LPS (Figure 22A).

In terms of morphological features, MDM^{WT} showed an increased elongation process of the cell body, in some cases generating protrusions up to 120 μ m in length after exposure to IL4. Consistently, these morphological differences reinforce the above pointed expression of E-Cadherin and β -catenin in an IL4-dependent manner, suggesting an EMT induction associated with IL4 signaling activation in MDM^{WT}. No morphological changes were observed in MDM^{KO} or PBS-treated MDM^{WT}, showing instead shortened protrusions of about 70 micrometers (Figure 22C).

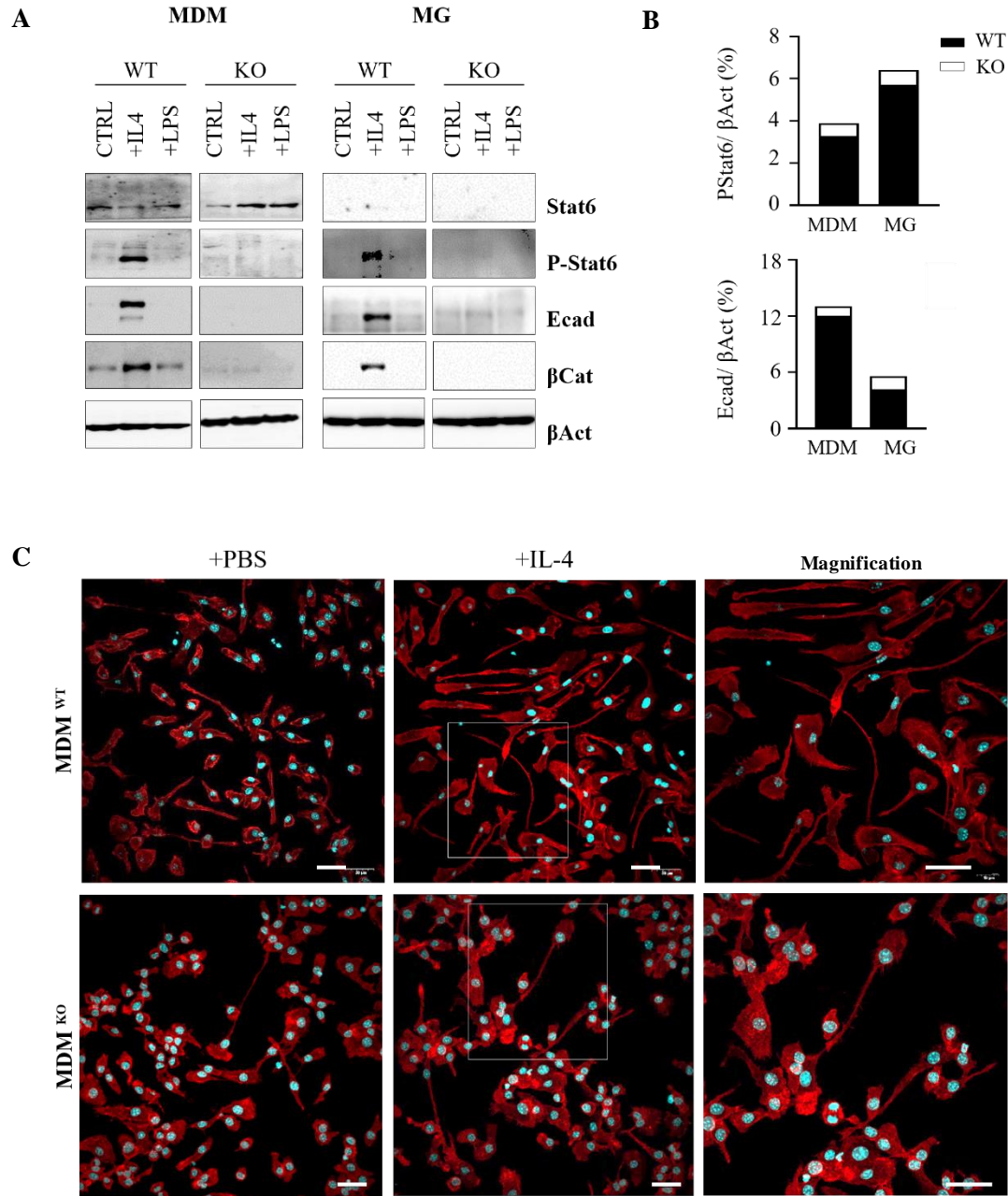


Figure 22. Characterization of IL4 signaling on MDM/MG. **A)** Western blot analysis of IL4/IL4R signaling downstream markers. Representative bands for Stat6, P-Stat6, Ecad and β Cat protein expression are shown upon PBS, IL4 (20ng/ml) or LPS (10ng/ml) treatment. β -actin was used as loading control. **B)** Quantification of E-cadherin and P-Stat6 protein expression. Band intensities were normalized to corresponding loading controls (β -Actin) and displayed as fold change over control cell line. **C)** Morphological features of MDM upon IL4 (20ng/mL) or PBS (ctrl) stimulation. Magnifications of IL4-treated cells are depicted. Confocal microscopy images after Phalloidin-conjugated TRITC (red) staining of cells and nuclear staining with DAPI (blue) are shown. Scale bars represent 30 μ m.

After confirming the successful activation of the IL4 signaling cascade in MDM and MG *in vitro*, M1 and M2 polarization status of MG/MDM was assessed using a panel of marker genes including pro-inflammatory M1-like markers *Il1 β* , *Il6* and *iNos* and immunosuppressive M2-like markers *Arg1*, *Il10* and *Il4*. LPS treatment of both MDM^{WT} and MDM^{KO} induced the upregulation of the traditional pro-inflammatory cytokines. On the other hand, the anti-inflammatory markers *Arg1* and *Il10* were exclusively overexpressed in MDM^{WT} after treatment of the immune cells with IL4. Similar results were seen in MG^{WT}, with *Arg1* overexpression upon IL4 stimulation (Figure 23).

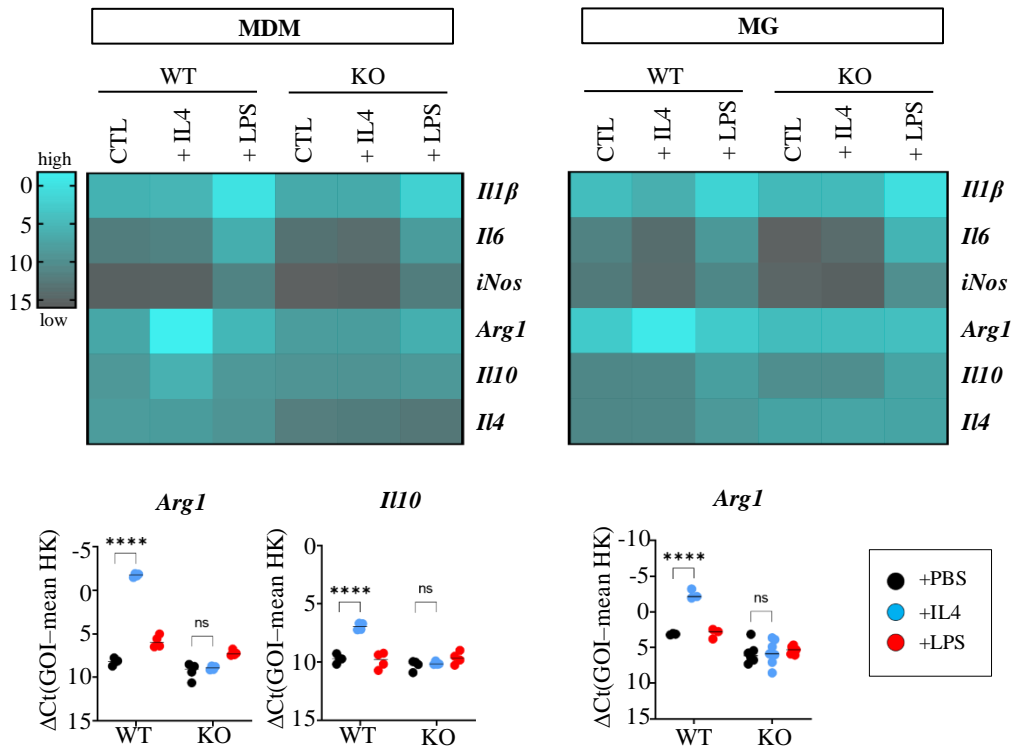


Figure 23. Potential contribution of MDM/MG cytokine profile to the TME. Heatmap of fold changes of macrophage M1 and M2 polarization marker genes in MDM and MG isolated from WT or KO Balb/C mice. Quantitative RT-PCR analysis of M1-like genes (*Il1 β* , *Il6*, *iNos*) and M2-like genes (*Arg1*, *Il10*, *Il4*) (light-coloured refers to high expression). Graphics for the significant differences upon IL4 treatment are shown. Control groups are PBS-treated, IL4 was administrated at 20ng/mL, LPS was administrated at 10ng/mL. Stimulation time: 24h. *Gadph* and *Pgk1* were used as housekeeping (HK) genes (n \geq 3; two-way ANOVA; ****P < 0.0001, ns = not significant).

I next assessed if IL4 treatment was enough to induce alternative M2-polarization of both myeloid populations. As previously reported in the literature, MDM and MG were accurately distinguished in their M2 polarization states by qRT-PCR (Murray et al., 2014; Klemm et al. 2020). The novelty of addressing

macrophage cell identity was assessed by using a panel of marker genes comprising transglutaminase 2 (*Tgm2*), C-C motif chemokine ligand 17 (*Ccl17*), C-X-C motif chemokine ligand 13 (*Cxcl13*), fibronectin-1 (*Fbn1*) and matrix metalloproteinase 12 (*Mmp12*). Analysis of gene expression levels in MDM upon IL4 treatment showed changes in *Tgm2*, *Ccl17*, and *Cxcl13* gene expression levels compared to the control. On the other hand, MG overexpressed the *Fbn1* gene upon IL4 stimulation, while *Mmp12* expression was increased in both cell types (Figure 24).

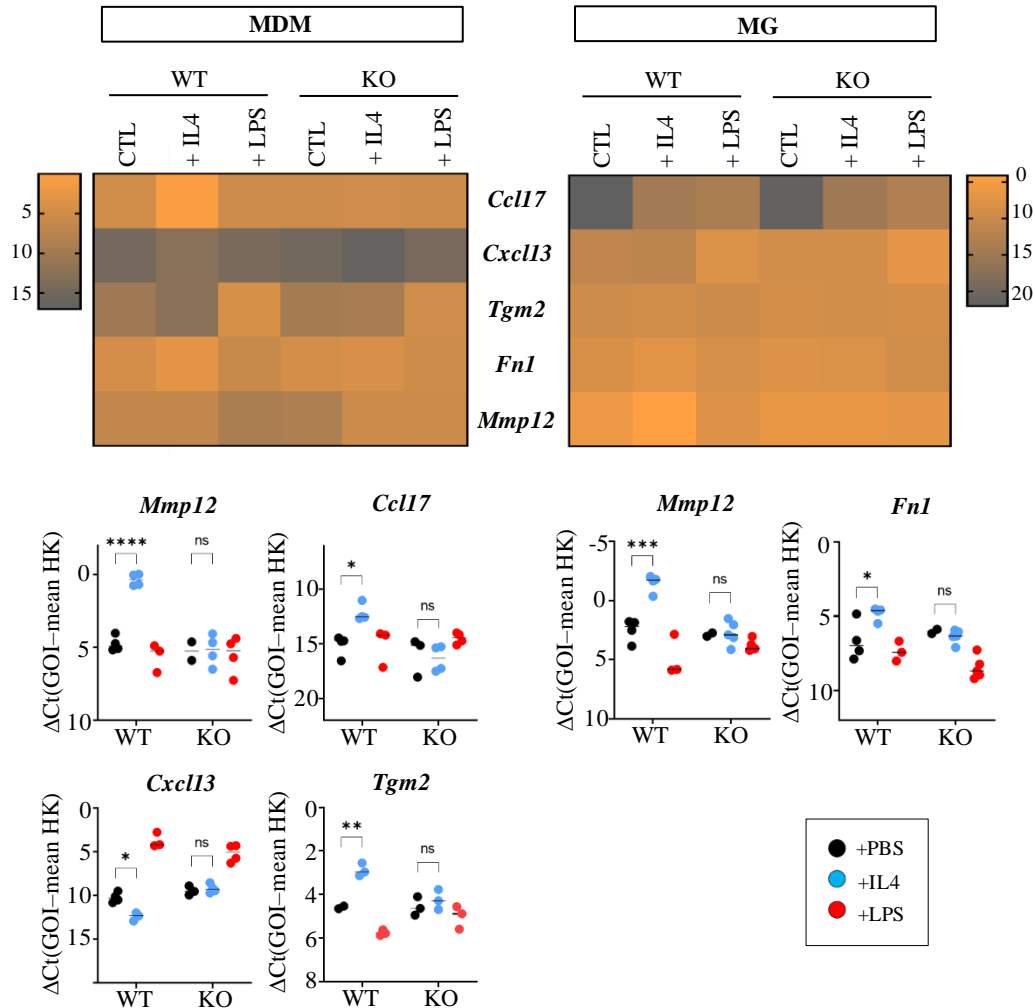


Figure 24. Analysis of M2-polarization status of MDM/MG. Heatmap of fold changes of M2-polarized MDM/MG-specific genes in macrophages isolated from WT or KO Balb/C mice. Graphics for the significant differences in IL4 treatment are shown (light-colored refers to high expression). Control groups are PBS-treated, IL4 was administrated at 20ng/mL, LPS was administrated at 10ng/mL. Stimulation time: 24h. *Gapdh* and *Pgk1* were used as housekeeping (HK) genes (n ≥ 3; two-way ANOVA; *P<0.05, **P<0.01, ***P<0.001, ****P < 0.0001, ns = not significant).

Contrary to the findings in BM mouse model cell lines, overexpression of *Arg1* in MDM^{WT} and MG^{WT} after IL4 stimulation *in vitro* points to potential involvement of both myeloid cell types in the immunosuppression of brain-MME mediated by IL4. These findings strongly suggest that the burden of the previously reported *in vivo* modifications (Figure 17) leading to metastatic development relies greatly on the macrophage component of the brain-MME.

3.3.3. IL4 signaling knockout in BM mouse models

Given the importance of the myeloid compartment in metastatic progression and the ability of MDM/MG to sense and respond to IL4, it became clear the need to determine the effects of macrophage-IL4R signaling during CNS-colonization of syngeneic breast cancer models *in vivo*. According to our hypothesis, the absence of IL4 signaling would prevent the tumor-supporting functions exerted by MDM/MG in their IL-4-induced M2 polarized state, and consequently, a prolongation of overall survival in KO mice compared to WT mice. To test this hypothesis, the BM mouse model cell lines were stereotactically injected in immunocompetent WT and genetically manipulated IL4R α KO mice of the same inbred strain (syngeneic mouse models) as previously published (Blazquez et al., 2020). To this end, a comparative analysis of WT and KO metastatic brains concerning overall survival and CI, tumor load, metastatic growth pattern at the MMPI, immune population infiltration and cytokine expression profile was performed in the next sections.

3.3.3.1. Effects of IL4-signaling knockout in overall survival, CI tumor load and MMPI

Stereotactical injection of 10³ cells into the right hemisphere of WT or IL4R α KO syngeneic mice was performed for all murine breast metastasis model cell lines as described in the Methods section (see 2.2.3.1). In TUBO-injected mice, the appearance of metastasis occurred very early in both WT and KO mice, showing a severe impact on the survival of the animals 2 to 3 weeks after intracortical injection. Interestingly, the absence of IL4 signaling prolonged the survival of KO mice a few days (mean survival WT = 20 days; median survival KO = 24 days), albeit with a slight significance (p=0,121). In mice injected with 410.4, in turn, I found successful colonization of all WT mice (8/8), with a median overall survival of 51 days. Remarkably, and as expected according to our hypothesis, the absence of a functional IL4 receptor in KO mice led to a reduced colonization potential of this cell line (6/18 mice showed macro-metastases) and to a significant increase in the survival of these mice (median OS = 140 days). The median OS of the KO mice that developed BM was 74 days. There were no differences between WT and KO mice injected

with the 4T1 cell line, since both groups developed neurological symptoms at around 3-4 weeks after injection (median OS^{WT} = 25 days; median OS^{KO} =24.5 days), (Figure 25A).

In order to compare the colonization capacity of TUBO, 410.4 and 4T1 BM models in WT and IL4R α KO Balb/C syngeneic mice, the CI was calculated as described previously in this work. As shown in the figure below, the non-infiltrative epithelial displacing TUBO only retained its high colonizing capacity in WT mice, and slightly decreased in the KO mice (CI^{WT}=0.5, CI^{KO}=0.417). The 410.4 model displayed a 4-times less aggressive colonization potential in KO mice compared to WT mice (CI^{WT}=0.196, CI^{KO}=0.056), while the highly aggressive colonization potential of the epithelial infiltrative 4T1 remained unchanged in both WT and KO mice (CI^{WT}=0.4, CI^{KO}=0.4) (Figure 25B).

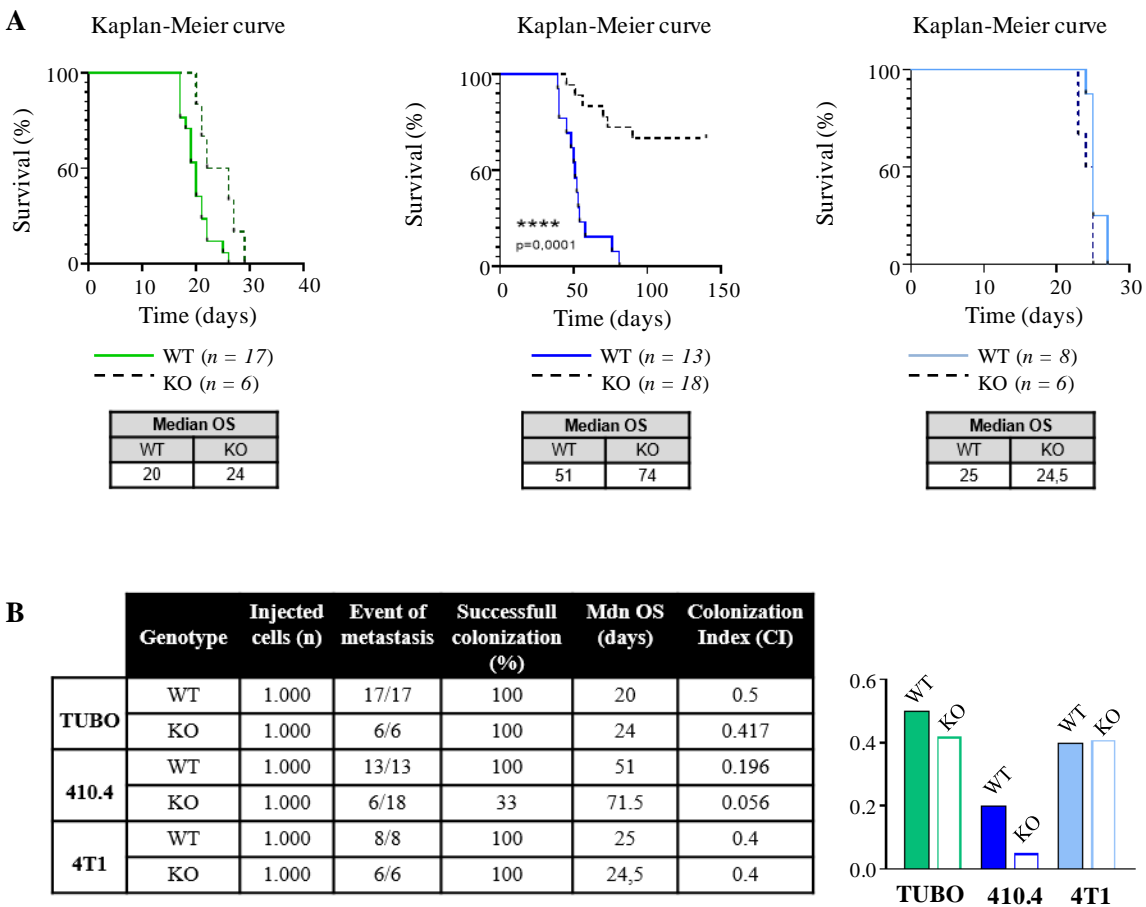


Figure 25. Effects of IL4-signaling knockout in BCBM mouse models on overall survival and colonization index. A) Kaplan-Meier survival curves of IL-4R-WT and IL-4R-KO mice injected with TUBO, 410.4 or 4T1 cell lines. P-value was calculated with Log-rank (Mantel-Cox) test (****p<0.001). B) Effect of IL4R α KO on CI. Comparison among WT and KO mice injected with from TUBO, 410.4 or 4T1 cell lines. Summary table of CI parameters is also shown.

Following determination of the CI of BM models in WT and KO Balb/C syngeneic mice, I next assessed the detection of metastatic evidence by real-time PCR analyses of epithelial markers *Ck8*, *Ck19* and *Ecad*, and the mesenchymal marker *Vim*. Comparison of gene expression between WT and KO mice injected with TUBO revealed no significant differences in *Ck8*, *Ecad* and *Vim*, but a slightly increased *Ck19* expression in the KO mice. Regarding 410.4 and 4T1 models, no significant differences were found in the expression level of epithelial and mesenchymal metastatic markers in KO mice compared to WT mice. As expected, the absence of BM in 410.4-injected tumor-free KO mice correlated with a significantly reduced expression of metastatic markers *Ck8*, *Ck19*, *Ecad* and *Vim* compared to WT and KO tumor-bearing mice (Figure 26).

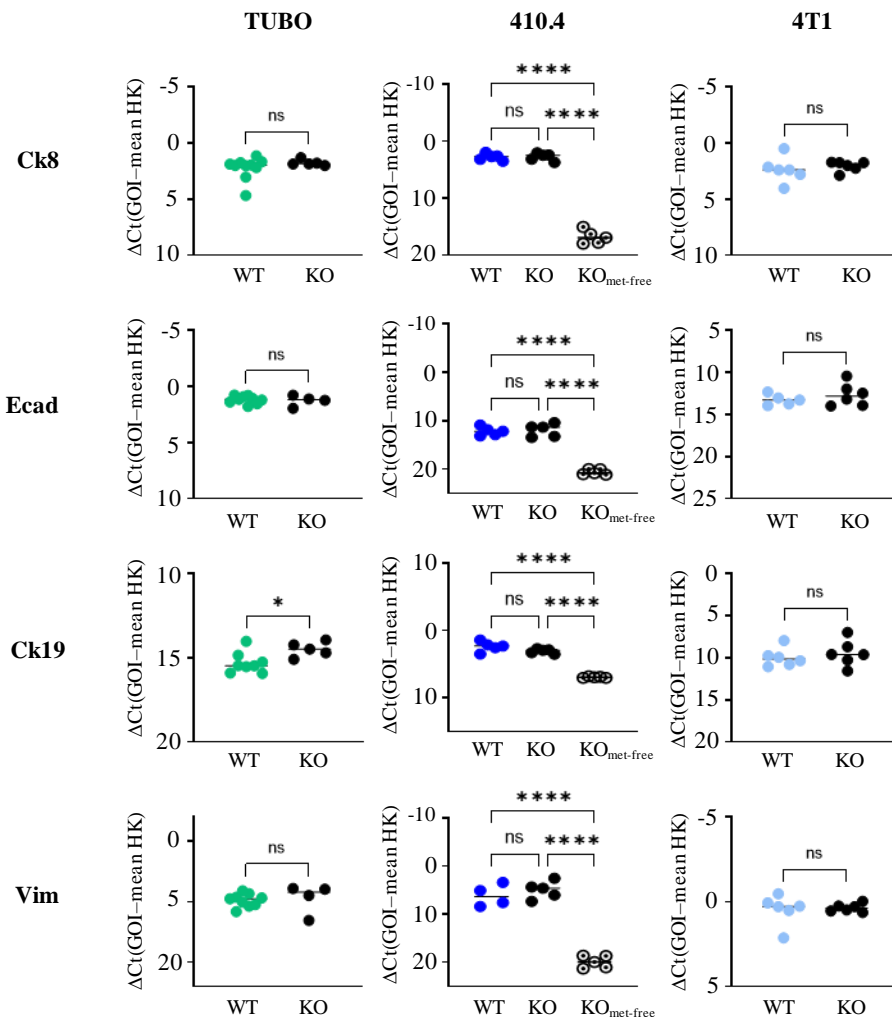


Figure 26. Effects of IL4-signaling knockout in BCBM mouse models on gene expression. Quantitative RT-PCR analysis of cytokeratin 8 (*Ck8*), cytokeratin 19 (*Ck19*), E-cadherin (*Ecad*) and vimentin (*Vim*) gene expression in brain metastases of WT ($IL4R\alpha^{+/+}$) and KO ($IL4R\alpha^{-/-}$) mice. *Gapdh* and *Pgk1* were

used as housekeeping genes (HK; mean and individual values; $n \geq 4$; one-way ANOVA followed by Tukey's multiple comparisons; * $P < 0.05$, **** $P < 0.0001$, n.s. = not significant).

Next, potential alterations in the metastatic growth pattern (MMPI) associated with IL4 signaling blockade were assessed morphologically by IHC analyses. Ck8 staining of TUBO, 410.4 and 4T1-derived metastatic brain areas revealed no changes in the metastatic growth pattern at the MMPI among WT and KO mice in any case. We also confirmed the absence of metastatic growth in the surviving 410.4-injected KO mice (Figure 27).

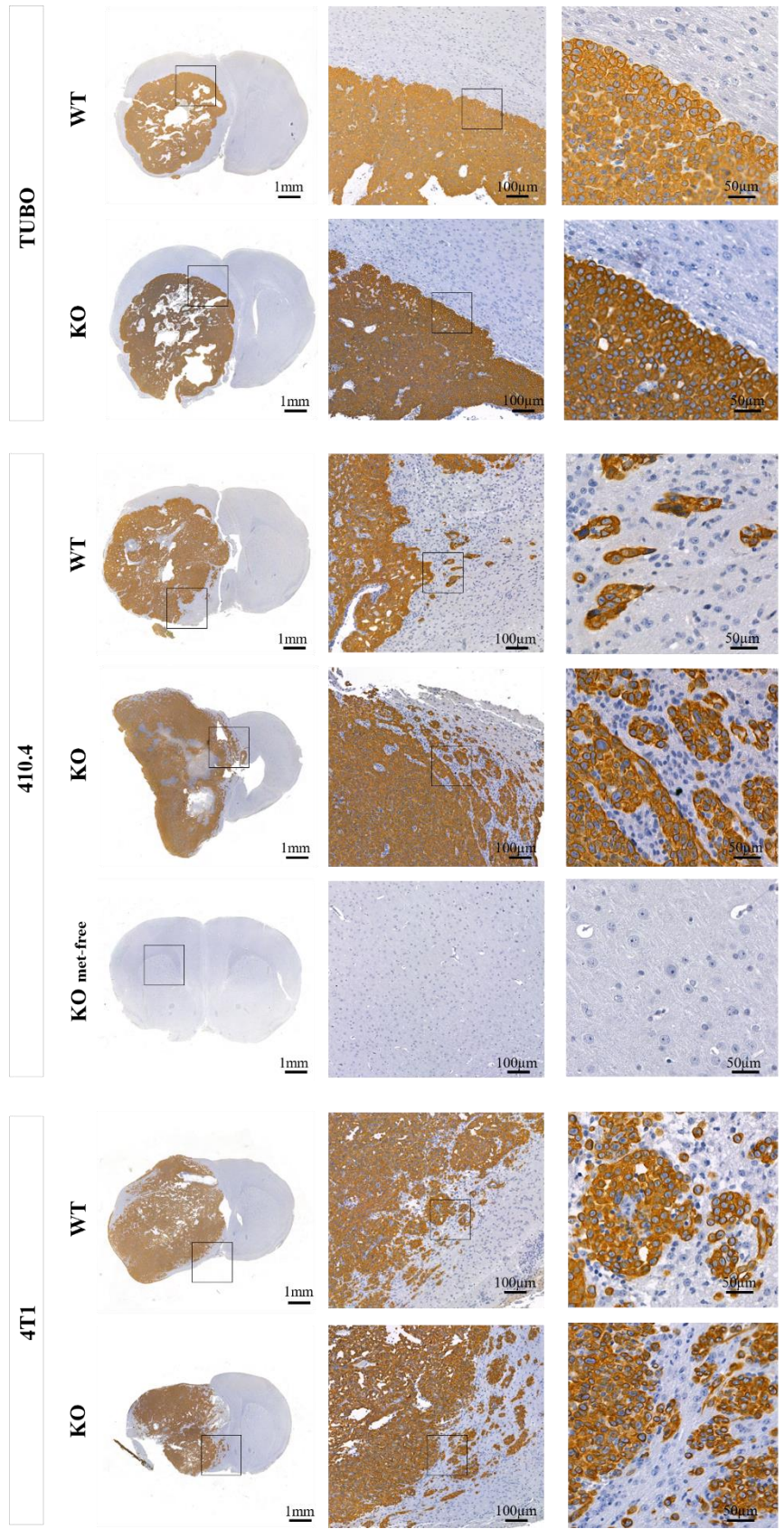


Figure 27. Effects of IL4-signaling knockout in BCBM mouse models on MMPI. IHC staining of cytokeratin 8 (Ck8) in tissue sections of 4T1, TUBO and 410.4 brain metastases. Representative images of coronal brain sections of WT and KO mice and images of their MMPI at higher magnifications are shown.

Taken together, these results claim that only the 410.4 BM model is sensitive to modulation of IL4 signaling, resulting in a prolongation of the survival rate. Although no changes in the colonization pattern were observed between WT and KO models, the CI was reduced up to 28% in 410.4-injected KO mice. In the TUBO “cold tumor” model, however, blockade of IL4 signaling generated wide metastases comparable in survival rate, CI and colonization pattern at the MMPI to those observed in WT mice. The same was observed for the 4T1 BM model. In this context, it is worth highlighting the paradox that, even though both 410.4 and 4T1 are representative “hot tumor” models, no survival advantage was observed in KO mice injected with the 4T1 cell line. This incognita will be further addressed later in this work.

3.3.3.2. The microenvironment in BM of IL4R knockout mice

The influence of IL4 signaling on the immunological landscape of the brain-MME was evaluated immunohistologically and at protein expression level as previously described. Again, characterization of activated microglia/macrophages, astrocytic activation and T cells were assessed by use of Iba1, Gfap and Cd3 markers, respectively, emphasizing the differences found in brain metastatic tissues of WT and KO mice.

3.3.3.2.1. Characterization of MG/MDM in the metastatic brain of IL4R knockout mice

Both tissue-resident MG and recruited MDMs comprise the tumor-associated macrophage (TAM) population in brain tumors, considered among the major immune-suppressive components of the brain-MME when polarized to their M2 phenotype state (Klemm et al., 2020). The precise contribution of the two ontogenetically distinct TAM cell types in BM is unclear, albeit our previous findings suggest that IL4 signaling may contribute to their immunosuppressive functioning by triggering their M2-polarization state. In that context, IL4R KO mice could be used as a therapeutic strategy to potentially diminish the M2-TAM population available in a brain-MME and, consequently, its immunosuppressive component.

Overall, the MG/MDM distribution pattern remained similar in WT and KO mice irrespective of the cell line with which they were injected. In all cases, Iba1-positive macrophages were found in the metastatic core and at the MMPI of metastatic tissues, as previously described in this work, and no activated MG/MDM were observed in the not-injected hemisphere. Specifically, in the case of the “hot tumor” model 410.4, a macroscopic decrease of the activated MG/MDM population could be observed in KO mice, suggesting a direct effect of IL4 signaling disruption in the availability of M2-MG/MDM in the metastatic core. Metastasis-free brains of KO mice injected with 410.4 showed a relaxed, star-shaped MG/MDM population, confirming that injection-induced damage is the trigger for macrophage activation (Figure 28A).

Gene expression analysis of *Iba1* gene expression levels confirmed the lack of significant differences in macrophage population density between metastatic tissues of WT and KO mice in all three BM models. As expected, a significant decrease of *Iba1* was observed in 410.4-injected metastasis-free KO brain tissues, with lower expression levels compared to metastatic tissues from WT or metastatic-KO mice (Figure 28B).

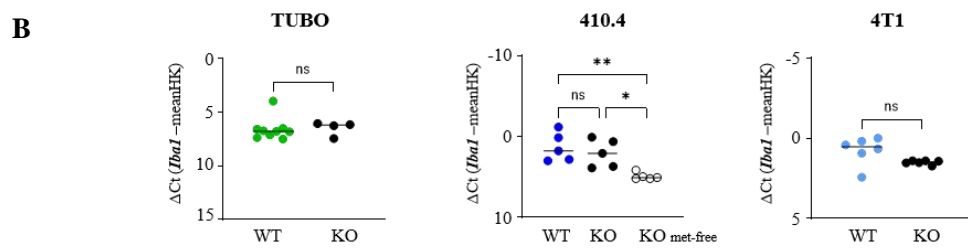
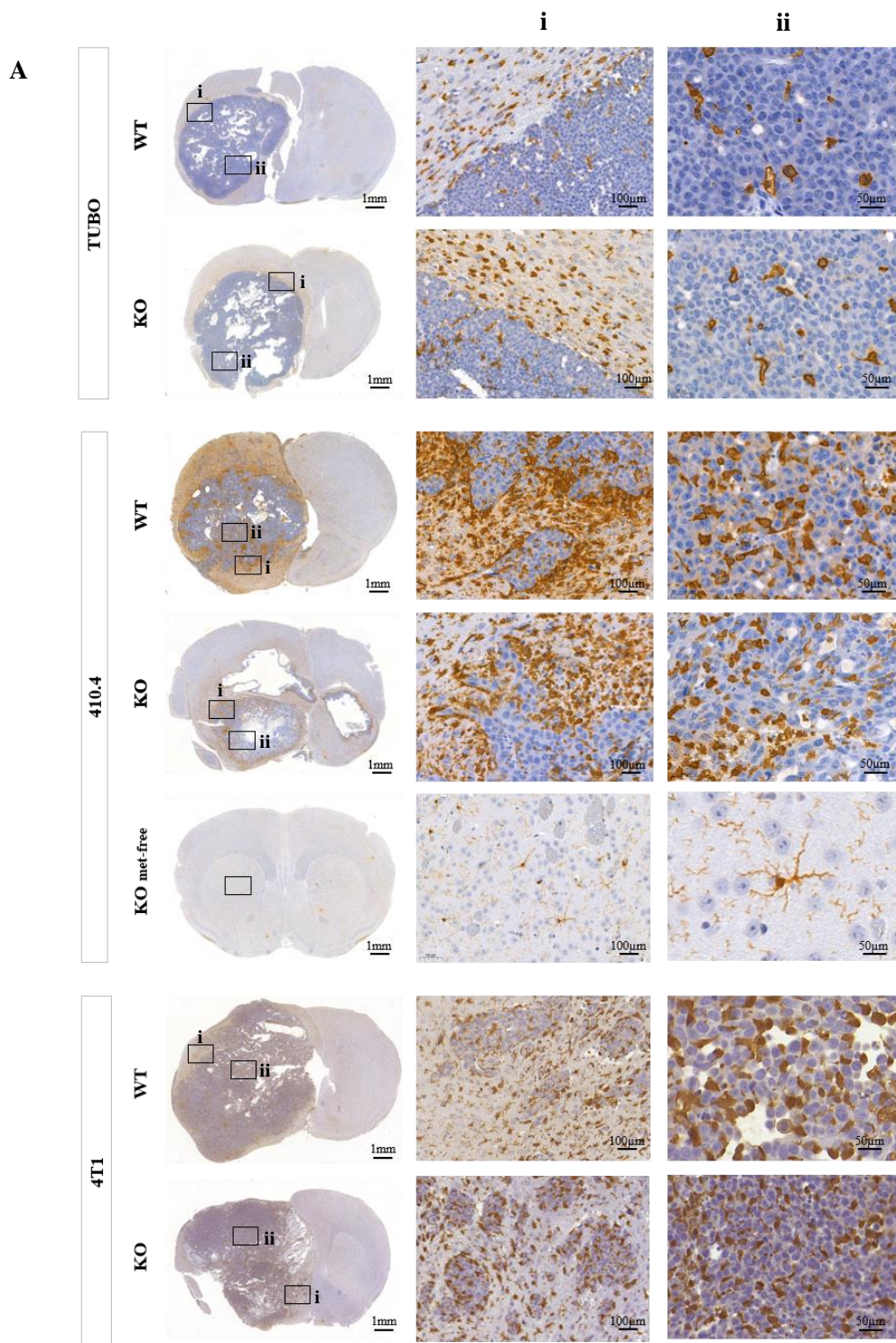


Figure 28. Characterization of MG/MDM population in the metastatic brain of IL4R WT and KO mice. **A)** IHC images of brain tissues after staining of MG/MDM populations with Iba1 marker of WT and KO mice injected with BCBM models TUBO, 410.4 and 4T1. Representative images of coronal brain sections and magnifications of the MMPI (i) and metastatic core (ii) are shown. **B)** Comparative real-time PCR analysis of *Iba1* gene expression levels between WT and KO-derived brain tissues injected with the corresponding BM model (TUBO, 410.4 or 4T1). *Gapdh* and *Pgk1* were used as housekeeping (HK) genes. P-value was calculated with one-way ANOVA followed by Tukey's multiple comparisons or unpaired t-student (*p<0.05, **p<0.01, ns=not significant).

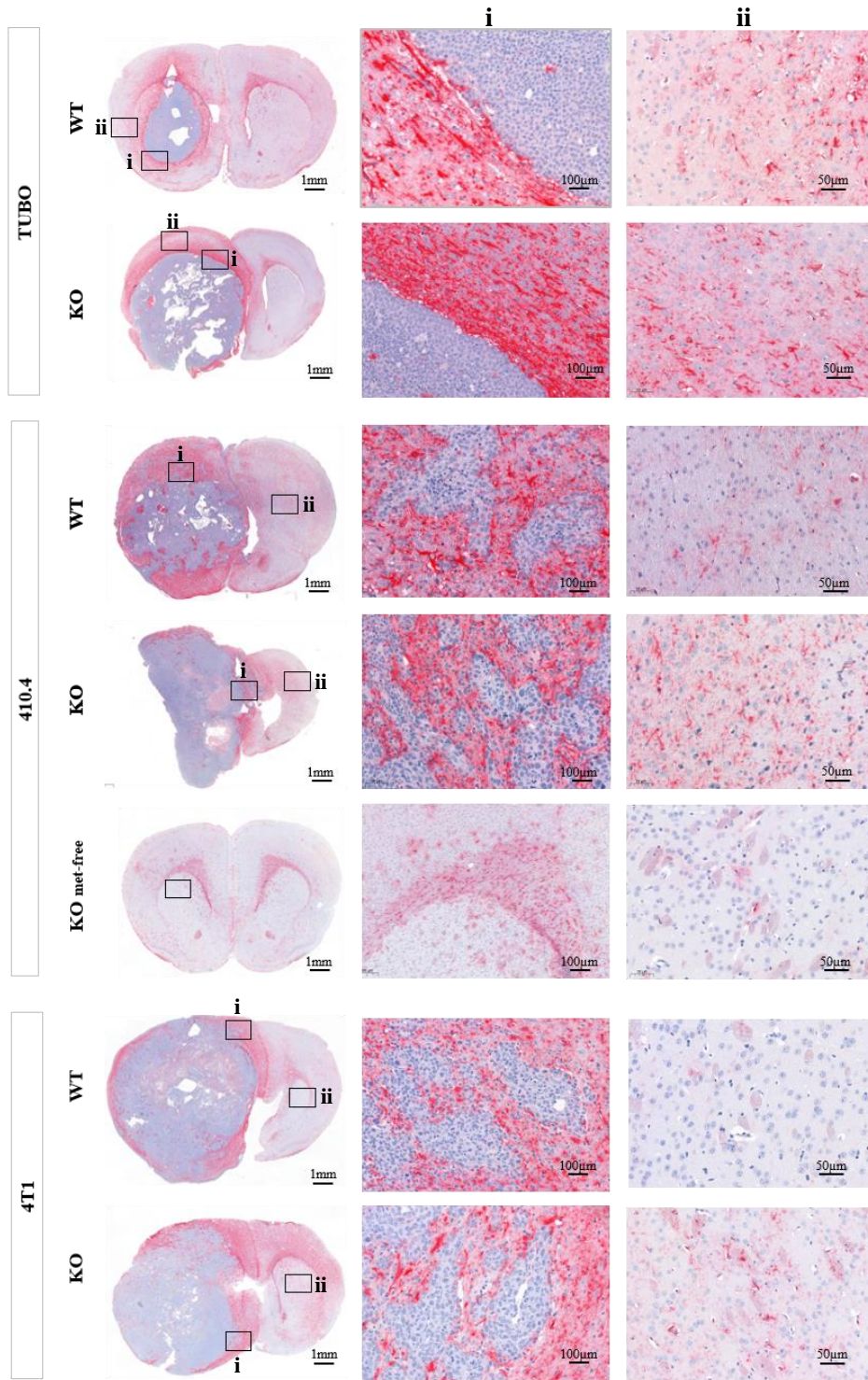
3.3.3.2.2. Characterization of astrocytes in the metastatic brain of IL4R KO mice

Astrocytes may also display metastasis-inducing behaviour in an organ-dependent manner. Particularly in the brain-MME, astrocytes relate to the enhancement of immunosuppressive PI3K signaling and increased outgrowth of brain metastatic cells. Given their ontogenetic proximity to TAMs and their link to signaling pathways active in immunosuppressive MG/MDMs, such as PI3K signaling, exploring the contributions of reactive astrocytes at the immunological level in mice deprived of IL4 signaling seemed an attractive scenario (Doron et al., 2019).

As can be seen in Figure 29, reactive astrocytes were found exclusively in the proximities of metastatic areas and without differentially populating metastatic tissues of WT or KO-injected mice. In the case of TUBO, the glial ring around the tumor mass remained prominent regardless of the activation of IL4 signaling, with no infiltration of *Gfap*-positive cells into the metastatic core. In the 410.4 and 4T1 “hot tumor” models, the reactive astrocyte population showed identical population profiles in WT or KO mice, with large clusters of *Gfap*-positive cells surrounding the tumor infiltrates. Furthermore, the absence of metastatic damage in 410.4-injected KO mice was accompanied by an absence of astrocytic activation. No astrocyte infiltration to the metastatic core was observed. The cell population of the non-injected hemisphere showed stellate morphology, typical of a non-astrocytic activation state (Figure 29A).

These observations could be confirmed by means of real-time PCR analysis (Figure 29B). No significant differences in the expression of the astrocytic marker *Gfap* between WT or KO mice injected with the corresponding BM models. As with MG/MDMs, tumor-free tissues from surviving 410.4-injected KO mice reported a significant reduction in *Gfap* compared to metastatic tissues from metastatic KO and WT mice.

A



B

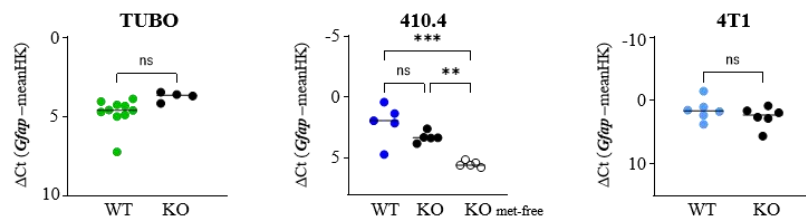


Figure 29. Characterization of astrocyte population in the metastatic brain of IL4R WT and KO mice. A) IHC images of brain tissues after staining of astrocyte populations with Gfap marker of WT and KO mice injected with BCBM models TUBO, 410.4 and 4T1. Representative images of coronal brain sections and magnifications of the MMPI (i) and adjacent parenchyma (ii) are shown. B) Comparative real-time PCR analysis of *Gfap* gene expression levels between WT and KO-derived brain tissues injected with the corresponding BM model (TUBO, 410.4 or 4T1). *Gapdh* and *Pgk1* were used as housekeeping (HK) genes. P-value was calculated with one-way ANOVA followed by Tukey's multiple comparisons or unpaired t-student (**p<0.01, ***p<0.001, ns=not significant).

3.3.3.2.3. Characterization of T cells in the metastatic brain of IL4R KO mice

T cell-mediated responses are minimal under normal physiological contexts. However, cell functions can be strongly altered by environmental cues within the local brain microenvironment (Platten et al., 2014). Considering that IL4 is a molecule secreted and produced in the context of brain-MME, the potential alterations of the immunosuppressive function of the T-cell compartment were evaluated in the absence of functional IL4 signaling.

As previously described for the WT mice models, no infiltrating T-cells were found in the metastatic core or at the MMPI of TUBO-injected KO mice, reinforcing our notions of an immunologically “cold tumor” model. In 410.4 and 4T1 models, in turn, similar Cd3-positive cell numbers can be observed in metastatic tissues derived from WT and KO mice. In the case of the “hot tumor” models, infiltrating Cd3-positive cells were found throughout the entire metastatic area as well as at the MMPI of infiltrating tumor regions. As reported in the case of reactive astrocytic populations or activated MG/MDMs, no traces of T cell activity could be found in tumor-free 410.4-injected KO mice (Figure 30A).

These immunological findings were further contrasted by analysis of gene expression levels of the *Cd3* marker by real-time PCR (Figure 30B). No significant differences were found among metastatic tissues from WT and KO mice in any of the three models of BM. In addition, 410.4-injected tumor-free KO mice displayed an acute decrease of *Cd3* expression levels, as expected given the absence of brain parenchymal damage.

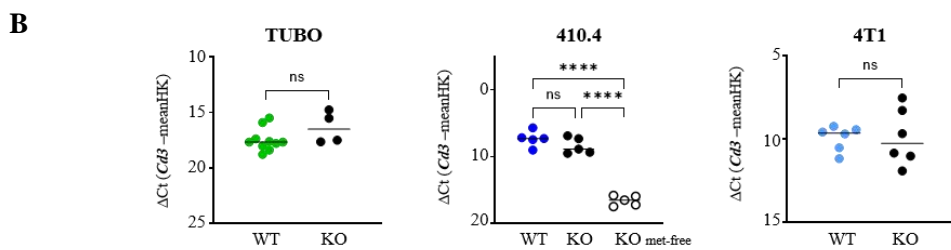
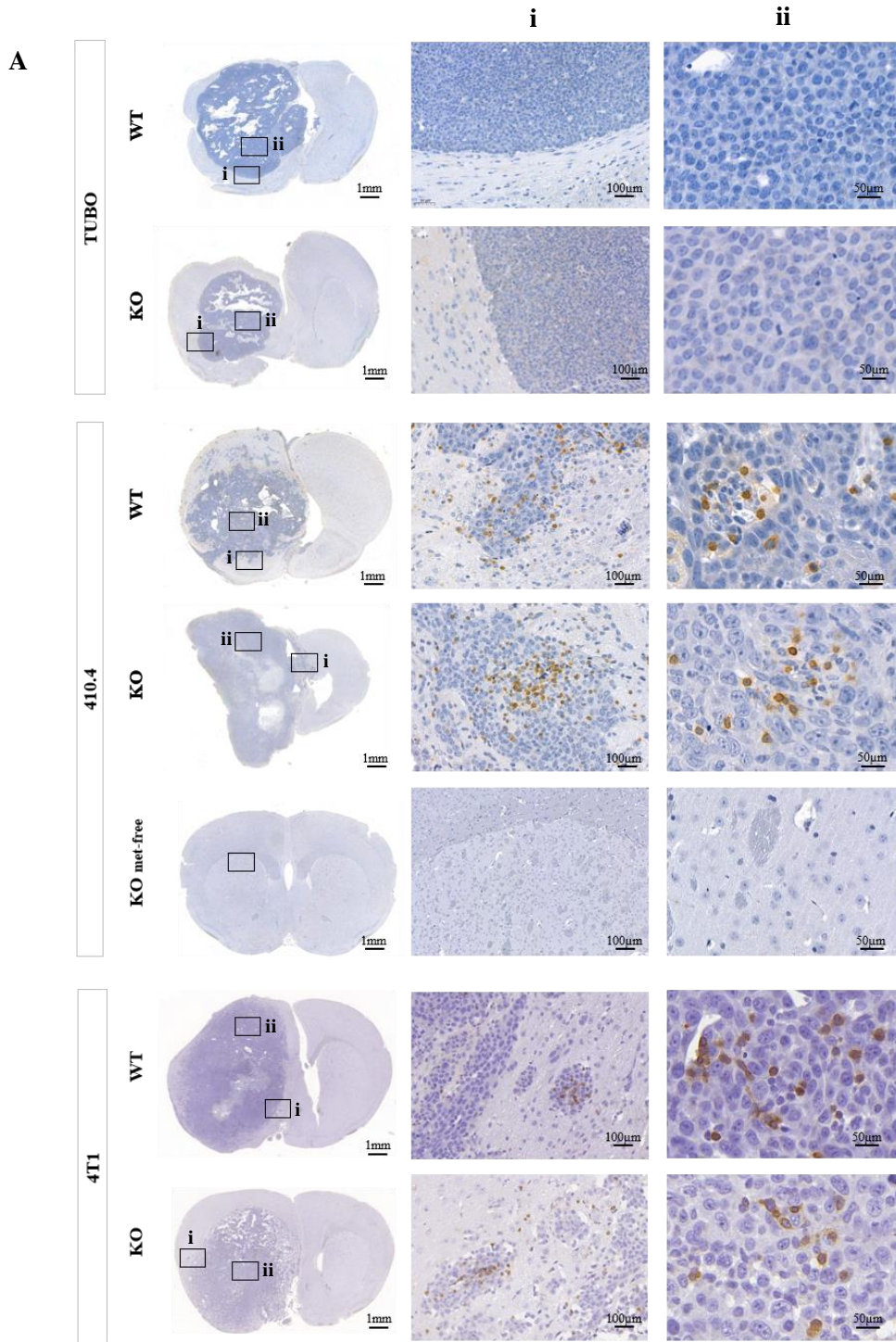


Figure 30. Characterization of T cell population in the metastatic brain of IL4 signaling KO mice. A) IHC images of brain tissues after staining of T cell populations with Cd3 marker of WT and KO mice injected with BCBM models TUBO, 410.4 and 4T1. Representative images of coronal brain sections and magnifications of the MMPI (i) and metastatic core (ii) are shown. B) Comparative real-time PCR analysis of *Cd3* gene expression levels between WT and KO-derived brain tissues injected with the corresponding BM model (TUBO, 410.4 or 4T1). *Gapdh* and *Pgk1* were used as housekeeping (HK) genes. P-value was calculated with one-way ANOVA followed by Tukey's multiple comparisons or unpaired t-student ****p<0.0001, ns=not significant).

Taken together, evaluation of the immune compartment in a brain-MME context revealed an abrupt change in the distribution of the immune population among WT and KO tumor-bearing mice only upon injection of the epithelial infiltrative 410.4 model. While no differences were observed among metastatic tissues from WT and KO mice injected with TUBO, or 4T1 BM models, a robust decrease of activated MG/MDMs, reactive astrocytes and infiltrative- T cell populations was widely detected in surviving 410.4 KO mice.

3.3.3.3. Therapeutic approach to IL4R- signaling

Characterization of the immune landscape in metastatic brain tissues identified the 4T1 and 410.4 BM models as highly immunogenic tumor inducers with associated strong recruitment of different immune populations, including T cells ("hot tumors"). While modulation of IL4 signaling was sufficient for the acquisition of survival advantage in the 410.4 model, 4T1 displayed resistance to such blockade, indicating the need for further investigation of a major weakness of the hot tumor model.

Immunotherapy, represented by immune checkpoint inhibitors (ICI), mediates antitumor responses depending on the infiltration of T cells. Given the high frequency of T cells in the 4T1 model, the use of immune therapies to boost antitumor immune responses emerged as a promising strategy in the framework of this project. Particularly, combined immune checkpoint blockade (ICB), based on the use of antibodies that neutralize the T cells inhibitory receptors cytotoxic T-lymphocyte antigen 4 (CTLA-4) and programmed cell death protein 1 (PD-1), is known to lead to sustained activation of the immune response provided by T cells with unprecedented efficacy in disease outcomes in different types of cancer patients (Seidel et al., 2018).

In an attempt to achieve a synergistic effect from blockade of the IL4 signaling and prolonged T-cell antitumor activity, syngeneic WT and KO immunocompetent mice were injected with the 4T1 cell line and treated with a cocktail containing both anti-CTLA-4 and anti-PD-1 monoclonal antibody (mAb). Mice treated with PBS alone were used as controls. Additionally, since cold tumors are characterized by the lack

of T-cell infiltration, TUBO was used as negative control of the ICB effectiveness. In the case of survival of the mice, a total of nine doses were administered, with alternating injections every 3 and 4 days (Figure 31A).

As immune-desert model, no differences in OS after ICB treatment was expected in TUBO-injected WT and KO mice. Consistent with our expectations, treatment of WT mice with PBS (control) or ICB showed symptoms of disease very early after tumor injection (median OS^{WT} = 20.5 days; OS^{KO} = 23.5 days). In the ICB-treated KO mice, only one mortality event was observed, with an overall survival of three weeks after injection (median OS = 23 days). All KO mice in the control group showed a similar dynamic, with metastatic symptomatology starting about three weeks after tumor injection (median OS = 22.5) (Figure 31B).

On the other hand, given previous evidence of immune infiltration in tissues derived from the 4T1 “hot tumor” model, a rescue effect was expected in tumor-bearing KO mice. According to the data, however, only 1/6 KO mice injected with the 4T1 cell line survived with no metastatic symptoms after ICB-treatment, while 5/6 died quickly (mean OS = 20 days). The same scenario was captured by PBS-treated KO mice (mean OS = 20 days). Similarly, all tumor-bearing WT mice, whether ICB- or PBS-treated, had very short survival rates, developing metastases around three weeks after stereotactic injection (median OS^{WT} = 22.5 days; median OS^{KO} = 21 days) (Figure 31C).

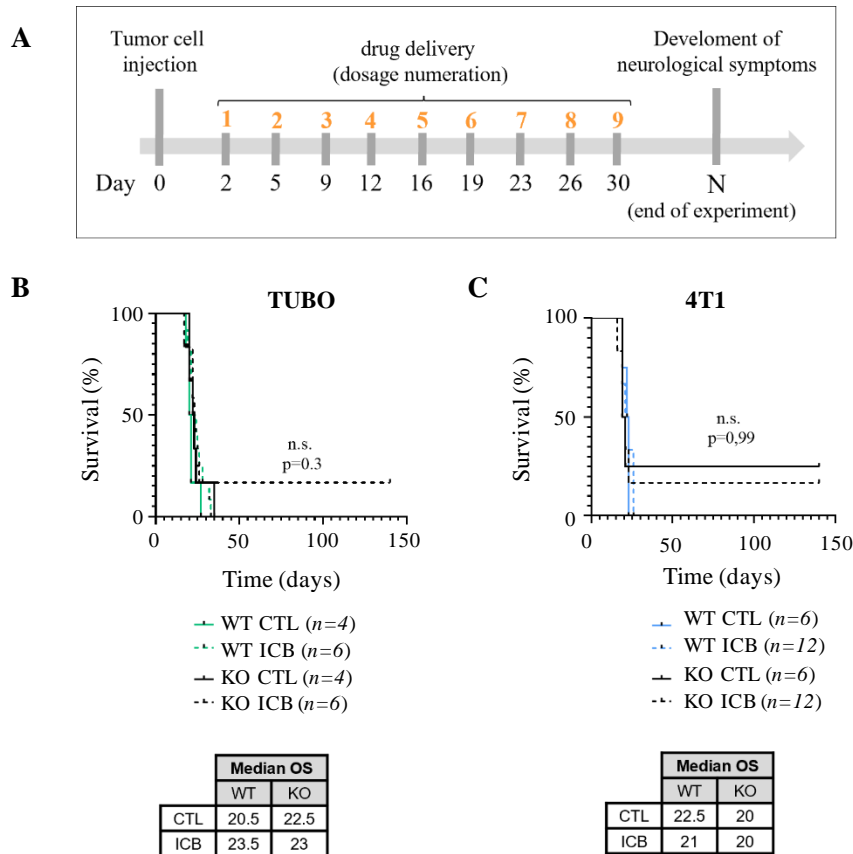


Figure 31. Effect of ICB therapy in IL4R knockout mice. A) Scheme of the *in vivo* experimental setting during ICB administration. Kaplan-Meier curve of overall survival of controls (PBS treated) and ICB-treated syngeneic mice injected with B) 4T1 or C) TUBO breast cancer cell lines. 10^3 tumor cells were injected in all cases. Statistical analysis conducted with Log-rank (Mantel-Cox) test (4T1-ICB, n=2; TUBO-ICB, n=3, n.s. = not significant).

The above results support previous findings regarding the unresponsiveness of “cold tumor” models to ICI (Bonaventura et al., 2019). However, contrary to expectations, the high infiltrating T cell population in the tumor mass of 4T1-injected metastatic brains, coupled with the prevention of immunosuppressive M2 phenotype polarization of MG/MDM, was not sufficient to trigger susceptibility to ICB therapy in 4T1-injected KO mice. These results suggest that this model of IL4 signaling inhibition at a general level may not be the right approach to study the immunosuppressive character of MG/MDM in a brain metastatic context.

3.3.3.4. MDM conditional IL4R KO mouse model

In contrast to cancer cells, microglia and MDMs are genetically stable and predictable cells, making them an attractive malleable target for cancer therapies. Due to the upcoming relevance of MG/MGM as sculptors of the immunosuppressive niche, one important aim of this thesis was to assess the specific role of IL4 signaling in both myeloid populations in our BM models. As shown in the figure above, general disruption of IL4 signaling did not prove to be a valid approach in our BM models for a precise understanding of IL4 signaling during BCBM. Instead, a new therapeutic strategy based on the blockade of IL4 functioning in a cell-specific manner was assessed by using conditional MDM-IL4R α KO mouse models.

Shortly, the creation of a cell-specific IL4R α -KO model was assessed by use of the Cre-loxP technology (see Methodology 2.1.1.3.1) and the lysozyme M (LysM) as a promoter, exclusively expressed in myelomonocytic cells including monocytes, macrophages and granulocytes. Originally, this experimental block aimed to conduct experiments with conditional KO mice specific for the MG and MDM populations. Unfortunately, due to delays in crossbreeding of Cre driver mouse strains, experiments could only be carried out on MDM-specific KO mice. Based on previous findings of high sensitivity to IL4 signaling modulation, conditional KO mice were injected with the 410.4 BM model.

Only 4/13 of the conditional IL4R KO mice survived with no metastatic symptoms upon 410.4 injections, while 9/13 developed metastatic symptoms and a mean OS of 85 days. Regarding the control mice, 8/10 died with a median OS of 70 days after intracortical injection, showing a survival rate of 20% (Figure 32). No significant differences were found between control and conditional-KO mice.

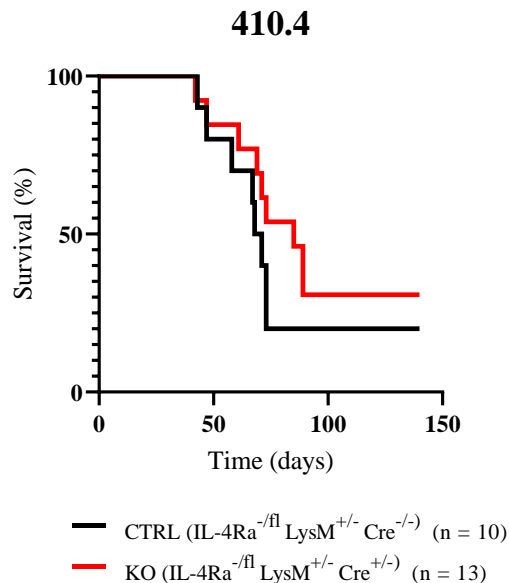


Figure 32. Effect of MDM-specific IL4 signaling knockout in 410.4 BM model. Kaplan-Meier curve of overall survival of CTL and MDM-specific KO mice injected with 410.4 cell line. Statistical analysis conducted with Log-rank (Mantel-Cox) test (P=0,28).

Given the absence of the Cre enzyme, control mice should behave identically to WT mice (Figure 11). However, 20% of the control mice survived following injection of the 410.4 cell line, suggesting a failure in the generation of the genetic modifications in the experimental mice.

Collectively, the IL4 signaling modulation did not lead to significant differences in the survival rate between control and MDM conditional-KO mice. However, given the unexpected survival of the genetically engineered control mice, it cannot be concluded that the MDM population comprised in the brain-MME is not responsible for the better prognosis in conditional-KO mice, but rather that the control selected is not the appropriate one to carry out this experiment. Instead, further experiments are required in order to determine whether the absence of MG/MDM polarized into their pro-tumor M2 phenotype because of the lack of functional IL4 receptor results in prolonged survival of KO mice.

3.4. Explanation for IL4 signaling modulation sensitivity of 410.4 model

In order to find out the nature of the dissimilar sensitivities to IL4 signaling of the selected models, the gene expression signature of metastatic brain tissues from WT and KO-injected mice as well as metastasis-free tissues from KO 410.4 injected mice were analyzed. An extensive panel of molecular markers was used including immune population tracers, general pro- and anti-inflammatory cytokines, cell death-associated biomarkers and specific MDM/MG-M2-polarization state markers (Figure 33A). Stereotactic injection of TUBO resulted in overexpression of anti-inflammatory *IL10* and M2-MDM *Cxcl13* as well as downregulation of the M2-MDM/MG marker *MMP12* in KO metastatic tissues, compared to WT samples (Figure 33B). Gene expression signature in 410.4-derived metastatic tissues revealed *IL10* and the iron-related *Hoi1* (heme oxygenase-1) genes significantly overexpressed in metastatic-KO tissues compared to the WTs. Moreover, *Il4ra* and the M2-MG related- *Fnl* (fibronectin-1) genes were significantly downregulated in metastatic-KO brain tissues compared to WT samples. Interestingly, no significant changes were observed in the expression levels of *Nqo1* (Quinone Oxidoreductase 1) between WT and KO-derived metastatic tissues, albeit strongly upregulated in metastasis-free KO samples compared to metastatic KO samples (Figure 33C). In the case of the 4T1 model, significant differences were exclusively found in the M2-MDM marker *Cxcl13*, downregulated in metastatic-KO tissues compared to the WT (Figure 33D).

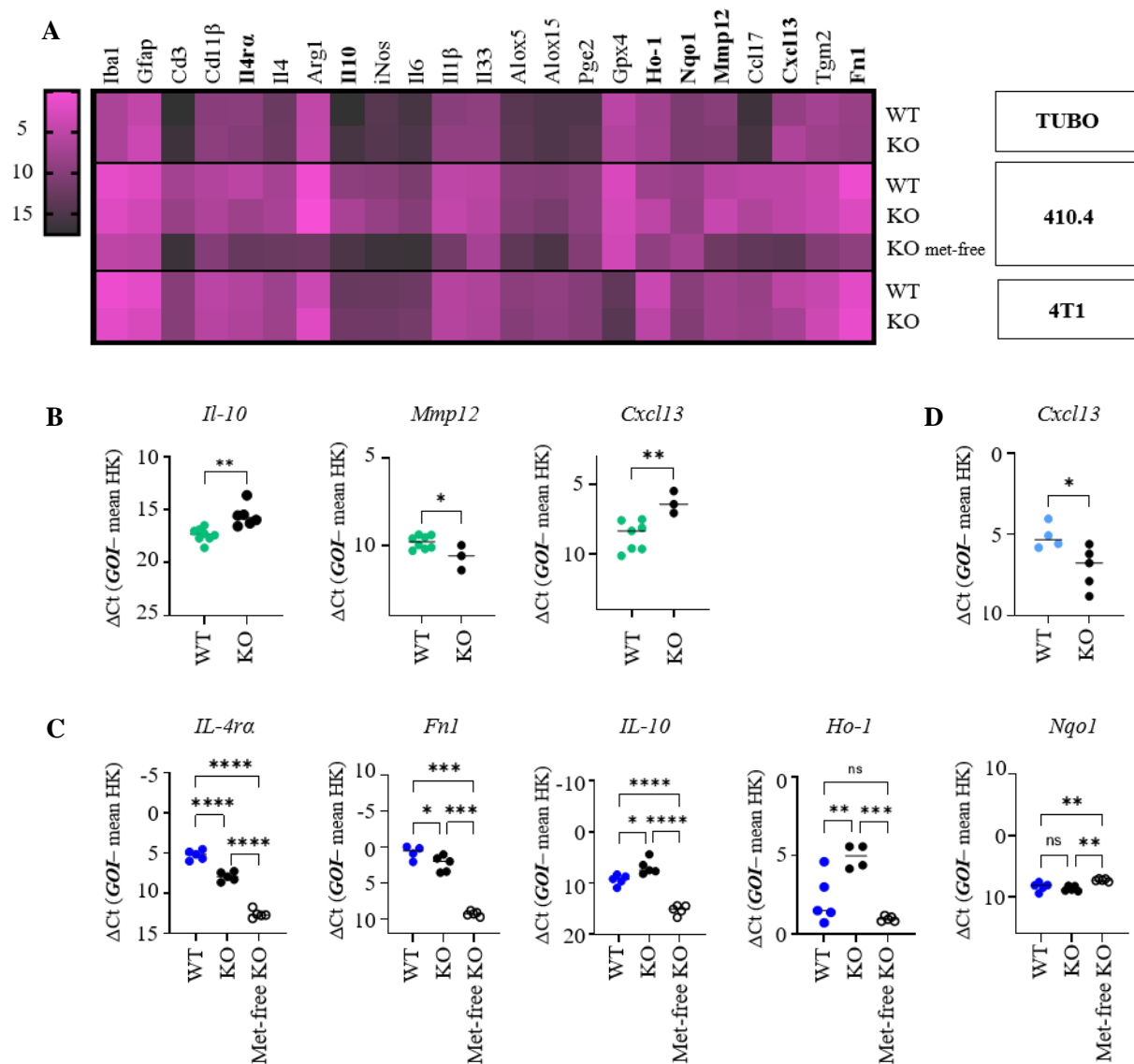


Figure 33. Gene expression signature in IL4 signaling KO metastatic tissues. **A)** Heatmap of fold change displaying quantitative RT-PCR analysis of a broad panel of molecular markers developed in metastatic tissue from WT and KO mice and metastasis-free tissues from KO mice after corresponding injection of TUBO, 410.4 or 4T1. **B)** Representative graphics of significantly regulated genes in metastatic brain tissues derived from TUBO-injected mice (WTvsKO). **C)** Representative graphics of significantly regulated genes in brain tissues derived from 410.4-injected mice (WTvsKO). Met-free KO refers to KO mice free of metastasis. **D)** Representative graphics of significantly regulated genes in metastatic brain tissues derived from 4T1-injected mice (WTvsKO). (Individual values, $n \geq 4$; One-way ANOVA followed by Tukey's multiple comparisons or unpaired t-student; * $P < 0.05$, ** $P < 0.01$, *** $P < 0.001$, **** $P < 0.0001$).

According to the findings, the absence of IL4 signaling is enough to prevent M2-polarization state of MG/MDM in the three selected BM models, but only 410.4 metastatic tissues suggest a major role of MG population in WT mice according to strong downregulation of *Fnl* gene expression.

To deepen the paradox of 410.4 sensitivity versus 4T1 resistance to IL4 signaling modulation, it is worth recalling the contrasts in the epithelial condition among the 410.4 and the 4T1 cell lines. As previously described in this thesis (Figure 8B and Figure 9B, C), the 410.4 cell line is represented as epithelial characterized by high expression of the epithelial marker E-cadherin, while 4T1 is defined as an epithelial cell line with mesenchymal-like features characterized by low E-cadherin and high Vimentin expression. Previous findings reported by this group and others suggest that the acquisition of a mesenchymal-like cellular state of breast cancer cells predicts sensitivity to a particular type of cell death known as ferroptosis (Trigueros et al., 2020, submitted; Viswanathan et al., 2017). Thus, to investigate the potential link between ferroptosis-cell death and IL4 signaling activation, basal expression of pro-tumoral and ferroptosis-related genes was assessed and compared among metastatic tissues from WT-injected mice.

As for the TUBO immune desert model, the expression profile of all genes was significantly decreased compared to both 410.4 and 4T1, with the only exception of *Gpx4*, overexpressed compared to 4T1-metastatic tissues. In turn, no significant differences in the expression levels of *IL4*, the macrophage M2-polarization markers *Tgm2*, *Fnl*, *Pge2* (Prostaglandin E2) and the lipid peroxidation tracers *Alox5* (Arachidonate 5-Lipoxygenase) and *Alox15* (Arachidonate 15-Lipoxygenase) were observed between 410.4- and 4T1-metastatic tissues. Interestingly, *IL10*, *Arg1* and the anti-ferroptosis markers *Nqo1* and *Gpx4* (Glutathione Peroxidase 4) were overexpressed at 410.4 compared to 4T1, and only *Hol* gene expression was strongly upregulated in 4T1 metastatic tissues compared to 410.4. Since ferroptosis occurrence is strongly associated with iron metabolism, the gene expression changes of iron-related molecules were also assessed. Particularly, *Blvrb*, *Fth1* and *Ncoa4* were strongly downregulated in TUBO, revealing comparable higher expression rates in the “hot tumor” models 410.4 and 4T1 (Figure 34).

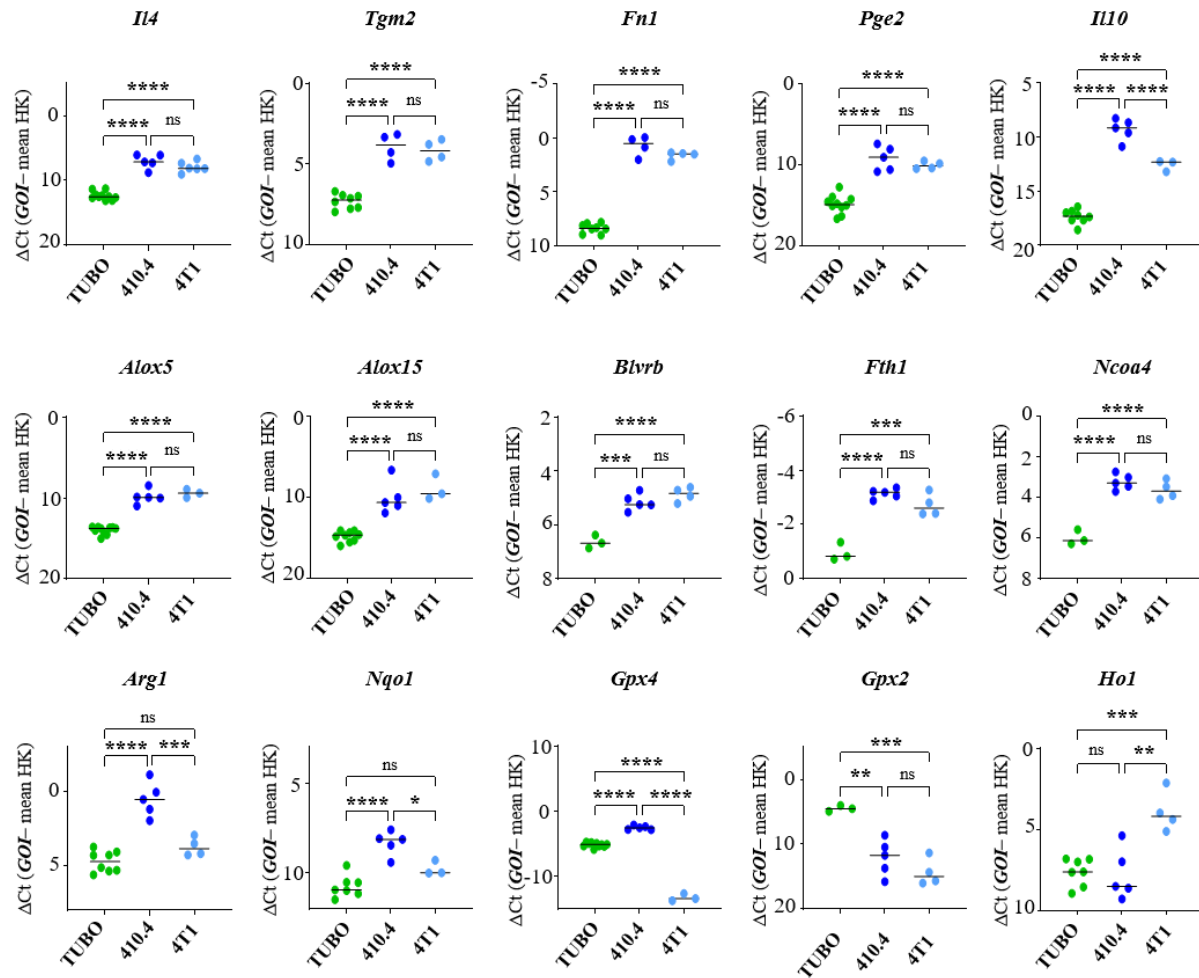


Figure 34. Comparative quantitative RT-PCR analysis of gene expression signature across WT-derived metastatic tissue. *Gapdh* and *Pgk1* were used as housekeeping genes (HK; mean and individual values; $n \geq 3$; one-way ANOVA followed by Tukey's multiple comparisons; * $P < 0.05$, ** $P < 0.01$, *** $P < 0.001$, **** $P < 0.0001$, n.s. = not significant).

Given the suggestion of strong discrepancies in the strengthening of the detoxifying systems among the 4T1 and 410.4 cell lines previously published in our group (Blazquez et al., 2020A), investigating the susceptibility of the cell lines to ROS emerged as an important target. In that context, a series of functional 3D co-cultures were carried out, yielding information on the sensitivity of the BM model cell lines to cell death by ROS accumulation.

3.4.1. ROS sensitivity in BCBM models

The sensitivity of tumor cells towards pathophysiological stress situations was analyzed by using the previously described multi-cellular 3D tumor spheroid model: the hanging drop assay. Broadly, 3D cell culture models represent a bridge between 2D cell culture and animal models, strikingly mimicking tissue microenvironment and approaching the cellular context of *in vivo* cancer, including metastatic outgrowth in the brain. The similarities of these spheroids to human tumors in terms of their necrotic and proliferative zones make them particularly suitable for studying cellular interactions *in vitro* close to what occurs in an animal model (Ravi et al., 2014).

The resulting tumor spheroids showed quite dissimilar structures with contrasting degrees of compactness (Figure 35A). The spheroid growth was measured over 72 hours, pointing to TUBO as the cell line producing the smallest spheroids over time. The 4T1 spheroids displayed the highest growth rate over time, followed by 410.4. The same tendency was observed at 72h, with the 4T1 spheroids showing the largest spheroid size, followed by 410.4, and TUBO considerably smaller spheroids (Figure 35B).

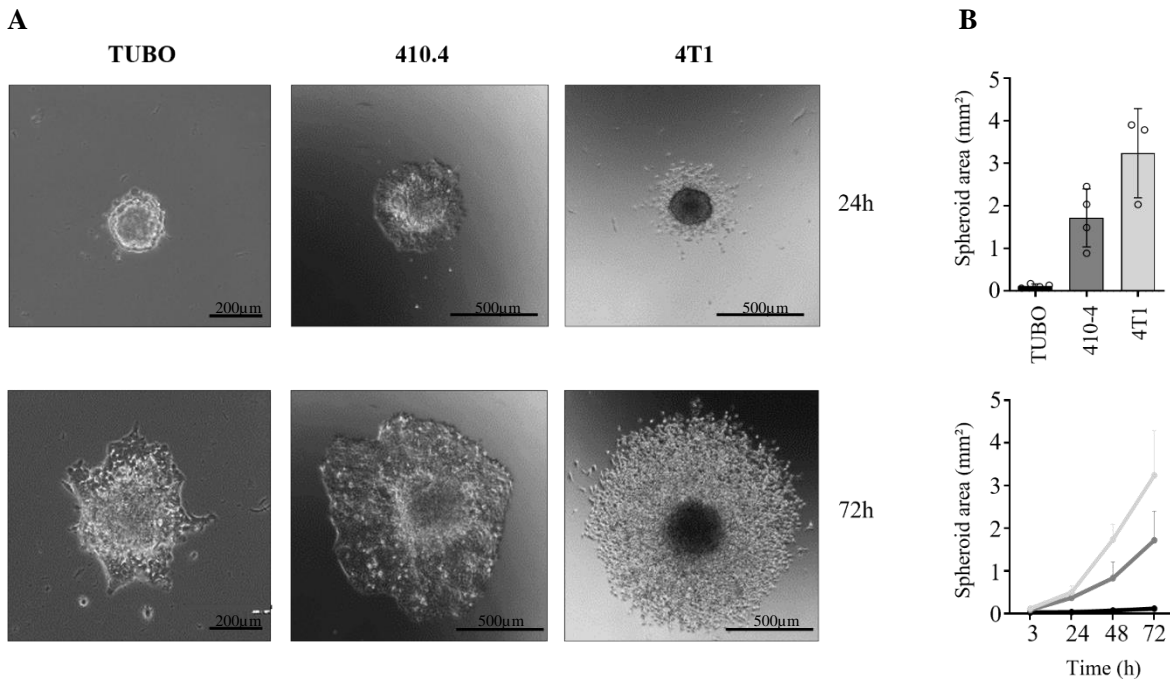


Figure 35. Functional 3D characterization of murine BM model cell lines. A) Representative bright field images of tumor cell spheroids. **B)** Spheroid outgrowth is indicated in mm² over time and displayed separately after 72h in mm².

As functional proof of concept, spheroids of the three cell lines were treated with buthionine sulfoximine (BSO), an inhibitor of GSH biosynthesis that leads to overproduction of reactive oxygen species (ROS) and triggers cell death, at increasing concentrations ranging from 10 to 50 μ M. Murine BM models were described as resistant or sensitive to ROS accumulation-induced cell death according to their decrease in spheroid size over time. All tumor spheroids decreased in size at increasing concentrations of BSO (Figure 36B). However, while TUBO spheroids revealed slightly high sensitivity to BSO treatment, with a decrease of approx. 35% of the spheroid size at 10 μ M, the 410.4 spheroids displayed a particularly high sensitivity to BSO, with a size reduction of up to 60% compared to the control. Conversely, spheroids consisting of the 4T1 cell line showed a size reduction of approximately 7% after ROS treatment. (Figure 36C).

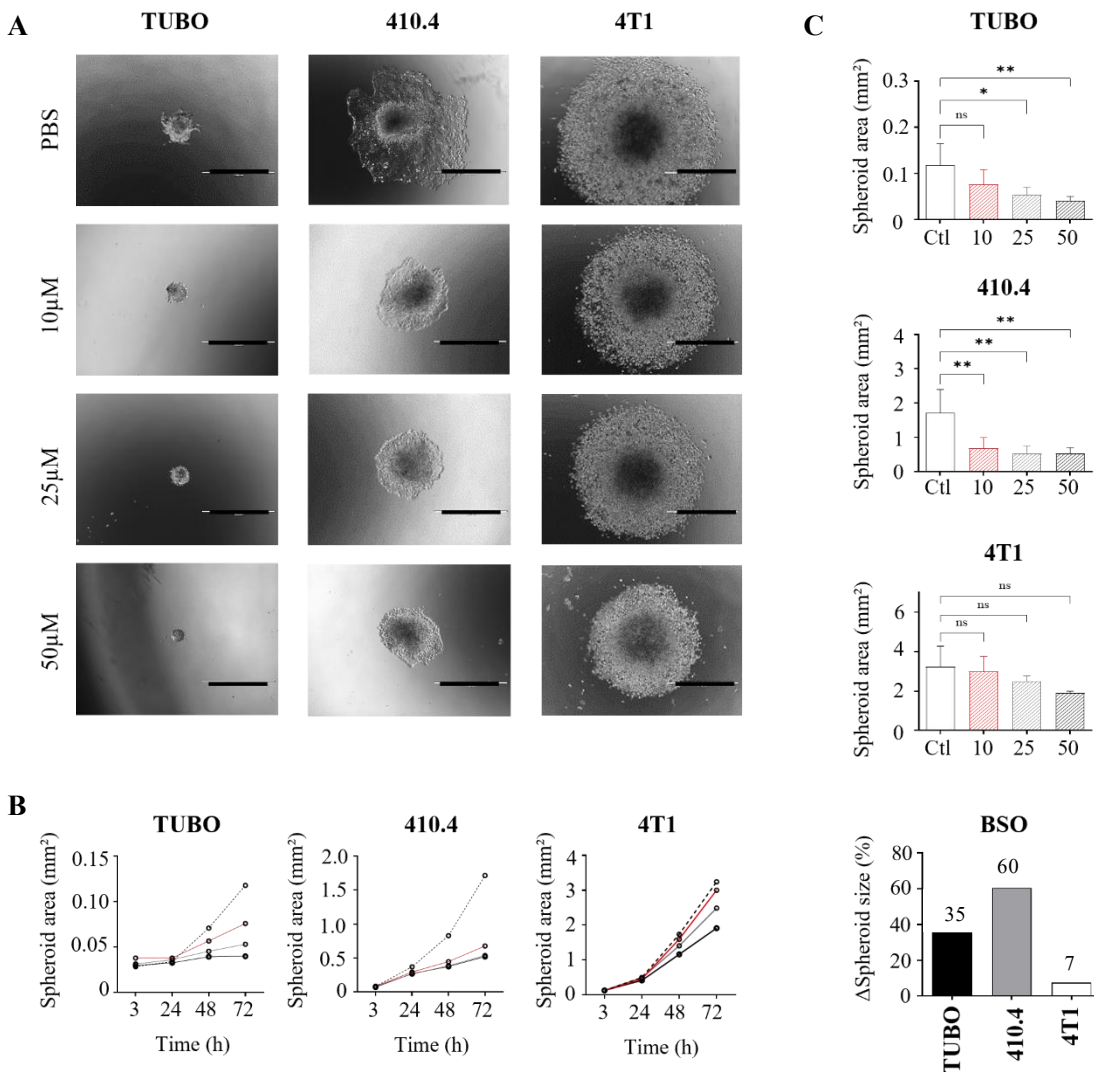


Figure 36. Effects of BSO in murine BM model cell lines *in vitro*. **A)** Representative images of spheroid decrease at 72h with different concentrations of BSO. Scale bars represent 250 μ m. **B)** Spheroid outgrowth

decrease under BSO stimulation over time. C) Spheroid outgrowth decrease under BSO stimulation (μM) at 72h for each cell line and percentage of spheroid size decrease at 10 μM BSO (CTRL-10 μM) (mean + SD, n = 3; one-way ANOVA followed by Dunnett's multiple comparisons test; *P < 0.05, **P < 0.01, n.s. = not significant).

Altogether, the TUBO and 4T1 cell lines show low sensitivity to detrimental BSO effect, with strong resistance to GSH inhibition-induced cell death. In turn, the 410.4 cell line is highly sensitive to GSH inhibition, resulting in an acute decrease of the spheroid size upon BSO treatment.

4. Discussion

The lethality of brain metastasis remains unavoidable and the underlying mechanism responsible for its fatality is largely unknown to the scientific community. The existence of biological differences within the metastatic cascade among patients and delayed clinical detection further increases the fatal nature of the disease, so greater clarity on the most decisive step of the metastasis, the colonization of the brain parenchyma, as well as in the formation of the macro-metastasis may be key in the search for new therapeutic approaches against brain metastasis. In this regard, this thesis aims to shed light on the different patterns of brain colonization at the level of the MMPI, area of prognostic impact, specifically in the context of intact or blocked IL4 signaling, a major activator of the immune system response. Additionally, addressing the effects of IL4 signaling pathway blockade is understood as a therapeutic approach to immunosuppression of the metastatic niche with a special focus on the TAM population, favouring thus the understanding of metastatic colonization of the CNS.

4.1. Comparison of MMPI colonization models in the CNS

The pattern of colonization of tumor cells at the MMPI has been shown to have a prognostic impact on different types of metastasis (Siam et al., 2015; Blazquez et al., 2020B), identifying the MMPI patterns as a clinically relevant tool. The existence of different MMPI patterns has been related to the occurrence of distinct pathomechanisms driving metastatic progression, suggesting the existence of divergent potential therapeutic targets against metastatic colonization. The major prognostic feature of the MMPI patterns refers to the grade of infiltration of the metastasis, finding the worst survival rates in patients with highly infiltrative MMPIs (Blazquez et al., 2020B). However, the study of the underlying biological mechanisms of colonization requires a broad representation of the MMPI patterns observed in human brain metastasis. Accordingly, this study used syngeneic mouse models of brain metastasis that represent both infiltrative and non-infiltrative patterns of MMPI.

4.1.1. Impact of E/M status of metastatic tumor cells in MMPI patterns

Three murine BCBM model cell lines were used throughout this study: the TNs 410.4 and 4T1 models, and the HER2+ TUBO model. They were intracortically injected into immunocompetent syngeneic mice, resulting in occurrence of wide symptomatic metastases in all cases. Interestingly, the performance of comprehensive IHC analysis of metastatic brains revealed highly divergent MMPI patterns among the selected brain colonization mouse models. While the 410.4 and 4T1 models exhibited infiltrative

colonization with clusters of cells embedding into the healthy parenchyma, the TUBO model showed well-defined non-infiltrative colonization of tumor cells that did not squeeze through healthy parenchyma but rather colonized by compression of adjacent tissues. Some of these MMPI patterns (4T1 and 410.4) have previously been described in the literature (Blazquez et al., 2020B), consolidating consistency in the experimental strategy. Unlike the 410.4 and 4T1 models, established as infiltrative models of late brain colonization in our laboratory years ago (Blazquez et al., 2020), the colonizing pattern of TUBO and its quality as a model of brain metastasis was until now completely unknown. Thus, the establishment of TUBO as a non-infiltrative MMPI pattern *in vivo* model of brain metastasis represents a first major milestone of this study.

Given the marked differences in the pattern of colonization at the MMPI among the selected models, the question arises as to what factors determine it. All three cell lines were proved to be adherent and displayed an epithelial phenotype *in vitro* and *in vivo*, albeit they showed prominent differences in their epithelial/mesenchymal (E/M) status. No changes in the EMT or MET phenotype of the cell lines integrated in the metastatic niche were found in any of the three selected mouse models. Instead, levels of epithelial and mesenchymal markers between the *in vitro* and the *in vivo* scenarios remained stable and proportional (Yang et al., 2020). Nevertheless, protein and gene expression level analysis as well as histological and immunofluorescence staining in 2D and 3D, revealed a gradual epithelial condition among TUBO, 410.4 and 4T1 models, respectively. The levels of E/M marker expression, including E-cadherin and vimentin, were identified as one of the key differences between non-infiltrative and infiltrative MMPI models.

The non-infiltrative TUBO model was characterized as a highly epithelial cell line, with high expression of the epithelial markers Ecad, or Ck19 both *in vitro* and *in vivo*. Increased levels of E-cadherin have been previously associated with an increased rate of cell-cell contacts that maintain the cells adhered to one another, reducing infiltration rate of the tumor cells and resulting in a lower incidence of metastasis in cancer patients (Li et al., 2017). Although the gain of epithelial features is believed to result in decreased tumor aggressiveness and prolonged host survival according to the current EMT theory (Yang et al., 2020), injection of the non-infiltrative TUBO model surprisingly led to metastatic symptom development and subsequent fatality of mice in short term. Thus, contrary to the previously reported correlation between non-infiltrative MMPIs and good prognosis in patients (Siam et al., 2015), the highly epithelial non-infiltrative TUBO model revealed a very high colonization capacity (CI=0.5) and metastatic potential.

In turn, the association between infiltrative MMPIs and unfavourable prognosis (Blazquez et al., 2020B) was reinforced in the 410.4 and 4T1 models. The infiltrative 410.4 model showed significant epithelial features, although lower than those exhibited by TUBO, and behaved as expected according to previous publications (Blazquez et al., 2020B), revealing a moderate colonization rate (CI=0.196) and maintaining

its epithelial character during the metastatic development. Strikingly, the infiltrative 4T1 model revealed significantly reduced expression of Ecad epithelial marker and prominent upregulation of the mesenchymal marker vimentin compared to the 410.4 model, but especially to the TUBO model, which led us to define the 4T1 cell line as epithelial with mesenchymal features. The acquisition of mesenchymal features in the 4T1 epithelial model was very well appreciated in the 3D tumor spheroid models, characterized by their trustable ability to mimic *in vivo* conditions, thus pointing to 4T1 as a model of hybrid E/M phenotype, a process known as “partial EMT” (Saitoh, 2018). The injection of syngeneic mice with the infiltrative 4T1 model resulted in rapid fatality and exhibition of high colonization capacity (CI=0.4). In line with these results, lower levels of E-cadherin are believed to result in lower cell-cell adhesion contacts, which could facilitate deeper infiltration of the cells into the adjacent tissues, resulting in poor prognosis and survival (Wong et al., 2018). Accordingly, the high metastatic potential of the infiltrative 4T1 model revealed *in vivo* could be a consequence of its hybrid E/M phenotype.

4.1.1.1. E/M cellular status impacts immunotherapy

Recent research focused on the revision of the classic EMT theory claimed that carcinoma cells transit along a continuum of multiple fluctuating intermediate states ranging from epithelial to mesenchymal extremes. Far from the exhibition of epithelial or mesenchymal purity of metastatic cells during colonization, EMT programmes may be activated only partially and contextually (Lambert et al., 2017). Carcinoma cells transiting the middle of the epithelial-mesenchymal spectrum comprise phenotypic plasticity that is believed to be crucial for metastatic growth (Lambert et al., 2017; Saitoh, 2018). In these terms, invasiveness of carcinoma cells would no longer depend on complete activation of the EMT/MET programme. Instead, tumor progression and metastasis have been related to partial E/M status of cancer cells (Lambert et al., 2017). Furthermore, the phenotypic diversity of tumor cells populating a single tumor mass is known as tumoral heterogeneity and is considered one of the most important drivers to therapy resistance (Saitoh, 2018). Some pioneering studies show that acquisition of partial E/M status maximize tumorigenic activity of cancer cells (Jolly et al., 2015). Particularly, the acquisition of mesenchymal-like features of epithelial cancer cells has been related to increased migration and aggressiveness of cancer cells and lower prognosis and survival rates of patients (Saitoh, 2018). As an example, the most aggressive molecular subgroups of breast cancer have been shown to have partial E/M state (Yu et al., 2013). Among others, nuclear factor erythroid 2-related factor 2 (Nrf2) was proposed to prevent progression towards a complete EMT and stabilize the hybrid E/M state, leading thus to an increased metastatic potential (Bocci et al., 2018).

Collectively, the evidences suggest that reprogramming of partial E/M state of cancer cells to fully mesenchymal or epithelial states, with less phenotypic plasticity, is a potentially promising therapeutic strategy. However, the effects of partial E/M on chemotherapy, radiotherapy, or immunotherapy led by blockade of Nfr2 or any other partial E/M inducer are yet completely unknown. In this context, the description of the infiltrative 4T1 model as an epithelial cell line with mesenchymal features facilitates its potential inclusion in future experimental models to further explore a relevant therapeutic impact.

4.2. Impact of the MMPI pattern on immune infiltration

The MMPI is presumed to determine the pattern of immune infiltration during brain metastasis and thus the host organ immune response, severely influencing the outcome of the disease (Siam et al., 2015; Blazquez et al., 2020). However, no published study to date supports such a suggestion. To further investigate the relationship between immune infiltration and MMPI, different immune populations including activated macrophages, astrocytes and T cells were analyzed in metastatic tissues injected with the three selected BCBM models.

The infiltrative colonizers 4T1 and 410.4 models revealed extensive immune infiltration of all interrogated immune populations. As previously described by others (Andreou et al., 2017), microglial/ macrophage infiltration in the metastatic niche is a robust feature of metastatic outgrowth in the brain. Additionally, in this study, we emphasize the presence of large aggregates of Iba1-positive cells in both 4T1 and 410.4 models. Similarly, infiltrating T cells were found in the metastatic core and at the MMPI, distinguishing however a significant increase of the Cd3-positive populations in 410.4-derived metastatic tissues compared to 4T1-derived metastatic tissues. Activated astrocytic populations, in turn, were found exclusively overlapping with the MMPI, with no signs of infiltration to the metastatic core in both models. In all cases, macroscopic findings were confirmed by gene expression of immune-specific markers, leading solidly to the association between infiltrative MMPI patterns and highly immunogenic tumors. The non-infiltrative colonizer TUBO model, however, revealed extraordinarily low levels of immune infiltration for all interrogated immune populations. Only small clusters of activated microglia/MDM were observed in the metastatic core and no apparent accumulation of Iba-1 positive cells was observed at the MMPI compared to the infiltrative models. Yet, a prominent reactive astroglial envelope was found at the MMPI, massively bordering the metastatic mass. This pseudo-capsule has been previously well-described in our lab and identified the displacing metastatic growth pattern at the MMPI of the TUBO model (Blazquez et al., 2020B). Strikingly, no trace of infiltrating T-cells was found intratumorally or at the MMPI, revealing a metastatic landscape deserted of Cd3-positive cells. Interestingly, the glial-reaction occurring at the MMPI

of displacing non-infiltrative models has been previously related to an orchestrated defence mechanism against CNS-foreign intruders (Siam et al., 2015; Blazquez et al., 2020). In this example, the glial envelope consisting of astroglia and microglia cells serves as a brake on tumor progression of non-infiltrative cells. However, far from it, the non-infiltrative TUBO model has been described as a very high colonizer, with an increased colonization capacity even comparable with the highly colonizing 4T1 model. Thus, it could be precisely the presence of the microglial ring at the MMPI which promotes the high aggressiveness of TUBO (Siam et al., 2015). Accordingly, the presence of microglia and other macrophage populations at the immunosuppressive brain-MME could facilitate the tumoral invasion of TUBO, providing metastatic survival advantages.

Collectively, these results confirm the close relationship between MMPI colonizing patterns and metastatic infiltration of immune cells. Taking into account the degree of immune cell infiltration of each model (Liu et al., 2021), infiltrative MMPI models can be robustly related to highly immunogenic "hot tumor" models, in which a potent immune response is triggered as a consequence of the tumor cell-immune compartment interaction at the MMPI. Likewise, the non-infiltrative MMPI model can be associated with the immune desert "cold tumor" model.

The lack of tumor-infiltrating T cells in "immune-desert tumors" is strongly involved in initial resistance to immune checkpoints inhibitors (ICI) (Bonaventura et al., 2019). Instead, ICI shows a better efficacy mainly associated with "hot tumors", characterized by significant T-cell infiltration. Thus, "cold tumors" resistance to ICIs evolve as the main challenge for the future of immunotherapy, and their conversion into immune responsive "hot" models has emerged as a major aimed strategy (Bonaventura et al., 2019). However, the paucity of reproducible murine models of cold tumors represents a major obstacle in the development of therapeutic strategies against ICI resistance. Strikingly, the non-infiltrative TUBO model established in this study accounts for one of the first cold tumor syngeneic models ever settled, providing a fundamental tool in the development of new therapeutic approaches to drive T cells into tumors and contributing to the transition from "cold tumors" to "hot tumors".

4.3. IL4 as an immune activator in brain metastasis

The Th2-like cytokine IL4 was used in this work as activator of the immune response in the context of the brain metastatic environment. Its role as major immunosuppressive effector of the MME was confirmed by *in vitro* characterization of the cytokine expression profile of metastatic tissues (*in vivo*) and cultured tumor cell lines (*in vitro*). However, the use of IL4-R α KO mice, for which the interleukin receptor remained non-functional, revealed no direct association between disrupted IL4 signaling and shifting in the colonization

pattern at the MMPI of any of the selected BCBM models. Despite this, they showed vastly diverse sensitivities to IL4 signaling silencing *in vivo*. As was to be expected, the non-infiltrative “cold tumor” TUBO model exhibited no response to the manipulation/modulation of IL4 signaling, with occurrence of wide metastases comparable in survival rate, CI and colonization pattern at the MMPI in WT and KO tumor-bearing mice. Consistently with its status of “immune desert”, the scope for interaction with the surrounding MME was too marginal to unleash an immune response, leading to minimal differences in the gene expression signature between *in vitro* and *in vivo* measurements.

On the other hand, highly immunogenic "hot tumor" models, which exhibited important changes in their gene expression signature among *in vitro* and *in vivo* measurements that could be directly translated into shaping of the brain-MME, were expected to respond with high sensitivity to disruption of IL4 signaling. Outstandingly, the injection of the infiltrative 4T1 model showed no alteration of the survival rate among WT and KO tumor-bearing mice, in its CI or in its colonization pattern at the MMPI. In turn, the injection of the 410.4 resulted in a significant prolongation of the OS in 12/18 injected KO animals by up to 20 weeks (limited time according to the animal ethic plans included in the project). The high sensitivity to IL4 signaling modulation *in vivo* of 410.4-injected KO mice further resulted in marked decrease of the colonization potential to less than 1/3 (CI=0.056) compared to WT mice (CI=0.196).

Furthermore, evaluation of the immunological landscape at immunohistological and gene expression levels revealed no significant changes in the interrogated immune populations in the IL4 no responsive models, TUBO and 4T1. However, the distribution of the immune landscape was abruptly shifted in the surviving 410.4-injected KO compared to the WT tumor-bearing mice. In these, the immune infiltration associated with the chronic inflammation resulting from the metastatic events failed to develop or disappeared completely. Consequently, no traces of reactive macrophages or astroglial populations were observed and no infiltrating T-cells were found in the tissues of non-metastatic KO mice.

Taken together, disruption of IL4 signaling induces a reduction of the metastatic potential of the epithelial infiltrative “hot tumor” 410.4 model exclusively, resulting in abrupt change of the immune infiltration pattern in no tumor-bearing KO animals. Not without surprise, the hybrid E/M infiltrative “hot tumor” 4T1 model show fierce resistance to IL4 modulation despite displaying very similar immunogenic status, comparable pattern of colonization in the MMPI and even belonging to the same molecular subgroup of breast cancer.

4.3.1. Immunotherapy in IL4R α -KO models

Characterization of IL4 signaling in microglia/MDM and the BM models *in vitro* revealed a potential involvement of the TAM population as an immunosuppressive component of brain-MME. Activation of the downstream effector P-Stat6, induction of IL4-mediated morphological changes and regulation of gene expression of well-known anti-inflammatory genes including *Arg1* and *IL10* in the macrophages indicated that changes observed *in vivo* at the MME must be due to the effect of IL4 on the TAM population. Contrary, tumor cells *per se* did not show morphological modifications or gene signature changes upon IL4-treatment.

Aiming to encourage a synergistic effect resulting from the shutdown of immunosuppression and the reactivation of the T-cell immune response, WT and IL4R α KO mice injected with the selected BCBM models were subjected to ICI therapy. Unresponsiveness of “cold tumor” models to ICI previously claimed by others (Bonaventura et al., 2019; Liu et al., 2021) was confirmed in this work, where a cocktail containing both anti-CTLA-4 and anti-PD-1 mAb failed to prolong overall survival of TUBO-injected mice. As expected, no effects of ICI treatment on survival were observed in the “immune-desert” model independently of the status of the IL4 signaling. The same treatment was administered to WT and KO mice injected with the highly immunogenic “hot tumor” model 4T1. Contrary to expectations, it was not sufficient to trigger susceptibility to ICB therapy. This fact may be associated with the partial E/M character of the 4T1 model, which, as mentioned above, is related to a higher resistance to immunotherapy due to greater cellular plasticity (Saitoh, 2018). Additionally, a significant increase in T-cell infiltration was observed in metastatic tissues derived from 410.4-injected mice compared to 4T1, so it would have been interesting to investigate whether the survival rate of the KO mice increased even further after administration of the combined immunotherapy.

Importantly, inhibition of IL4 signaling was conducted at a general level, and not in a cell-specific manner, which may not be the right approach to study the immunosuppressive character of MG/MDM in a brain metastatic context. With the purpose of assessing the effect of immunosuppressive M2 phenotype polarization prevention in MDM through IL4 signaling disruption, MDM conditional IL4R α -KO mouse models were further used in this study. These experiment aimed to prove if the absence of MDM polarized to their pro-tumor M2 phenotype because of the lack of functional IL4 receptor resulted in prolonged survival of MDM-specific IL4-R α -KO mice. In other words, to check if MDMs are main contributors of the pro-tumor activities of IL4 signaling during brain metastasis. In line with the results, the effect of IL4 signaling modulation on survival rate of 410.4-injected mice does not seem to rely primarily on infiltrating MDMs comprising the brain-MME, since survival of WT and MDM-specific IL4-R α -KO injected mice exhibited similar OS rates. Due to the delay in acquiring these conditional KO mice and the time constraint

of the PhD, brain tissues derived from this experimental approach could not be processed, and comprehensive analysis of the MMPI colonization pattern and immune infiltration in these mice are still pending. Furthermore, this experiment had an additional limitation, as the control mice have been found to carry an incomplete genetic modification: IL4R α gene is heterozygous, carrying only one unmodified allele encoding the functional receptor protein. Although theoretically the possession of a single allele is sufficient to maintain IL4R functionality, in practice we find the opposite scenario, where control mice, which previously died when injected with 410.4 cell line, now survive. This suggests that on the way to heterozygous modification of the control mice, part of the IL4R α coding message has been lost. However, this assumption needs to be further evaluated.

4.4. ROS fitness as a driver for IL4 sensitivity

Given the pronounced immune infiltration in both "hot tumor" models, one may wonder what makes 4T1 model resistant while 410.4 model proves to be highly sensitive to IL4 modulation. In other words, what prevents this "partial EMT" cancer cell line from sensitivity to IL4 signaling? There are many similarities between the 410.4 and 4T1 murine brain metastasis models. Among others, both are epithelial breast cancer cell lines representative of TN molecular subtype with an infiltrating colonization pattern at the MMPI that generates massive metastatic tumors with a similarly high pattern of immune infiltration. Yet, the differences among them appear to be sufficient to determine their resistance/sensitivity to modulation of the IL4 signaling pathway. Differences in the colonization potential (CI) or the increased T-cell infiltration in the 410.4 model are final evidence of a biological divergence that must have begun long before macroscopic metastasis formation.

Among the most striking molecular differences between 4T1 and 410.4 cell lines may be their divergent metabolic flexibility in terms of ROS metabolism. Aware of the benefit of 3D tumor models to mimic the *in vivo* context, hanging drop assays performed in this study revealed a profound sensitivity of 410.4 spheroids to GSH inhibition and consequent reactive oxygen species (ROS) accumulation. A decrease of the spheroid size of up to 60% was observed in 410.4 spheroids treated with BSO, a proved potent GSH inhibitor, compared to the controls, while 4T1 spheroids showed a near absolute resistance to the extracellular increase in ROS upon BSO treatment. In this regard, ROS resistance could be understood as a key difference in the colonizing capacity of the 4T1 cell line, mapping a potential link between the ROS metabolic capacity of the cell line, its "partial EMT" status and its lack of responsiveness to IL4 signaling modulation. Interestingly, ROS resistance of epithelial cancer cells has been previously related to boosting intracellular GSH levels and acquisition of survival advantages during brain colonization (Blazquez et al.,

2020). Former studies associated the ROS-related cell death observed in 410.4 spheroids with the acquisition of lower detoxifying related genes including GSH and a concomitant reduction of the pair GSH/GSSG, directly related to an increase in cytotoxic ROS levels (Blazquez et al., 2020).

The inhibition of GSH has been further related to a specific type of cell death different from apoptosis, necrosis or any other type of previously described cell death event, known as ferroptosis. As introduced earlier in this study (see Introduction 1.3.1), ferroptosis is an iron-dependent form of cell death triggered by the accumulation of lipid-based ROS (Li et al., 2020). Thus, ferroptosis susceptibility is tightly related to ROS sensitivity, so it could be thought that the key discrepancy between the 4T1 and 410.4 models resides in their resistance or sensitivity to ferroptosis, respectively. The link BSO sensitivity – ferroptosis occurrence in the 410.4 model was addressed by analysis of the gene expression signature in IL4R α -KO metastatic tissues. Among the variety of genes analyzed, the iron-related *Hol* revealed significantly higher expression levels in KO mice compared to WT and metastasis-free KO mice. *Hol* gene is known to exert a dual role in ferroptosis, able to confer both a cytoprotective role against reactive oxygen species (ROS)-mediated stress conditions and a detrimental role by mediating the induction of ferroptosis, depending on its degree of activation (Chiang et al., 2019). Importantly, in an over-activated state, the *Hol* gene is related to iron-dependent lipid peroxidation and intracellular ROS levels upregulation, resulting in ferroptotic cell death induction. Thus, *Hol* overexpression in 410.4-KO metastatic tissues suggests the existence of a potential link between IL4 signaling and ferroptosis in 410.4-induced metastasis development. Furthermore, downregulation of the antioxidant protein *Nqo1* was observed in metastatic 410.4-KO mice compared to metastasis-free 410.4-KO mice, suggesting an increase in intracellular ROS accumulation by the decrease of anti-oxidant molecules upon IL4 signaling disruption.

Additionally, comparative analysis of gene expression signature across WT-derived metastatic tissue of the three selected models revealed a significant upregulation of the IL4-mediated anti-inflammatory markers *Arg1* and *IL10* and the antioxidant molecules *Nqo1* and *Gpx4* and a pronounced downregulation of the *Hol* gene in the 410.4 model compared to the 4T1 model. *Nqo1* and *GPX4* promote buffering of the toxic effects of ROS accumulation, while decreased *Hol* expression may be related to its cytoprotective effect, indicating a rather protective role of the metabolic mechanism in presence of functional IL4 signaling particularly in the infiltrative 410.4 model. Moreover, the high mortality observed in 4T1-injected mice irrespective of IL4 modulation and the reduced availability of *Nqo1* and *Gpx4* genes in the 4T1 metastatic tissues suggested the existence of alternative and inherent detoxification mechanisms in the cell line that allow coping with cytotoxic stress and provide survival advantages. Particularly, a recent publication of our group revealed that BSO sensitivity of BCBM model cell lines with different E/M status correlates with their metastatic potential in terms of their colonization index in the brain (CI^{brain}), (Trigueros et al., 2020,

submitted). Altogether, the reported higher resistance of the 4T1 model to BSO treatment suggests great ROS flexibility and potential resistance to ferroptotic-cell death. Contrary, 410.4 sensitivity to ROS accumulation mediated- cell death potentially underlines its susceptibility to ferroptosis.

Due to the precise prerequisites for the occurrence of ferroptosis, GSH metabolism is closely linked to iron metabolism. In line with this, we recently postulated that escaping ferroptosis cell death depends on the activation of iron-dependent antioxidant mechanisms during metastatic colonization for tumor cells displaying a diffuse infiltrative colonization pattern at the MMPI. That is the case of the TNBC cell line EO771-LG, highly characterized for acquisition of mesenchymal features and partial loss of its epithelial character (Trigueros et al., 2020, submitted). However, no significant differences were found at gene expression level of iron-dependent antioxidant markers *Blvrb*, *Fth1* or *Ncoa4* in metastatic samples derived from 4T1 tumor-bearing mice compared to the 410.4. Interestingly, previous studies also claimed that the more aggressive nature of the 4T1 cell line could lead to disparities in latency versus other breast cancer cell lines after modulation of IL4 signaling (Venmar et al., 2016). In these, glutamine metabolism and enhanced long-term glutamine uptake were associated with IL4-mediated enhanced tumoral growth at the primary site of breast cancer cells, tracing important differences compared to a metastatic context. Improvement of glutamine metabolism has been further related to iron metabolism and ferroptosis induction (Gao et al., 2015), providing clues on future directions for further understanding of the survival advantage derived from the acquisition of a partial E/M state and its associated resistance to ferroptosis. Furthermore, prevention of ferroptotic cell death upon acquisition of mesenchymal properties of epithelial cancer cells has been correlated with a higher reliance on pathways involving GPX4 activity (Viswanathan et al., 2017). Yet, the GPX4 gene expression levels in metastatic tissues derived from 4T1-injected mice were downregulated compared to 410.4-derived metastatic tissues. Interestingly, TUBO-metastatic tissues revealed high expression of both GPX4 and GPX2 compared to the “hot tumor” models-injected tissues, reinforcing the suggestion of higher dependence of epithelial-like cancer cells on GSH synthesis/GPX4 activation to escape ferroptotic cell death during metastatic colonization (Trigueros et al., 2020, submitted).

Additionally, the complexity of ferroptosis is currently a topic of growing interest, and although correct GPX4 functioning is among the most studied anti-ferroptosis delators, it is not the only one. In line with this, mitochondrial activity in cancer cells has been shown to play a crucial role in the induction of ferroptosis through its ability to deprive intracellular cysteine availability, an important component of the antioxidant defense (Gao et al., 2019). Decrease of cysteine has been associated with lower GSH metabolism and increased sensitivity to iron accumulation under stress conditions, which lastly leads to ferroptosis-mediated cell death (Gao et al., 2019). No evidence was found in this study to support a higher tolerance of iron metabolism in the 4T1 model. However, further expression analyses of genes involved in

heme synthesis or intracellular iron retention could be of great interest in addressing the differences between 410.4 and 4T1 model's sensitivity to IL4 signaling disruption and ferroptosis cell death event. In these terms, the sensitivity of the infiltrative "hot tumor" 410.4 model could be linked to particular over-activation of the mitochondria in the absence of a properly functioning IL4. Together, associative studies into the mitochondrial activity and E/M status of BCBM cells may prove to be an interesting perspective to elucidate the true role of ROS, GSH/GPX4, iron metabolism and ferroptosis in the brain-MME.

4.5. IL4 effect in microglia/MDM

According to previous literature and the results presented in this work, IL4 drives the polarization of TAM population within the MME into their invasive phenotype and is therefore identified as a major immunosuppressive component during metastatic colonization. Importantly, TAMs mainly accumulate at the MMPI of infiltrative "hot tumors", where they directly interact with cancer cells resulting in increased invasion capacity (Blazquez et al., 2018) by mechanisms yet incompletely understood. Nevertheless, the involvement of IL4 signaling in cytotoxic ROS management/fitness in breast cancer cells must be a natural consequence of the coexistence of both myeloid populations at the MMPI as a site of maximum scope for interaction. Thus, the strong decrease of 410.4 spheroids outgrowth and marked tolerance of the 4T1 spheroids upon treatment with BSO mirrored the behaviors of both "hot tumor" models against modulation of IL4 signaling *in vivo*. Similarly, the "cold tumor" TUBO model and the 4T1 "hot tumor" model displayed resistance to ROS sensitivity *in vitro*, which correlated with the paucity of significant changes in the mild/null survival advantage observed *in vivo*. According to the reported data, the tumorigenic/metastatic effect of MG/MDM during CNS colonization of the breast cancer cells depends not only on IL4 signaling but also on ROS sensitivity/detoxifying mechanisms of breast cancer cell.

In this work, we argue that the survival effects triggered by IL4/IL4R α signaling axis blockade in 410.4-injected no tumor-bearing KO mice occur due to intracellular signaling in microglia/MDM population comprised at the metastatic niche. Interestingly, *in vitro* measurement of the migration capacity of the macrophage populations in response to tumor-derived supernatants from "hot" or "cold" tumor models reported equal migratory effects on both MDM and MG. Also *in vivo*, the *Iba1* marker revealed a similar infiltration capacity of both myeloid populations in brain metastatic tissues. However, modifications in the metastatic environment that trigger tumor cell progression start with the activation of the innate immune system rather than with adaptive immunity (Blazquez et al., 2018). Thus, despite the failure of our conditional MDM- IL4R α KO model in demonstrating if the absence of IL4 signaling prevents pro-tumor

activities of M2 phenotype-polarized MDMs during BM, it is still fundamental to elucidate the importance of the role of MDM and MG at the metastatic niche separately.

4.6. Future research perspectives

Most current cancer immunotherapy strategies target adaptive immune responses, albeit only 20% of patients undergoing treatment report efficacy (Rameshbabu et al, 2021). Furthermore, the success of ICI is limited to “hot” tumors characterized by preexisting T cell infiltration, consolidating “hot” and “cold” tumor immune phenotypes as entities of prognostic significance (Barnes et al, 2018). Failure to immunotherapy in “hot tumor” models upon ICI treatment is usual in different cancer malignancies including breast cancer, which highlights the need to develop therapeutic approaches driving activation of the innate immune system in terms of tumor immunosurveillance and generation of antitumor immune responses (Rameshbabu et al, 2021). Alternatively, promotion of T cell infiltration in immunologically “cold” tumors emerges as a novel approach of rising interest, since lack of immunogenicity results, at least partially, from orchestrated immunosuppression role of the TAMs comprised in the MME (Beatty et al.,2015).

Since TAMs are purposed to modulate metastatic colonization and outgrowth through local immunosuppression when polarized into their M2-phenotype, re-education of the TAM compartment into its M1 phenotype entails an interesting approach to reprogram the MME toward a more pro-inflammatory environment in order to avoid the colonization of the brain. The use of PI3K (delta) inhibitors and CSF1R as monotherapy, and in combination with chemotherapy and ICI, are some of the agents in clinical development aimed to target innate immunity in cancer (Autio et al, 2019; Kaneda et al, 2016). Importantly, Klemm et al recently demonstrated the efficacy of CSF1R inhibition in including anti-tumor responses of target TAMs at distinct stages of the metastatic cascade. In this study, induction of neuroinflammation in association with wound repair responses was triggered by the macrophage population in preclinical breast-to-brain metastasis models (Klemm et al., 2021). In these terms, given the promising results observed in other investigations, the effect on inhibition of the IL4/IL4R axis in the innate compartment of the brain-MME needs to be further elucidated.

5. Summary and Conclusions

The prognostic value of infiltrative MMPI patterns highlights their relevance as a key target in the battle against brain metastasis. In the attempt to investigate the biological mechanisms that determine the pathophysiology of brain metastatic colonization, different brain metastasis models displaying infiltrative or displacing MMPIs have been used in this study.

The 410.4 and 4T1 cell lines, previously established in our group as brain metastasis models displaying infiltrative MMPI patterns, revealed the moderate and high metastatic potential and were characterized as epithelial and epithelial with mesenchymal-like features, respectively. However, the TUBO cell line has been characterized as highly epithelial and established as a new syngeneic mouse model of brain metastasis with a displacing MMPI pattern. Importantly, although previous work suggested the correlation between non-infiltrative MMPIs and good prognosis, in this study I showed that displacing MMPIs may also display a very high colonization capacity and hence great metastatic potential.

Characterization of the immune response within the brain-MME in the different MMPI models revealed a correlation between MMPI patterns and immune cell infiltration. Infiltrative MMPI models were associated with a greater immune infiltration within the metastatic core together with a pronounced activation of macrophage and astrocyte populations. However, the displacing MMPI model showed severe exclusion of infiltrative T cells and a lower degree of immune cell infiltration, reflecting an immunologically desert metastatic niche. Depending on their degree of immune cell infiltration, tumors were classified as "cold" or "hot". Thus, this work has contributed to the establishment of TUBO as a new "cold tumor" model available for future research. Similarly, the 410.4 and 4T1 models have been established as "hot tumor" models. Collectively, the association of the MMPI patterns with immune infiltration highlights the therapeutic potential of MMPI patterns as a strategy to shape the immune response within the brain-MME.

IL4/IL4R α -signaling blockade impacted immune response activation during colonization of breast cancer cell lines. Particularly, IL4 signaling disruption resulted in a decreased metastatic potential of the infiltrative 410.4 model *in vivo*, with associated prolongation of the survival rate of the mice but no changes in the colonization pattern at the MMPI. Importantly, characterization of the IL4/IL4R α signaling activation in brain-TAMs and breast cancer cell lines confirmed that the immunosuppressive role of IL4 signaling relies on the macrophage compartment of the brain-MME rather than in the tumor entities themselves. Thus, this work has shown that IL4 signaling activation in MG/MDM triggers the immunosuppressive/pro-metastatic role of TAMs during breast cancer colonization of the brain.

Resistance of the infiltrative 4T1 model to IL4R α signaling highlighted the existence of important differences among both “hot tumor” models of brain metastasis, including their E/M plasticity and metabolic flexibility. The sensitivity of the 410.4 model to disruption of IL4 signaling *in vivo* suggested that the immunosuppressive functions of brain-TAMs are particularly impaired in infiltrating metastatic models with a marked epithelial-like feature. Highly divergent metabolic ROS fitness was suggested as a potential immune resistance mechanism among the selected breast cancer brain metastasis model cell lines since their ROS sensitivities mimicked *in vivo* susceptibility to IL4 signaling disruption. Likewise, gene expression signature analysis of metastatic brain tissues revealed significant differences in the expression of ferroptosis-related markers, suggesting a positive correlation between ferroptosis susceptibility and ROS sensitivity upon IL4/IL4R α signaling disruption. Importantly, combined ICI treatment on the infiltrative 4T1 model revealed high resistance to immunotherapy despite strong recruitment of infiltrative T cells in the brain-MME, once more potentially related to its hybrid E/M status. This data suggests the need for further research into the molecular, metabolic, and pathophysiological differences between the cell lines.

Taken together, the data reported in this study suggest that IL4R-signaling in MDM/microglia is crucial for the acquisition of the metastasis-promoting macrophage phenotype during colonization of the brain. Nevertheless, sensitivity to IL4 signaling disruption may be governed not only by the E/M status or type of MMPI pattern displayed by a breast cancer cell line but also by their metabolic flexibility. In summary, the findings of this study might contribute to the generation of new therapies against brain metastasis focused on re-education of the innate immune cells populating the metastatic niche or based on the different pathophysiological characteristics of the MMPI patterns.

	TUBO		410.4		4T1	
IL4R α - disruption	Low sensitivity		Highly sensitive		Resistant	
BSO	Low sensitivity		Highly sensitive		Resistant	
	WT	KO	WT	KO	WT	KO
MMPI	Displacing	Displacing	Infiltrative	Infiltrative	Infiltrative	Infiltrative
Immune response	“Cold tumor”	“Cold tumor”	“Hot tumor”	“Hot tumor”	“Hot tumor”	“Hot tumor”
E/M state	E	E	E	E	E/M	E/M
GPX4	-	-	-	-	-	-
H01	-	-	↓	↑	-	-
Ferroptosis ζ ?	Resistant	Resistant	Resistant	Sensitive ζ ?	Resistant	Resistant

Table 24. Summary of major differences among BCBM mouse models upon IL4/IL4R α signaling disruption.

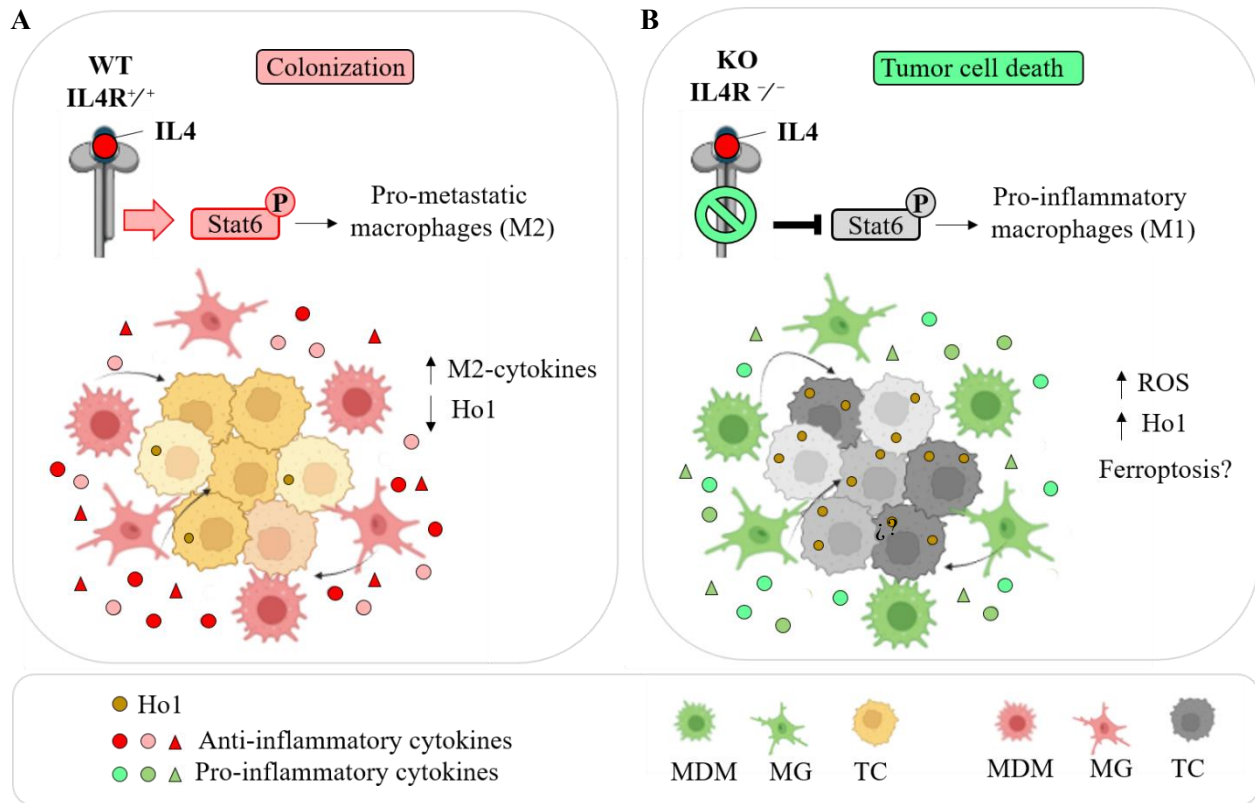


Figure 37. Schematic representation of macrophage phenotypic switch after IL4R α -inhibition. A) The pro-metastatic role of the M2-like microglia/MDM in WT mice (IL4R α ^{+/+}) upon IL4 signaling activation is represented by increased expression of anti-inflammatory cytokines. The interplay between the TAM compartment and the tumor entities within the brain-MME results in improved- colonization of the breast cancer cells during brain metastasis. **B)** The pro-inflammatory role of microglia/MDM polarized into their M1-like phenotype in KO mice (IL4R α ^{-/-}) results in increased expression of inflammatory cytokines. Potentially, the resulting intracellular accumulation of ROS in breast cancer cells and up-regulation of the ferroptosis-related *Ho1* gene could lead to tumor cell death upon disruption of the IL4 signaling, preventing colonization of the brain (*Ho1*, Heme-oxygenase1; MDM, monocyte-derived macrophages; MG, microglia; TC, tumor cell; IL4, interleukin-4, Stat6, signal transducer and activator of transcription factor 6; P, phosphorylation; ROS, reactive oxygen species; WT, wild-type; KO, knock-out).

6. Appendix

6.1. List of Tables

Table 1: Cell lines.....	24
Table 2: Cell culture and additives.....	26
Table 3. Chemicals, enzymes and other reagents.....	26
Table 4: Buffers and solutions.....	27
Table 5: Antibodies and fluorescence dyes.....	29
Table 6: Oligonucleotides.....	30
Table 7: Comercial kits.....	31
Table 8: Consumables.....	32
Table 9: Equipment.....	33
Table 10: Software products and databases.....	34
Table 11: Compesation and antibody FACS staining procedure.....	37
Table 12: Composition of cell culture mediums for MDM isolation.....	39
Table 13: Composition of anesthetic solution and painkiller for stereotactical intracortical injection of tumor cells.....	42
Table 14: Animal scoring after stereotactical intracortical injection.....	43
Table 15: Composition of stacking and resolving gels.....	45
Table 16: Protocol of qRT-PCR program.....	49
Table 17: List of essential components included in the master mix (MM) for the PCR.....	51
Table 18: Protocol of PCR program.....	52
Table 19: Phalloidin staining protocol.....	53
Table 20: Tumor cell spheroids staining protocol.....	54
Table 21: Alcohol concentration series for staining of brain tissue.....	55
Table 22: H-E staining protocol.....	55
Table 23: IHC staining protocols for Cd3, Ck8 and Iba1.....	56
Table 24: IHC staining protocols for Gfap.....	56

6.2. List of Figures

Figure 1. Metastatic brain colonization.....	10
Figure 2. Macro-metastasis/organ parenchyma interface (MMPI) patterns.	13
Figure 3. The cellular environment in the healthy brain and BM.	15
Figure 4. Signaling pathways activated via interleukin 4-receptors (IL4R).....	20
Figure 5. Example of cell count determination using flow cytometer BD FACSCalibur.....	38
Figure 6. Schematics of Hanging Drop assay.....	40
Figure 7. Schematics of Chemotaxis assay.....	41
Figure 8. Characterization of murine breast cancer cell lines.....	60
Figure 9. Morphological characterization of murine breast cancer cell lines.....	62
Figure 10. TUBO breast cancer BM mouse model.	63
Figure 11. Overall survival and colonization index of BCBM mouse models.....	65
Figure 12. Tumor load comparison between the BCBM mouse models	66
Figure 13. MMPI of BCBM mouse models	67
Figure 14. Characterization of MG/MDM populations in the metastatic brain.	69
Figure 15. Characterization of astrocyte population in the metastatic brain	71
Figure 16. Characterization of T cell population in the metastatic brain.....	73
Figure 17. Gene expression signature in the microenvironment of BM: in vitro versus in vivo expression patterns.....	74
Figure 18. Macrophage migration capacity: “cold” versus “hot” tumor models	76
Figure 19. Characterization of IL4 signaling on murine BM model cell lines.....	78
Figure 20. Characterization of IL4 signaling on murine BM model cell lines.....	79
Figure 21. IL4R α -knockout murine model.....	81
Figure 22. Characterization of IL4 signaling on MDM/MG	82
Figure 23. Potential contribution of MDM/MG cytokine profile to the TME.....	83
Figure 24. Analysis of M2-polarization status of MDM/MG.....	84
Figure 25. Effects of IL4-signaling knockout in BCBM mouse models on overall survival and colonization index	86
Figure 26. Effects of IL4-signaling knockout in BCBM mouse models on gene expression.....	87
Figure 27. Effects of IL4-signaling knockout in BCBM mouse models on MMPI	90
Figure 28. Characterization of MG/MDM population in the metastatic brain of IL4R WT and KO mice.....	93
Figure 29	95
Figure 30. Characterization of T cell population in the metastatic brain of IL4 signaling KO mice	97

Figure 31. Effect of ICB therapy in IL4R knockout mice.....	99
Figure 32. Effect of MDM-specific IL4 signaling knockout in 410.4 BM model	101
Figure 33. Gene expression signature in IL4 signaling KO metastatic tissues.....	102
Figure 34. Comparative quantitative RT-PCR analysis of gene expression signature across WT-derived metastatic tissue.....	104
Figure 35. Functional 3D characterization of murine BM model cell lines	105
Figure 36. Effects of BSO in murine BM model cell lines in vitro.....	106
Figure 37. Schematic representation of macrophage phenotypic switch's effect on breast cancer cell lines after IL4R α -disruption.	122

6.3. Abbreviations

ANOVA	analysis of variance
BBB	blood-brain barrier
BBM	blood-brain metastasis barrier
BCBM	breast cancer brain metastasis
BF	bright field
BM	brain metastasis
BMDM	bone marrow-derived macrophages
BSA	bovine serum albumin
BSO	buthionine sulfoximine
Cd3	cluster of differentiation 3
CI	colonization index
Ck19	cytokeratin-19
Ck8	cytokeratin-8
CNS	central nervous system
CSF1R	colony-stimulating factor 1 receptor
CTL	control
CTL4	cytotoxic T-lymphocyte antigen 4
DAB	diaminobenzidine
DAMPs	damage-associated molecular patterns
ddH ₂ O	double-distilled water
DEG	differentially expressed gene
dH ₂ O	distilled water
DMEM	Dulbecco's modified Eagle medium
DMSO	dimethyl sulfoxide
Ecad	E-cadherin
E-cadherin	epithelial cadherin
ECM	extracellular matrix
EDTA	ethylenediaminetetraacetic acid
E/M	epithelial/mesenchymal
EMT	epithelial-mesenchymal transition
EtOH	ethanol
FACS	fluorescence-activated cell sorter
FDA	food and drug administration
FCS	fetal calf serum
FITC	fluorescein isothiocyanate

Gfap	glial fibrillary acidic protein
GOI	gene of interest
GPX4	glutathione peroxidase 4
GSH	glutathione
GSSG	oxidized glutathione
HE	hematoxylin and eosin
HER2+	human epidermal growth factor receptor 2-positive
HK	housekeeping gene ABBREVIATIONS XI
HRP	horseradish peroxidase
HSP90	heat shock protein 90
Iba1	allograft inflammatory factor 1
ICI	immunecheckpoint inhibitor
ICB	immunecheckpoint blockade
IF	immunofluorescence
IHC	immunohistochemistry
IL4	Interleukin 4
IL4R	interleukin 4-receptor
IRS	insulin receptor substrate protein
KO	knockout
LPS	lipopolysaccharide
LysM	lysozyme M
MDMs	monocyte-derived macrophages
MG	microglia
MME	metastatic microenvironment
MMP	modified milk powder
MMPI	macro-metastasis/organ parenchyma interface
M-CSF	macrophage colony-stimulating factor
mRNA	messenger RNA
n.s.	not significant
mTOR	mammalian target of rapamycin
NaCl	sodium chloride
OS	overall survival
PAMPs	pathogen-associated molecular patterns
PFA	paraformaldehyde
PBS	phosphate buffered saline PFA paraformaldehyde
PI3K	phosphoinositide 3-kinase
PD1	programmed death-1

P/S	penicillin/streptomycin
qRT-PCR	quantitative real-time polymerase chain reaction
RNA	ribonucleic acid
ROI	region of interest
ROS	reactive oxygen species
RT	room temperature
SDS	sodium dodecyl sulfate
SDS-PAGE	SDS polyacrylamide gel electrophoresis
Stat6	transducer and activator of transcription factor 6
TAMs	tumor-associated macrophages
TME	tumor microenvironment
TRITC	tetramethylrhodamine
TN	triple negative
Vim	vimentin
WT	wild-type
β -Act	β -Actin
β -Cat	β -catenin

Measurement units

% (v/v) volume per volume
 % (w/v) weight per volume
 bp base pairs
 °C degree Celsius
 g gram
 h hour
 l liter
 m meter
 M Molar
 min minute
 n number
n sample size
 rpm revolutions per minute
 ses second

Metric prefixes

k kilo (10^3)
 c centi (10^{-2})
 m milli (10^{-3})
 μ micro (10^{-6})
 n nano (10^{-9})

7. Bibliography

- Achrol, Achal Singh; Rennert, Robert C.; Anders, Carey; Soffiatti, Riccardo; Ahluwalia, Manmeet S.; Nayak, Lakshmi et al. (2019): Brain metastases. *Nature reviews. Disease primers* 5 (1), p. 5.
- Amit, Moran; Laider-Trejo, Leonor; Shalom, Vardit; Shabtay-Orbach, Ayelet; Krelin, Yakov; Gil, Ziv (2013): Characterization of the melanoma brain metastatic niche in mice and humans. *Cancer medicine* 2 (2), pp. 155–163. DOI: 10.1002/cam4.45.
- Andreou, Kleopatra E.; Soto, Manuel Sarmiento; Allen, Danny; Economopoulos, Vasiliki; Bernardi, Axel de; Larkin, James R.; Sibson, Nicola R. (2017): Anti-inflammatory Microglia/Macrophages As a Potential Therapeutic Target in Brain Metastasis. *Frontiers in oncology* 7, p. 251. DOI: 10.3389/fonc.2017.00251.
- Arvanitis, Costas D.; Ferraro, Gino B.; Jain, Rakesh K. (2020): The blood-brain barrier and blood-tumour barrier in brain tumours and metastases. *Nature reviews. Cancer* 20 (1), pp. 26–41. DOI: 10.1038/s41568-019-0205-x.
- Autio, Karen A.; Klebanoff, Christopher A.; Schaer, David; Kauh, John Sae Wook; Slovin, Susan F.; Adamow, Matthew et al. (2020): Immunomodulatory Activity of a Colony-stimulating Factor-1 Receptor Inhibitor in Patients with Advanced Refractory Breast or Prostate Cancer: A Phase I Study. *Clinical cancer research: an official journal of the American Association for Cancer Research* 26 (21), pp. 5609–5620. DOI: 10.1158/1078-0432.CCR-20-0855.
- Barnes, Tristan A.; Amir, Eitan (2017): HYPE or HOPE: the prognostic value of infiltrating immune cells in cancer. *British journal of cancer* 117 (4), pp. 451–460. DOI: 10.1038/bjc.2017.220.
- Bankaitis, Katherine Venmar; Fingleton, Barbara (2015): Targeting IL4/IL4R for the treatment of epithelial cancer metastasis. *Clinical & experimental metastasis* 32 (8), pp. 847–856. DOI: 10.1007/s10585-015-9747-9.
- Beatty, Gregory L.; Gladney, Whitney L. (2015): Immune escape mechanisms as a guide for cancer immunotherapy. *Clinical cancer research: an official journal of the American Association for Cancer Research* 21 (4), pp. 687–692. DOI: 10.1158/1078-0432.CCR-14-1860.
- Berghoff, Anna S.; Rajky, Orsolya; Winkler, Frank; Bartsch, Rupert; Furtner, Julia; Hainfellner, Johannes A. et al. (2013): Invasion patterns in brain metastases of solid cancers. *Neuro-oncology* 15 (12), pp. 1664–1672. DOI: 10.1093/neuonc/not112.
- Berghoff, Anna S.; Preusser, Matthias (2015): The inflammatory microenvironment in brain metastases: potential treatment target? *Chinese clinical oncology* 4 (2), p. 21. DOI: 10.3978/j.issn.2304-3865.2015.06.03.
- Berghoff, Anna S.; Schur, Sophie; Füreder, Lisa M.; Gatterbauer, Brigitte; Dieckmann, Karin; Widhalm, Georg et al. (2016): Descriptive statistical analysis of a real life cohort of 2419 patients with brain metastases of solid cancers. *ESMO open* 1 (2), e000024. DOI: 10.1136/esmoopen-2015-000024.
- Blazquez, R.; Sparrer, D.; Wendl, C.; Evert, M.; Riemenschneider, M. J.; Krahn, M. P. et al. (2020): The macro-metastasis/organ parenchyma interface (MMPI) - A hitherto unnoticed area. *Seminars in cancer biology* 60, pp. 324–333. DOI: 10.1016/j.semcancer.2019.10.012.
- Blazquez, Raquel; Rietkötter, Eva; Wenske, Britta; Wlochowitz, Darius; Sparrer, Daniela; Vollmer, Elena et al. (2020): LEF1 supports metastatic brain colonization by regulating glutathione metabolism and increasing ROS resistance in breast cancer. *International journal of cancer* 146 (11), pp. 3170–3183. DOI: 10.1002/ijc.32742.
- Blazquez, Raquel; Wlochowitz, Darius; Wolff, Alexander; Seitz, Stefanie; Wachter, Astrid; Perera-Bel, Julia et al. (2018): PI3K: A master regulator of brain metastasis-promoting macrophages/microglia. *Glia* 66 (11), pp. 2438–2455. DOI: 10.1002/glia.23485.
- Bonaventura, Paola; Shekarian, Tala; Alcazer, Vincent; Valladeau-Guilemond, Jenny; Valsesia-Wittmann, Sandrine; Amigorena, Sebastian et al. (2019): Cold Tumors: A Therapeutic Challenge for Immunotherapy. *Frontiers in immunology* 10, p. 168. DOI: 10.3389/fimmu.2019.00168.

- Bowman, Robert L.; Klemm, Florian; Akkari, Leila; Pyonteck, Stephanie M.; Sevenich, Lisa; Quail, Daniela F. et al. (2016): Macrophage Ontogeny Underlies Differences in Tumor-Specific Education in Brain Malignancies. *Cell reports* 17 (9), pp. 2445–2459. DOI: 10.1016/j.celrep.2016.10.052.
- Byers, Lauren Averett; Diao, Lixia; Wang, Jing; Saintigny, Pierre; Girard, Luc; Peyton, Michael et al. (2013): An epithelial-mesenchymal transition gene signature predicts resistance to EGFR and PI3K inhibitors and identifies Axl as a therapeutic target for overcoming EGFR inhibitor resistance. *Clinical cancer research: an official journal of the American Association for Cancer Research* 19 (1), pp. 279–290. DOI: 10.1158/1078-0432.CCR-12-1558.
- Chatila, Talal A. (2004): Interleukin-4 receptor signaling pathways in asthma pathogenesis. *Trends in molecular medicine* 10 (10), pp. 493–499. DOI: 10.1016/j.molmed.2004.08.004.
- Charles, Nikki A.; Holland, Eric C.; Gilbertson, Richard; Glass, Rainer; Kettenmann, Helmut (2011): The brain tumor microenvironment. *Glia* 59 (8), pp. 1169–1180. DOI: 10.1002/glia.21136.
- Chen, Daniel S.; Mellman, Ira (2017): Elements of cancer immunity and the cancer-immune set point. *Nature* 541 (7637), pp. 321–330. DOI: 10.1038/nature21349.
- Chen, Jiaoe; Gong, Chaoju; Mao, Huiqin; Li, Zhaoyun; Fang, Zejun; Chen, Qiang et al. (2018): E2F1/SP3/STAT6 axis is required for IL-4-induced epithelial-mesenchymal transition of colorectal cancer cells. *International journal of oncology* 53 (2), pp. 567–578. DOI: 10.3892/ijo.2018.4429.
- Chen, Jinyu; Lee, Ho-Jeong; Wu, Xuefeng; Huo, Lei; Kim, Sun-Jin; Xu, Lei et al. (2015): Gain of glucose-independent growth upon metastasis of breast cancer cells to the brain. *Cancer research* 75 (3), pp. 554–565. DOI: 10.1158/0008-5472.CAN-14-2268.
- Chiricozzi, Andrea; Maurelli, Martina; Peris, Ketty; Girolomoni, Giampiero (2020): Targeting IL-4 for the Treatment of Atopic Dermatitis. *ImmunoTargets and therapy* 9, pp. 151–156. DOI: 10.2147/ITT.S260370.
- Chuang, Han-Ning; van Rossum, Denise; Sieger, Dirk; Siam, Laila; Klemm, Florian; Bleckmann, Annalen et al. (2013): Carcinoma cells misuse the host tissue damage response to invade the brain. *Glia* 61 (8), pp. 1331–1346. DOI: 10.1002/glia.22518.
- Condeelis, John; Pollard, Jeffrey W. (2006): Macrophages: obligate partners for tumor cell migration, invasion, and metastasis. *Cell* 124 (2), pp. 263–266. DOI: 10.1016/j.cell.2006.01.007.
- Cordero, Alex; Kanojia, Deepak; Miska, Jason; Panek, Wojciech K.; Xiao, Annie; Han, Yu et al. (2019): FABP7 is a key metabolic regulator in HER2+ breast cancer brain metastasis. *Oncogene* 38 (37), pp. 6445–6460. DOI: 10.1038/s41388-019-0893-4.
- Cotechini, Tiziana; Atallah, Aline; Grossman, Arielle (2021): Tissue-Resident and Recruited Macrophages in Primary Tumor and Metastatic Microenvironments: Potential Targets in Cancer Therapy. *Cells* 10 (4). DOI: 10.3390/cells10040960.
- De, Ishani; Nikodemova, Maria; Steffen, Megan D.; Sokn, Emily; Maklakova, Vilena I.; Watters, Jyoti J.; Collier, Lara S. (2014): CSF1 overexpression has pleiotropic effects on microglia in vivo. *Glia* 62 (12), pp. 1955–1967. DOI: 10.1002/glia.22717.
- DeNardo, David G.; Barreto, Jairo B.; Andreu, Pauline; Vasquez, Lesley; Tawfik, David; Kolhatkar, Nikita; Coussens, Lisa M. (2009): CD4(+) T cells regulate pulmonary metastasis of mammary carcinomas by enhancing protumor properties of macrophages. *Cancer cell* 16 (2), pp. 91–102. DOI: 10.1016/j.ccr.2009.06.018.
- Dixon, Scott J.; Lemberg, Kathryn M.; Lamprecht, Michael R.; Skouta, Rachid; Zaitsev, Eleina M.; Gleason, Caroline E. et al. (2012): Ferroptosis: an iron-dependent form of nonapoptotic cell death. *Cell* 149 (5), pp. 1060–1072. DOI: 10.1016/j.cell.2012.03.042.
- Doron, Hila; Pukrop, Tobias; Erez, Neta (2019): A Blazing Landscape: Neuroinflammation Shapes Brain Metastasis. *Cancer research* 79 (3), pp. 423–436. DOI: 10.1158/0008-5472.CAN-18-1805.

- Emeline Tabouret, Olivier Chinot, Philippe Metellus, Agnès Tallet, Patrice Viens, Anthony Gonçalves (2012). Recent trends in epidemiology of brain metastases: an overview. *Anticancer Res.* Nov;32 (11):4655-62.
- Erblich, Bryna; Zhu, Liyin; Etgen, Anne M.; Dobrenis, Kostantin; Pollard, Jeffrey W. (2011): Absence of colony stimulation factor-1 receptor results in loss of microglia, disrupted brain development and olfactory deficits. *PLoS one* 6 (10), e26317. DOI: 10.1371/journal.pone.0026317.
- Erez, Neta; Coussens, Lisa M. (2011): Leukocytes as paracrine regulators of metastasis and determinants of organ-specific colonization. *International journal of cancer* 128 (11), pp. 2536–2544. DOI: 10.1002/ijc.26032.
- Fitzgerald, Daniel P.; Palmieri, Diane; Hua, Emily; Hargrave, Elizabeth; Herring, Jeanne M.; Qian, Yongzhen et al. (2008): Reactive glia are recruited by highly proliferative brain metastases of breast cancer and promote tumor cell colonization. *Clinical & experimental metastasis* 25 (7), pp. 799–810. DOI: 10.1007/s10585-008-9193-z.
- Fidler, I. J. (1970). Metastasis: Quantitative Analysis of Distribution and Fate of Tumor Emboli Labeled With 125I-5-Iodo-2'-deoxyuridine. *JNCI: Journal of the National Cancer Institute*, 45(4), 773-782. DOI:10.1093/jnci/45.4.773
- Friedl, Peter; Alexander, Stephanie (2011): Cancer invasion and the microenvironment: plasticity and reciprocity. *Cell* 147 (5), pp. 992–1009. DOI: 10.1016/j.cell.2011.11.016.
- Gadani, Sachin P.; Cronk, James C.; Norris, Geoffrey T.; Kipnis, Jonathan (2012): IL-4 in the brain: a cytokine to remember. *Journal of immunology* (Baltimore, Md: 1950) 189 (9), pp. 4213–4219. DOI: 10.4049/jimmunol.1202246.
- Germain, Nicolas; Dhayer, Mélanie; Boileau, Marie; Fovez, Quentin; Kluza, Jerome; Marchetti, Philippe (2020): Lipid Metabolism and Resistance to Anticancer Treatment. *Biology* 9 (12). DOI: 10.3390/biology9120474.
- Gomez Perdiguero, Elisa; Klapproth, Kay; Schulz, Christian; Busch, Katrin; Azzoni, Emanuele; Crozet, Lucile et al. (2015): Tissue-resident macrophages originate from yolk-sac-derived erythro-myeloid progenitors. *Nature* 518 (7540), pp. 547–551. DOI: 10.1038/nature13989.
- Gordon, Siamon; Martinez, Fernando O. (2010): Alternative activation of macrophages: mechanism and functions. *Immunity* 32 (5), pp. 593–604. DOI: 10.1016/j.immuni.2010.05.007.
- Hallett, Miranda A.; Venmar, Katherine T.; Fingleton, Barbara (2012): Cytokine stimulation of epithelial cancer cells: the similar and divergent functions of IL-4 and IL-13. *Cancer research* 72 (24), pp. 6338–6343. DOI: 10.1158/0008-5472.CAN-12-3544.
- Hanahan, Douglas; Weinberg, Robert A. (2011): Hallmarks of cancer: the next generation. *Cell* 144 (5), pp. 646–674. DOI: 10.1016/j.cell.2011.02.013.
- Hangauer, Matthew J.; Viswanathan, Vasanthi S.; Ryan, Matthew J.; Bole, Dhruv; Eaton, John K.; Matov, Alexandre et al. (2017): Drug-tolerant persister cancer cells are vulnerable to GPX4 inhibition. *Nature* 551 (7679), pp. 247–250. DOI: 10.1038/nature24297.
- He, Bei Ping; Wang, Jian Jun; Zhang, Xian; Wu, Yan; Wang, Miao; Bay, Boon-Huat; Chang, Alex Yuang-Chi (2006): Differential reactions of microglia to brain metastasis of lung cancer. *Molecular medicine* (Cambridge, Mass.) 12 (7-8), pp. 161–170. DOI: 10.2119/2006-00033.He.
- Hendriks, Lizza E. L.; Henon, Clemence; Auclin, Edouard; Mezquita, Laura; Ferrara, Roberto; Audigier-Valette, Clarisse et al. (2019): Outcome of Patients with Non-Small Cell Lung Cancer and Brain Metastases Treated with Checkpoint Inhibitors. *Journal of thoracic oncology: official publication of the International Association for the Study of Lung Cancer* 14 (7), pp. 1244–1254. DOI: 10.1016/j.jtho.2019.02.009.
- Heppner G. H. (1984): Tumor heterogeneity. *Cancer Res.* 1984;44:2259-2265.
- Hosseini, Hedayatollah; Obradović, Milan M. S.; Hoffmann, Martin; Harper, Kathryn L.; Sosa, Maria Soledad; Werner-Klein, Melanie et al. (2016): Early dissemination seeds metastasis in breast cancer. *Nature* 540 (7634), pp. 552–558. DOI: 10.1038/nature20785.

Ito, Shuku-Ei; Shiota, Hidekazu; Kasahara, Yuki; Saijo, Ken; Ishioka, Chikashi (2017): IL-4 blockade alters the tumor microenvironment and augments the response to cancer immunotherapy in a mouse model. *Cancer immunology, immunotherapy: CII* 66 (11), pp. 1485–1496. DOI: 10.1007/s00262-017-2043-6.

Kaneda, Megan M.; Messer, Karen S.; Ralainirina, Natacha; Li, Hongying; Leem, Christopher J.; Gorjestani, Sara et al. (2016): PI3K γ is a molecular switch that controls immune suppression. *Nature* 539 (7629), pp. 437–442. DOI: 10.1038/nature19834.

Kim, Hyeonhui; Kim, Minki; Im, Sun-Kyoung; Fang, Sungsoo (2018): Mouse Cre-LoxP system: general principles to determine tissue-specific roles of target genes. *Laboratory animal research* 34 (4), pp. 147–159. DOI: 10.5625/lar.2018.34.4.147.

Kim, Yi-Jun; Kim, Jae-Sung; Kim, In Ah (2018): Molecular subtype predicts incidence and prognosis of brain metastasis from breast cancer in SEER database. *Journal of cancer research and clinical oncology* 144 (9), pp. 1803–1816. DOI: 10.1007/s00432-018-2697-2.

Klemm, Florian; Maas, Roeltje R.; Bowman, Robert L.; Kornete, Mara; Soukup, Klara; Nassiri, Sina et al. (2020): Interrogation of the Microenvironmental Landscape in Brain Tumors Reveals Disease-Specific Alterations of Immune Cells. *Cell* 181 (7), 1643-1660.e17. DOI: 10.1016/j.cell.2020.05.007.

Klemm, Florian; Schäffer, Alexander; Salamero-Boix, Anna; Alekseeva, Tijna; Schulz, Michael; Niesel, Katja et al. (2021): Compensatory CSF2-driven macrophage activation promotes adaptive resistance to CSF1R inhibition in breast-to-brain metastasis.

Kotecki, Nuria; Lefranc, Florence; Devriendt, Daniel; Awada, Ahmad (2018): Therapy of breast cancer brain metastases: challenges, emerging treatments and perspectives. *Therapeutic advances in medical oncology* 10, 1758835918780312. DOI: 10.1177/1758835918780312.

Lambert, Arthur W.; Pattabiraman, Diwakar R.; Weinberg, Robert A. (2017): Emerging Biological Principles of Metastasis. *Cell* 168 (4), pp. 670–691. DOI: 10.1016/j.cell.2016.11.037.

Leland, P.; Taguchi, J.; Husain, S. R.; Kreitman, R. J.; Pastan, I.; Puri, R. K. (2000): Human Breast Carcinoma Cells Express Type II IL-4 Receptors and Are Sensitive to Antitumor Activity of a Chimeric IL-4-Pseudomonas Exotoxin Fusion Protein in vitro and in vivo. *Mol Med* 6 (3), pp. 165–178. DOI: 10.1007/BF03402112.

Li, Ben Hui; Yang, Xian Zi; Li, Pin Dong; Yuan, Qin; Liu, Xiao Hong; Yuan, Jia; Zhang, Wen Jie (2008): IL-4/Stat6 activities correlate with apoptosis and metastasis in colon cancer cells. *Biochemical and biophysical research communications* 369 (2), pp. 554–560. DOI: 10.1016/j.bbrc.2008.02.052.

Li, Jie; Cao, Feng; Yin, He-Liang; Huang, Zi-Jian; Lin, Zhi-Tao; Mao, Ning et al. (2020): Ferroptosis: past, present and future. *Cell death & disease* 11 (2), p. 88. DOI: 10.1038/s41419-020-2298-2.

Li, Zhan; Yin, Songcheng; Zhang, Lei; Liu, Weiguang; Chen, Bo (2017): Prognostic value of reduced E-cadherin expression in breast cancer: a meta-analysis. *Oncotarget* 8 (10), pp. 16445–16455. DOI: 10.18632/oncotarget.14860.

Lin, E. Y.; Nguyen, A. V.; Russell, R. G.; Pollard, J. W. (2001): Colony-stimulating factor 1 promotes progression of mammary tumors to malignancy. *The Journal of experimental medicine* 193 (6), pp. 727–740. DOI: 10.1084/jem.193.6.727.

Liu, Baoyi; Zhang, Xin (2021): Metabolic Reprogramming Underlying Brain Metastasis of Breast Cancer. *Frontiers in molecular biosciences* 8, p. 791927. DOI: 10.3389/fmolb.2021.791927.

Liu, Yuan-Tong; Sun, Zhi-Jun (2021): Turning cold tumors into hot tumors by improving T-cell infiltration. *Theranostics* 11 (11), pp. 5365–5386. DOI: 10.7150/thno.58390.

Long, Georgina V.; Atkinson, Victoria; Lo, Serigne; Sandhu, Shahneen; Guminski, Alexander D.; Brown, Michael P. et al. (2018): Combination nivolumab and ipilimumab or nivolumab alone in melanoma brain metastases: a multicentre randomised phase 2 study. *The Lancet Oncology* 19 (5), pp. 672–681. DOI: 10.1016/S1470-2045(18)30139-6.

- Lowry, Oliver H.; Rosebrough, Nira J.; Farr, A. Lewis; Randall, Rose J. (1951): PROTEIN MEASUREMENT WITH THE FOLIN PHENOL REAGENT. *Journal of Biological Chemistry* 193 (1), pp. 265–275. DOI: 10.1016/S0021-9258(19)52451-6.
- Maria C. Villacres and Cornelia C. Bergmann (1999): Enhanced Cytotoxic T Cell Activity in IL-4-Deficient Mice. *The Journal of Immunology*. Online ISSN: 1550-6606.
- Martin, Allison M.; Cagney, Daniel N.; Catalano, Paul J.; Warren, Laura E.; Bellon, Jennifer R.; Punglia, Rina S. et al. (2017): Brain Metastases in Newly Diagnosed Breast Cancer: A Population-Based Study. *JAMA oncology* 3 (8), pp. 1069–1077. DOI: 10.1001/jamaoncol.2017.0001.
- Maureen Howard, John Farrar, Mary Hilfiker, Barbara Johnson, Kiyosi Takatsu, Toshiyuki Hakamaoka; William E. Pail (1982): Identification of a T-cell derived B cell growth factor distinct from interleukin 2. *J. Exp. MED.* The Rockefeller University Press, Volume 155.
- McCormick, Sarah M.; Heller, Nicola M. (2015): Commentary: IL-4 and IL-13 receptors and signaling. *Cytokine* 75 (1), pp. 38–50. DOI: 10.1016/j.cyto.2015.05.023.
- Minghui Gao, Junmei Yi, Jiajun Zhu, Alexander M. Minikes, Prashant Monian, Craig B. Thompson, Xuejun Jiang (2019). Role of Mitochondria in Ferroptosis. *Molecular Cell* 73, 354–363.
- Mohrs, M., Ledermann, B., Kohler, G., Dorfmueller, A., Gessner, A., and Brombacher, F. (1999). Differences between IL-4- and IL-4 receptor alpha-deficient mice in chronic leishmaniasis reveal a protective role for IL-13 receptor signaling. *Journal of immunology* 162, 7302-7308.
- Moravan, Michael J.; Fecci, Peter E.; Anders, Carey K.; Clarke, Jeffrey M.; Salama, April K. S.; Adamson, Justus D. et al. (2020): Current multidisciplinary management of brain metastases. *Cancer* 126 (7), pp. 1390–1406. DOI: 10.1002/cncr.32714.
- Mueller, Thomas D.; Zhang, Jin-Li; Sebald, Walter; Duschl, Albert (2002): Structure, binding, and antagonists in the IL-4/IL-13 receptor system. *Biochimica et Biophysica Acta (BBA) - Molecular Cell Research* 1592 (3), pp. 237–250. DOI: 10.1016/S0167-4889(02)00318-X.
- Nelms, K.; Keegan, A. D.; Zamorano, J.; Ryan, J. J.; Paul, W. E. (1999): The IL-4 receptor: signaling mechanisms and biologic functions. *Annual review of immunology* 17, pp. 701–738. DOI: 10.1146/annurev.immunol.17.1.701.
- Negrini, Simona; Gorgoulis, Vassilis G.; Halazonetis, Thanos D. (2010): Genomic instability--an evolving hallmark of cancer. *Nature reviews. Molecular cell biology* 11 (3), pp. 220–228. DOI: 10.1038/nrm2858.
- Ngiow, Shin Foong; Young, Arabella (2020): Re-education of the Tumor Microenvironment with Targeted Therapies and Immunotherapies. *Frontiers in immunology* 11, p. 1633. DOI: 10.3389/fimmu.2020.01633.
- Nguyen, Don X.; Bos, Paula D.; Massagué, Joan (2009): Metastasis: from dissemination to organ-specific colonization. *Nature reviews. Cancer* 9 (4), pp. 274–284. DOI: 10.1038/nrc2622.
- Nielsen, Sebastian R.; Schmid, Michael C. (2017): Macrophages as Key Drivers of Cancer Progression and Metastasis. *Mediators of inflammation* 2017, p. 9624760. DOI: 10.1155/2017/9624760.
- Nowell, P. C. (1976): The clonal evolution of tumor cell populations. *Science (New York, N.Y.)* 194 (4260), pp. 23–28. DOI: 10.1126/science.959840.
- Orihuela, Ruben; McPherson, Christopher A.; Harry, Gaylia Jean (2016): Microglial M1/M2 polarization and metabolic states. *British journal of pharmacology* 173 (4), pp. 649–665. DOI: 10.1111/bph.13139.
- Peterson, G. L. (1979). Review of the Folin phenol protein quantitation method of Lowry, Rosebrough, Farr and Randall. *Anal Biochem*, 100(2), 201-220.
- Platten, Michael; Ochs, Katharina; Lemke, Dieter; Opitz, Christiane; Wick, Wolfgang (2014): Microenvironmental clues for glioma immunotherapy. *Current neurology and neuroscience reports* 14 (4), p. 440. DOI: 10.1007/s11910-014-0440-1.

- Pukrop, T.; Klemm, F.; Hagemann, Th; Gradl, D.; Schulz, M.; Siemes, S. et al. (2006): Wnt 5a signaling is critical for macrophage-induced invasion of breast cancer cell lines. *Proceedings of the National Academy of Sciences of the United States of America* 103 (14), pp. 5454–5459. DOI: 10.1073/pnas.0509703103.
- Pukrop, Tobias; Dehghani, Faramarz; Chuang, Han-Ning; Lohaus, Raphaela; Bayanga, Kathrin; Heermann, Stephan et al. (2010): Microglia promote colonization of brain tissue by breast cancer cells in a Wnt-dependent way. *Glia* 58 (12), pp. 1477–1489. DOI: 10.1002/glia.21022.
- Quail, Daniela F.; Joyce, Johanna A. (2017): The Microenvironmental Landscape of Brain Tumors. *Cancer cell* 31 (3), pp. 326–341. DOI: 10.1016/j.ccell.2017.02.009.
- Quail, D. F., & Joyce, J. A. (2013). Microenvironmental regulation of tumor progression and metastasis. *Nat Med*, 19(11), 1423-1437. DOI:10.1038/nm.3394
- Rameshbabu, Srikrishnan; Labadie, Brian W.; Argulian, Anna; Patnaik, Akash (2021): Targeting Innate Immunity in Cancer Therapy. *Vaccines* 9 (2). DOI: 10.3390/vaccines9020138.
- Reiling, N.; Klug, K.; Krallmann-Wenzel, U.; Laves, R.; Goyert, S.; Taylor, M. E. et al. (2001): Complex encounters at the macrophage-mycobacterium interface: studies on the role of the mannose receptor and CD14 in experimental infection models with *Mycobacterium avium*. *Immunobiology* 204 (5), pp. 558–571. DOI: 10.1078/0171-2985-00093.
- Rietkötter, Eva; Menck, Kerstin; Bleckmann, Annalen; Farhat, Katja; Schaffrinski, Meike; Schulz, Matthias et al. (2013): Zoledronic acid inhibits macrophage/microglia-assisted breast cancer cell invasion. *Oncotarget* 4 (9), pp. 1449–1460. DOI: 10.18632/oncotarget.1201.
- Rostami, Rezvan; Mittal, Shivam; Rostami, Pooya; Tavassoli, Fattaneh; Jabbari, Bahman (2016): Brain metastasis in breast cancer: a comprehensive literature review. *Journal of neuro-oncology* 127 (3), pp. 407–414. DOI: 10.1007/s11060-016-2075-3.
- Rovero, S.; Amici, A.; Di Carlo, E.; Bei, R.; Nanni, P.; Quaglino, E. et al. (2000): DNA vaccination against rat her-2/Neu p185 more effectively inhibits carcinogenesis than transplantable carcinomas in transgenic BALB/c mice. *Journal of immunology* (Baltimore, Md.: 1950) 165 (9), pp. 5133–5142. DOI: 10.4049/jimmunol.165.9.5133.
- Ruffell, Brian; Coussens, Lisa M. (2015): Macrophages and therapeutic resistance in cancer. *Cancer cell* 27 (4), pp. 462–472. DOI: 10.1016/j.ccell.2015.02.015.
- Saitoh, Masao (2018): Involvement of partial EMT in cancer progression. *Journal of biochemistry* 164 (4), pp. 257–264. DOI: 10.1093/jb/mvy047.
- Santarpia, Mariacarmela; Karachaliou, Niki (2015): Tumor immune microenvironment characterization and response to anti-PD-1 therapy. *Cancer biology & medicine* 12 (2), pp. 74–78. DOI: 10.7497/j.issn.2095-3941.2015.0022.
- Schild, Tanya; Low, Vivien; Blenis, John; Gomes, Ana P. (2018): Unique Metabolic Adaptations Dictate Distal Organ-Specific Metastatic Colonization. *Cancer cell* 33 (3), pp. 347–354. DOI: 10.1016/j.ccell.2018.02.001.
- Schulz, Michael; Sevenich, Lisa (2021): TAMs in Brain Metastasis: Molecular Signatures in Mouse and Man. *Frontiers in immunology* 12, p. 716504. DOI: 10.3389/fimmu.2021.716504.
- Seidel, Judith A.; Otsuka, Atsushi; Kabashima, Kenji (2018): Anti-PD-1 and Anti-CTLA-4 Therapies in Cancer: Mechanisms of Action, Efficacy, and Limitations. *Frontiers in oncology* 8, p. 86. DOI: 10.3389/fonc.2018.00086.
- Shaul, Yoav D.; Freinkman, Elizaveta; Comb, William C.; Cantor, Jason R.; Tam, Wai Leong; Thiru, Prathapan et al. (2014): Dihydropyrimidine accumulation is required for the epithelial-mesenchymal transition. *Cell* 158 (5), pp. 1094–1109. DOI: 10.1016/j.cell.2014.07.032.
- Shi, Chao; Pamer, Eric G. (2011): Monocyte recruitment during infection and inflammation. *Nature reviews. Immunology* 11 (11), pp. 762–774. DOI: 10.1038/nri3070.
- Shiao, Stephen L.; Ruffell, Brian; DeNardo, David G.; Faddegon, Bruce A.; Park, Catherine C.; Coussens, Lisa M. (2015): TH2-Polarized CD4(+) T Cells and Macrophages Limit Efficacy of Radiotherapy. *Cancer immunology research* 3 (5), pp. 518–525. DOI: 10.1158/2326-6066.CIR-14-0232.

- Siam, Laila; Bleckmann, Annalen; Chaung, Han-Ning; Mohr, Alexander; Klemm, Florian; Barrantes-Freer, Alonso et al. (2015): The metastatic infiltration at the metastasis/brain parenchyma-interface is very heterogeneous and has a significant impact on survival in a prospective study. *Oncotarget* 6 (30), pp.29254–29267. DOI: 10.18632/oncotarget.4201.
- Surana, Rishi; Wang, Shangzi; Xu, Wei; Jablonski, Sandra A.; Weiner, Louis M. (2014): IL4 limits the efficacy of tumor-targeted antibody therapy in a murine model. *Cancer immunology research* 2 (11), pp. 1103–1112. DOI: 10.1158/2326-6066.CIR-14-0103.
- Todaro, M.; Lombardo, Y.; Francipane, M. G.; Alea, M. Perez; Cammareri, P.; Iovino, F. et al. (2008): Apoptosis resistance in epithelial tumors is mediated by tumor-cell-derived interleukin-4. *Cell death and differentiation* 15 (4), pp. 762–772. DOI: 10.1038/sj.cdd.4402305.
- Topalian, Suzanne L.; Drake, Charles G.; Pardoll, Drew M. (2015): Immune checkpoint blockade: a common denominator approach to cancer therapy. *Cancer cell* 27 (4), pp. 450–461. DOI: 10.1016/j.ccell.2015.03.001.
- Valiente, Manuel; Ahluwalia, Manmeet S.; Boire, Adrienne; Brastianos, Priscilla K.; Goldberg, Sarah B.; Lee, Eudocia Q. et al. (2018): The Evolving Landscape of Brain Metastasis. *Trends in cancer* 4 (3), pp. 176–196. DOI: 10.1016/j.trecan.2018.01.003.
- Vanharanta, Sakari; Massagué, Joan (2013): Origins of metastatic traits. *Cancer cell* 24 (4), pp. 410–421. DOI: 10.1016/j.ccr.2013.09.007.
- Venkatesan, Subramanian; Swanton, Charles (2016): Tumor Evolutionary Principles: How Intratumor Heterogeneity Influences Cancer Treatment and Outcome. *American Society of Clinical Oncology educational book*. American Society of Clinical Oncology. Annual Meeting 35, e141-9. DOI: 10.1200/EDBK_158930.
- Venmar, Katherine T.; Carter, Kathy J.; Hwang, Daniel G.; Dozier, E. Ashley; Fingleton, Barbara (2014): IL4 receptor ILR4 α regulates metastatic colonization by mammary tumors through multiple signaling pathways. *Cancer research* 74 (16), pp. 4329–4340. DOI: 10.1158/0008-5472.CAN-14-0093.
- Venmar, Katherine T.; Carter, Kathy J.; Hwang, Daniel G.; Dozier, E. Ashley; Fingleton, Barbara (2014): IL4 receptor ILR4 α regulates metastatic colonization by mammary tumors through multiple signaling pathways. *Cancer research* 74 (16), pp. 4329–4340. DOI: 10.1158/0008-5472.CAN-14-0093.
- Venmar, Katherine T.; Fingleton, Barbara (2014): Lessons from immunology: IL4R directly promotes mammary tumor metastasis. *Oncimmunology* 3 (9), e955373. DOI: 10.4161/21624011.2014.955373.
- Venmar, Katherine T.; Kimmel, Danielle W.; Cliffl, David E.; Fingleton, Barbara (2015): IL4 receptor α mediates enhanced glucose and glutamine metabolism to support breast cancer growth. *Biochimica et biophysica acta* 1853 (5), pp. 1219–1228. DOI: 10.1016/j.bbamcr.2015.02.020.
- Viswanathan, Vasanthi S.; Ryan, Matthew J.; Dhruv, Harshil D.; Gill, Shubhroz; Eichhoff, Ossia M.; Seashore-Ludlow, Brinton et al. (2017): Dependency of a therapy-resistant state of cancer cells on a lipid peroxidase pathway. *Nature* 547 (7664), pp. 453–457. DOI: 10.1038/nature23007.
- Vriens, Kim; Christen, Stefan; Parik, Sweta; Broekaert, Dorien; Yoshinaga, Kazuaki; Talebi, Ali et al. (2019): Evidence for an alternative fatty acid desaturation pathway increasing cancer plasticity. *Nature* 566 (7744), pp. 403–406. DOI: 10.1038/s41586-019-0904-1.
- Wong, Sonia How Ming; Fang, Chee Mun; Chuah, Lay-Hong; Leong, Chee Onn; Ngai, Siew Ching (2018): E-cadherin: Its dysregulation in carcinogenesis and clinical implications. *Critical reviews in oncology/hematology* 121, pp. 11–22. DOI: 10.1016/j.critrevonc.2017.11.010.
- Wu, Jiao; Minikes, Alexander M.; Gao, Minghui; Bian, Huijie; Li, Yong; Stockwell, Brent R. et al. (2019): Intercellular interaction dictates cancer cell ferroptosis via NF2-YAP signalling. *Nature* 572 (7769), pp. 402–406. DOI: 10.1038/s41586-019-1426-6.
- Wu, Shih-Ying; Watabe, Kounosuke (2017): The roles of microglia/macrophages in tumor progression of brain cancer and metastatic disease. *Frontiers in bioscience (Landmark edition)* 22 (10), pp. 1805–1829. DOI: 10.2741/4573.

Xing, Fei; Kobayashi, Aya; Okuda, Hiroshi; Watabe, Misako; Pai, Sudha K.; Pandey, Puspa R. et al. (2013): Reactive astrocytes promote the metastatic growth of breast cancer stem-like cells by activating Notch signalling in brain. *EMBO molecular medicine* 5 (3), pp. 384–396. DOI: 10.1002/emmm.201201623.

Yang, Jing; Antin, Parker; Berx, Geert; Blanpain, Cédric; Brabletz, Thomas; Bronner, Marianne et al. (2020): Guidelines and definitions for research on epithelial-mesenchymal transition. *Nature reviews. Molecular cell biology* 21 (6), pp. 341–352. DOI: 10.1038/s41580-020-0237-9.

Yang, Sen; Ouyang, Jing; Lu, Yanqiu; Harypursat, Vijay; Chen, Yaokai (2022): A Dual Role of Heme Oxygenase-1 in Tuberculosis. *Frontiers in immunology* 13, p. 842858. DOI: 10.3389/fimmu.2022.842858.

Yates, Lucy R.; Gerstung, Moritz; Knappskog, Stian; Desmedt, Christine; Gudem, Gunes; van Loo, Peter et al. (2015): Subclonal diversification of primary breast cancer revealed by multiregion sequencing. *Nature medicine* 21 (7), pp. 751–759. DOI: 10.1038/nm.3886.

You, Hua; Baluszek, Szymon; Kaminska, Bozena (2019): Immune Microenvironment of Brain Metastases-Are Microglia and Other Brain Macrophages Little Helpers? *Frontiers in immunology* 10, p. 1941. DOI: 10.3389/fimmu.2019.01941.

Zhang, Qiong-wen; Liu, Lei; Gong, Chang-yang; Shi, Hua-shan; Zeng, Yun-hui; Wang, Xiao-ze et al. (2012): Prognostic significance of tumor-associated macrophages in solid tumor: a meta-analysis of the literature. *PloS one* 7 (12), e50946. DOI: 10.1371/journal.pone.0050946.

8. Acknowledgements

I would like to thank all the people who paved the way for me at some point, both professionally and emotionally. This work would not have been possible without the reciprocal support of a resilient social network.

An die Laborpartner, die am Anfang dabei waren (Daniela, Julia, Elli), die die Zentren durchlaufen haben (Hannah, Caro) und an diejenigen, die am Ende angekommen sind (Cristoph, Jessica). Ich danke euch allen, dass ihr Teil dieses intensiven vierjährigen Abenteuers gewesen seid und es erträglicher gemacht habt. I cannot forget my dear fellow PhD students Elena, Asmita, Manu, Marianna, Sakhila. Thank you girls for the necessary embraces at every stone in the road and the talks as an antidote against frustration.

Ich muss auch Gunnar für seine ausgezeichnete technische Unterstützung und Hilfe bei meinen sehr häufigen Zweifeln danken. Ebenso möchte ich Elena für ihre hervorragende technische Leistung danken, denn ihre technische Unterstützung hat bei vielen der hier enthaltenen Experimente den Unterschied ausgemacht. я хочу поблагодарить тебя за твои человеческие качества, ты всегда находила время выслушать и помочь в самые трудные моменты работы над докторской диссертацией. От всего сердца спасибо тебе за всё!

Eine besondere Erwähnung muss an Raquel und Tobi gehen, da ihr bei der Entwicklung dieser Arbeit eine entscheidende Rolle gespielt habt. Gracias Raquel, por ser mi guía y haberme querido llevar siempre a la excelencia. An Tobi, weil er mir das Privileg gegeben hat, diese Erfahrung zu machen, die mich beruflich und persönlich hat reifen lassen. Danke, dass du mir dein Vertrauen geschenkt hast.

To my family in Chile, for holding my hand through my first steps in science and make me feel that I am one of them. Victor, Natalia, Pancha: I miss you.

To my family in Germany, Amrei, Jelen a and Miriam, for being my home and saving me from the clutches of relentless capitalism.

Above all, to my parents, my brother and my grandmothers. Thank you for being unconditional and for making sense of the distance. Nunca sabré expresar cuánto os quiero y admiro.

A los seres intangibles que habitan la vulnerabilidad y siembran luz hasta hacerla rielar.

A Marta, que me ha traído la paz.

This thesis is dedicated to the otherness and reminds that science also belongs to the minorities.

DECLARATION OF INDEPENDENCE

I, Laura Trigueros López, born on 09.01.1993 in Málaga, hereby declare that I have prepared this thesis without the unauthorized assistance of third parties and without the use of resources other than those indicated.

The data and concepts taken directly or indirectly from other sources are marked with an indication of the source. In particular, I have not made use of the paid assistance of intermediary or advisory services (doctoral advisors or other persons).

The thesis has not been submitted to any other examination authority in the same or a similar form, neither in Germany nor abroad.

Regensburg, 14.07.2022

